Switchable Bragg gratings

Marckmann, Carl Johan; Kristensen, Martin

Publication date:
2003

Document Version
Publisher's PDF, also known as Version of record

Switchable Bragg gratings

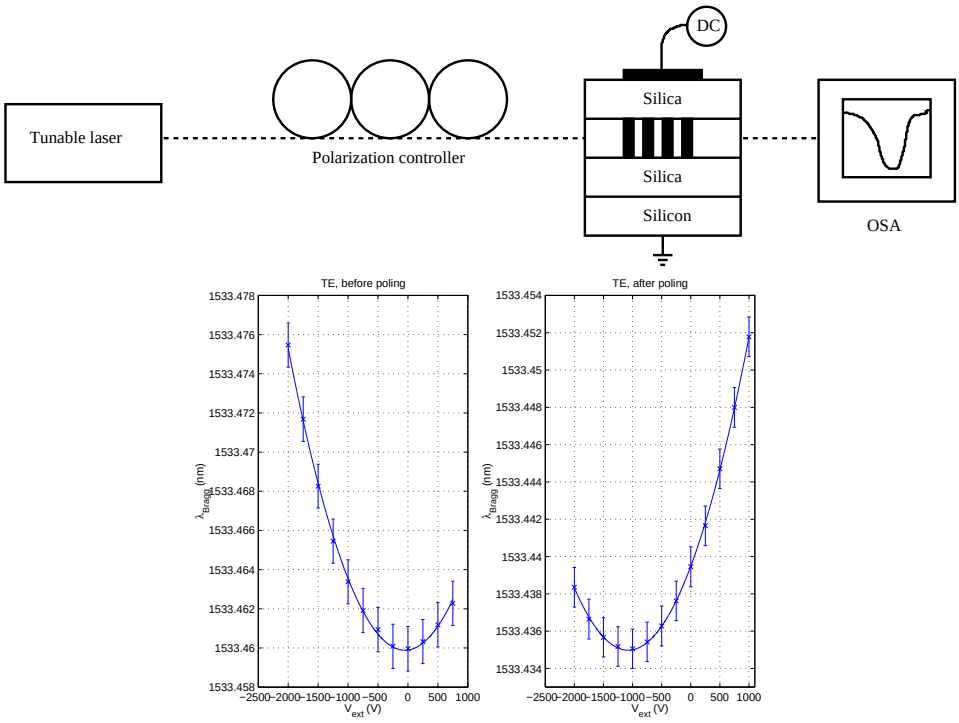

Carl Johan Marckmann
COM
Technical University of Denmark
Ph.D. Thesis, April 2003

Abstract

The subject of this Ph.D. thesis was the development of an electrically switchable Bragg grating made in an optical waveguide using thermal poling to be applied within optical telecommunication systems.
The planar waveguides used in this thesis were fabricated at the Micro- and Nanotechnology Research Center (MIC) at the Technical University of Denmark. The Bragg gratings were fabricated at COM using UV irradiation of the planar waveguides using the phase mask method. The induction of a frozen-in DC electric field into the samples was performed by thermal poling of the Bragg gratings.
Characterization of the third-order nonlinearities and the frozen-in field were performed using a new measurement method where the Bragg gratings were used as probes. Good coherence was obtained between this new measurement method and the traditional Mach-Zehnder interferometer method.
In the project, several important questions regarding the nonlinearities of silica glass were addressed. It was found that the greatest change in the third-order nonlinearity was obtained by doping the waveguides. No UV induced change of the third-order nonlinearity was observed in this project. By increasing the sample buffer layers it became possible to investigate the symmetry properties of the third-order nonlinearities. Contrary to the expectations for an amorphous material, the measurements indicated an almost polarization independent third-order nonlinearity - the most probable explanation being electrostriction. This result is very useful in the production of telecommunication devices since polarization independence of the second-order nonlinearity is wanted.
In order to increase the second-order nonlinearity, it was found that the introduction of a high refractive index trapping layer was favorable. During the thesis, the thermal poling induced second-order nonlinearity was increased by approximately 64% making a silica based optical switch possible.
Finally, a possible explanation to the very high, but short-lived, poling results obtained by some groups was discovered.

Resume

Emnet for denne Ph.D. afhandling var udviklingen af et elektrisk flytbart Bragg gitter, lavet i optiske bølgeledere ved hjælp af termisk poling, til brug inden for optiske telekommunikationssystemer.
De planare bølgeledere, der blev anvendt i denne afhandling, blev fremstillet på Mikro- og Nanoteknologi Forsknings-Centret (MIC) ved Danmarks Tekniske Universitet. Bragg gitrene blev lavet på COM ved UV bestråling af de planare bølgeledere ved hjælp af fasemaskemetoden. Skabelsen af et indefrossent DC elektrisk felt i prøverne foregik ved termisk poling af Bragg gitrene.
Karakteriseringen af tredje-ordens ulinearitetерne og de indefrosne felter blev udført med brug af en ny målemetode, hvor Bragg gitrene blev brugt som prober. God overensstemmelse blev opnået mellem denne nye måle metode og den traditionelle Mach-Zehnder interferometer metode.
I projektet blev flere vigtige spørgsmål vedrørende unlinearitetерne i silica glas adresseret. Det blev fundet, at den største ændring af tredje-ordens ulinearitetен blev opnået ved dotering af bølgelederne. Ingen UV-induceret ændring af tredje-ordens unlinearitetен blev observeret i dette projekt.
Ved en forøgning af prøvebufferlaget blev det muligt at undersøge symmetrieegenskaberne af tredje-ordens ulinearitetерne. I modsætning til forventningerne til et amorft materiale indikerede målingerne en næsten polarisationuafhængig tredje-ordens ulinearitet. Den mest sandsynlige forklaring på dette er elektrostriktion. Dette resultat er meget brugbart indenfor produktionen af telekommunikations udstyr, da polarisations-uafhængighed af anden-ordens ulinearitetен er ønskeligt.
For at øge anden-ordens ulinearitetен blev det opdaget, at introduktionen af et lag med højt brydningsindeks til indfangning af ladninger var favorabelt. I løbet af denne afhandling blev den termisk poling-inducerede anden-ordens ulinearitet forøget med cirka 64%, hvorved en silica-baseret kontakt er mulig. Endelig blev der opdaget en mulig forklaring på de meget høje, men kortlevede, poling-resultater opnået af visse grupper.

Acknowledgements

I would like to thank my supervisors, Martin Kristensen (COM), Thomas Rasmussen (ADC Denmark Aps.), Thomas Clausen (ADC Denmark Aps.) and Kent E. Mattsson (NKT Research A/S) for always having the time to help me with scientific and practical questions during my study. A special thanks to NKT Research A/S for taking over my project at the end of 2001 when ADC Denmark Aps. closed due to the recession in the telecommunication sector.
In the fabrication and test of planar waveguides, I would like to thank Jesper Arentoft, Yitao Ren, Rune Shim, Thomas Clausen, and Morten G. Dyndgaard for their assistance in the cleanroom. Also thanks to Karin N. Andersen and Hayan Ou for their answers to cleanroom and sample fabrication questions and to M. Svalgaard for his help in measurering the structure of the waveguides.
A special thanks to Jesper Bo Damm Jensen, Poul Varming and Hans-Jürgen Deyerl for their extremely valuable help in the excimer laser lab and to Jörg Hübner and Nicolai Plougmann for the very constructive discussions on Bragg gratings.
Thanks to Jesper Bo Damm Jensen, Rune Shim, Yitao Ren, Jacob Fage-Pedersen and Christoffer Marckmann for proofreading the thesis.
A deep and heart-felt thanks to all my dear colleagues that I have had at COM, ADC Denmark Aps. and NKT Research A/S during the project. It has been a pleasure for me to work together with you all and you have made this project very enjoyable and memorable.
Finally, I would like to thank my family, my girl-friend and her family for their patience and support during this study.

Carl Johan Marckmann
COM
Technical University of Denmark
April 2003

Publication list

Below is a list of the publications made during this project:

- C. J. Marckmann, Y. Ren, G. Genty and M. Kristensen, "Strength and symmetry of the third-order nonlinearity during poling of glass waveguides", IEEE Photon. Technol. Lett., **14** (9), pp. 1294-1296, 2002.
- Y. Ren, C. J. Marckmann, J. Arentoft and M. Kristensen, "Thermally poled channel waveguides with polarization-independent electrooptic effect", IEEE Photon. Technol. Lett., **14** (5), pp. 639-641, 2002.
- C. J. Marckmann, J. Arentoft and M. Kristensen, "Measuring poling-induced nonlinearities in Ge:SiON waveguides using a Bragg grating", in OFC 2001, Tech. Dig., pp. WDD94-1-WDD94-3, 2001.
- C. J. Marckmann, G. Genty, Y. Ren, J. Arentoft, and M. Kristensen, "Bragg gratings as probes to dertermine nonlinearities induced by thermal poling", in BGPP 2001, Tech. Dig., pp. BFC3-1-BFC3-3, 2001.
- C. J. Marckmann, R. Shim, Y. Ren, and M. Kristensen, "Interpretation of high poling effects with short lifetimes", in ECIO 2003, Vol. 1, pp. 301-304, 2003.
- Yitao Ren, Carl Johan Marckmann, Rune Shim and Martin Kristensen, "Increased electro-optic effect in poled waveguides with a charge-trapping layer", submitted for BGPP 2003.
- M. Kristensen, J. Arentoft, J. B. Jensen, H.-J. Deyerl, J. Lægsgaard, C. J. Marckmann, N. Plougmann, Y. Ren, S. Søgaard and P. Varming, "Bragg gratings and poling", DOPS-NYT, **2**, pp. 49-54, 2001.

Contents

Chapter 1

Introduction

The ability to communicate complex information is one of the characteristics of human kind. As populations grow and the interaction between people increases, the need for increased speed in information delivery is required. An example of a remedy to facilitate the transmission of information was the invention of the analogue telephone, which allowed a point-to-point information transfer transmitted via electrical signals. Besides the point-to-point nature of the electrical networks, they suffer from small repeater spacing in the case of fast operation speeds and slow operation speeds in the case of large repeater spacing [2]. As an example, one can mention the microwave systems from the 1970s with a maximum speed of 274Mb/s with a repeater spacing of only 1km.
The invention of the optical fiber with a loss of less than $0.2\frac{\text{dB}}{\text{km}}$ at a wavelength of 1.55μm, the invention of single-mode semiconductor lasers in this wavelength window together with the invention of optical amplifiers spawned the development of optical telecommunication. The invention of the Internet resulted in an exploding demand for bandwidth. The Internet traffic almost doubles every year and thus obeys a Moore's law for Internet traffic [1]. Optical telecommunication allowed for a large bandwidth at a relatively low price and was the obvious way of overcoming the ever increasing demand for higher bandwidth.
The invention of Wavelength Division Multiplexing (WDM) increased the bandwidth of the already installed optical fiber many times. Today's commercially available optical telecommunication systems transmit information at speeds up to 0.8Tb/s (80 channels at 10Gb/s) with a repeater separation of 40-50km (medio April 2003). Unfortunately, the optical networks still have a point-to-point nature due to the poor availability/high prices of optical components capable of switching, filtering and modulating the optical

[1] In 1965 Moore predicted a doubling in the number of transistors in a CPU every approximately 18 month. A development the semiconductor industry has followed ever since and probably will for the next two decades.

signals. The existing modulators are based on $LiNbO_3$ or Micro Electro-Mechanical Systems technology which is expensive or slow and difficult to integrate into the glass based fiber optical networks. A large effort is put into developing glass based technology able to provide these devices.

The scientific goal of this project was to make a Bragg grating, in a silica based waveguide, that could be switched in wavelength by the application of a (small) voltage drop across the device. Such a Bragg grating would in itself serve as a switchable filter and find use in devices such as Optical Add Drop Multiplexers and thus would be very useful in telecommunication systems. Silica is an inversion symmetric material and thus it does not posses a second-order nonlinear effect [2] which could have enabled the fabrication of a switchable Bragg grating. Without the second-order nonlinearity, the Kerr effect is responsible for the electric field induced wavelength change in silica and this effect is too small to have any commercial value.
Through thermal poling it is possible to induce a second-order nonlinearity into silica glass [53]. The induced second-order nonlinearity is still not high enough for practical use. Thermal poling is the method used in this project to induce second-order nonlinearities into the samples and a great part of the thesis has been devoted to increasing the effect in the waveguides used. Another part of the project was the development of a measurement setup in which the switchable Bragg grating was used to probe the second- and third-order nonlinearities of the material in which they had been made. Finally, part of the project was devoted to making the waveguides used in the experimental setup and to the variation of several process parameters to investigate material effects on the nonlinearities.

This thesis consists of six chapters. Chapter 1 contains this introduction. Chapter 2 contains the theory used in the thesis. The principle of total internal reflection is described. This is the principle used to guide the light in the planar waveguides. Bragg gratings, and specifically uniform Bragg gratings, are explained together with the Gaussian fitting used to determine the effective refractive index of the optical waveguides. Nonlinear optical media and the expectations to amorphous materials such as silica are described together with two models explaining the symmetry breaking during thermal poling.

[2] In this thesis the nomenclature of [53] and [61] has been adopted i.e. the second-order nonlinear term/effect, $\chi^{(2)}$, represents the second term in the Taylor's series of the polarization density,

$$P(E) = \epsilon_0 \left(\chi E + \chi^{(2)} E^2 + \chi^{(3)} E^3 + \cdots \right) ,$$

and the third-order nonlinear term/effect, $\chi^{(3)}$, represents the third term in this series.

In Chapter 3, the fabrication of the samples is described. It consists of a description of the processing equipment used to make the samples in the cleanroom at the Technical University of Denmark together with a description of the process parameters used and some of the discoveries made regarding annealing procedures during the sample processing. A description of the Bragg grating fabrication performed at COM is also included in this chapter.
The experimental setup is covered in Chapter 4. Here, the thermal poling process is explained together with the experimental setup as well as how the nonlinearities are extracted from the measurements. Finally, the experimental setup developed during this project is compared to existing methods and the pros and cons of the different methods are discussed.
In Chapter 5, the results obtained during this project are analyzed. Five different types of samples are characterized in this chapter: UV written samples with a thin buffer layer, UV written samples with a thick buffer layer, UV written samples with a trapping layer, etched samples with soft top-cladding and etched samples with hard top-cladding.
The thesis ends with a conclusion in Chapter 6 in which the concluding remarks are presented together with an outlook on the future possibilities for thermal poling as well as suggestions as how to increase the second-order nonlinearity in planar waveguides.
Two appendices have been added in Chapters A and B. In Chapter A, the sample thicknesses and refractive indices of the different sample layers are described and in Chapter B, the measurements are presented in tabular form.

Chapter 2

Theory

2.1 Introduction

This chapter describes the theory needed to understand the measurements presented in this thesis. In section 2.2 the principle of total internal reflection, used to guide the light in the waveguides, is briefly described. Section 2.3 describes the theory behind Bragg gratings used in this thesis to determine the nonlinearities in the waveguides. In section 2.4, the basic properties of a nonlinear material are given. A method to induce a second-order nonlinear effect in silica glass, called poling, is described in section 2.5.

2.2 Waveguides

When the nonlinear properties of a material are investigated, it is important to consider how the assignment is performed in the best way. Either bulk material or waveguides in the material can be investigated. Guided waves present several advantages over plane waves in bulk material, since nonlinear optics require high light intensities (for Second Harmonic Generation, SHG). The high intensities are automatically obtained in waveguides, but in a bulk material it requires the focusing of a laser beam. The focusing of the laser reduces the length over which the light interacts with the nonlinear region. The interaction length in a waveguide is determined by the length of the waveguide. Using waveguides, the possibility to dope and test the dopants' influence on the nonlinearities is also more easily determined. Finally, waveguides have the advantage that they are easily incorporated into setups using guided waves and fiber optics.
In this section, the principle behind wave-guiding is described shortly. In the samples presented in this thesis, the wave-guiding is performed by the principle of total internal reflection (used in e.g. fibers, planar, etched and UV-written waveguides). For a slab waveguide, as seen in Figure 2.1, it is found that light from the high refractive index dielectric (n1 and an-

gle $\Theta 1$) will be totally reflected at the interface with the low refractive index dielectric (n2) as long as $\Theta 1 > \sin^{-1}\left(\frac{n2}{n1}\right)$, found using Snell's law, $n_1 \sin\Theta_1 = n_2 \sin\Theta_2$. Solving the wave equation for a tri-layered structure with refractive indices $n1 > n2 \geq n3$ with the the light traveling in the x-direction and confined to the core layer (n1) yields a standing wave in the core layer ($E_y \propto \cos y$) and exponentially decaying waves in the cladding layers ($n2$ and $n3$), $E_y \propto \exp(-|y|)$.
For a planar waveguide, the structure is illustrated in Figure 2.2. Assuming that each individual layer (layers n1, n2, n3, n4 and n5) is uniform and that $n1 > ni, i = \{2, 3, 4, 5\}$, the solution to the individual layers for a wave traveling in the z-direction, will be given as $E(x, y) = E_1(x)E_2(y)$. $E_1(x)$ and $E_2(y)$ are the solutions to the different tri-layer structures constituting Figure 2.2 i.e. $n1 > n4 \geq n2$ or $n1 > n3 \geq n5$, respectively. The solutions found must be continuous at the interfaces. Thus, in layer n1 $E(x, y) \propto \cos x \cos y$, in layers n2 and n4 $E(x, y) \propto \cos y \exp(-|x|)$ and in layers n3 and n5 $E(x, y) \propto \cos x \exp(-|y|)$.

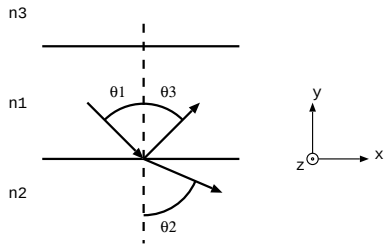

Figure 2.1: A schematic of Snell's law. Light from high index dielectric, n1, is falling onto the interface between the two dielectric materials at an angle $\Theta 1$. $\Theta 2$ represents the transmitted wave and $\Theta 3$ the reflected.

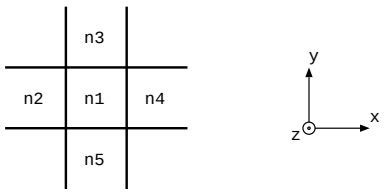

Figure 2.2: A schematic of a planar waveguide. n1 is the refractive index of the core and $n1 > ni, i = \{2, 3, 4, 5\}$. Light is transmitted in the z-direction.

2.2.1 Waveguide loss

The loss in silica waveguides is caused by absorption and scattering in the core layer and leakage of light from the core layer. The absorption of light is due to vibrational transitions and electronic transitions in the silica glass. The scattering, Rayleigh scattering, is due to randomly distributed variations of the molecular positions in the glass creating refractive index inhomogenieties that acts as scattering centers. The silicon wafer introduces a leakage loss due to its higher refractive index relative to the silica core.
Using the program CrystalWave [12], an estimation of the loss induced by the silicon wafer has been calculated for a UV-written sample with a thin buffer layer made on a silicon wafer as described in section A.1 and analyzed in section 5.2. The program uses a real-valued refractive index distribution and

the calculated loss is therefore entirely due to leakage loss. The calculation method used by the program is Finite-Difference Time-Domain with perfectly matched layers in three dimensions. Convergence has been obtained for all the relevant calculation parameters. According to the calculations, the TM polarization is suppressed by approximately 35dB compared to the TE mode. This result is in accordance with the experimental findings of section 5.2, where the difference between TE and TM polarization transmission for a sample with a thin buffer layer is found to be above 30dB.

2.3 Bragg gratings

A periodic modulation of the effective refractive index in a waveguide is called a Bragg grating and yields a frequency-dependent reflectivity of the light traveling in the waveguide.
Bragg gratings are very versatile and in the telecommunication sector, Bragg gratings are used as wavelength selective devices in Wavelength Division Multiplexing networks [26]. Bragg gratings are also used as sensors measuring temperature, stress, etc. [70, 30]. In this thesis, UV written uniform Bragg gratings made using the phase mask method [25] are used to determine nonlinear properties in waveguides as described below.

2.3.1 Uniform Bragg grating

In Figure 2.3 the refractive index modulation profile of a Bragg grating is illustrated. The refractive index modulation is given by

$$n(z) = n_{core} + n_{ave}(z) + n_{mod}(z) \sin\left(\frac{2\pi}{\Lambda_{grating}} z + \phi(z)\right) , \qquad (2.1)$$

where n_{core} is the waveguide refractive index prior to UV exposure, $n_{ave}(z)$ is the average UV induced refractive index change, $n_{mod}(z)$ is the refractive index modulation amplitude, $\Lambda_{grating}$ is the period of the modulation in the waveguide and $\phi(z)$ is a phase describing possible chirp in the phase mask. The Bragg condition is satisfied when

$$n_{eff}\Lambda_{grating} = \frac{m\lambda_{Bragg}}{2} , \qquad (2.2)$$

where n_{eff} is the effective refractive index of the waveguide, m represents the m'th order Bragg diffraction and λ_{Bragg} is the wavelength of the light reflected by the periodic perturbation [2, p. 105]. When equation 2.2 is satisfied, the waves propagating in the forward and backward directions are coupled to each other. The coupled-mode equations are

$$\frac{dA_f}{dz} = i\delta A_f + i\kappa A_b \qquad (2.3)$$

$$\frac{dA_b}{dz} = -i\delta A_b - i\kappa A_f , \qquad (2.4)$$

where A_f and A_b are the forward and backward propagating waves, respectively. δ is the detuning from λ_{Bragg}, $\delta = \frac{2\pi}{\lambda} - \frac{2\pi}{\lambda_{Bragg}}$, where λ is the wavelength of the light in the waveguide. κ is a constant describing the coupling between the two waves, A_f and A_b. The linear nature of equations 2.3 and 2.4 means that they can be solved analytically. The transmitivity of the grating is given by [27]

$$T(\lambda, L) = 1 - \frac{\kappa^2 \sinh^2\left(\sqrt{\kappa^2 - \delta^2}L\right)}{\delta^2 \sinh^2\left(\sqrt{\kappa^2 - \delta^2}L\right) + (\kappa^2 - \delta^2)\cosh^2\left(\sqrt{\kappa^2 - \delta^2}L\right)}\ , \quad (2.5)$$

where L is the length of the grating. In the wavelength range around λ_{Bragg} this expression is fitted well by a Gaussian function

$$F(x) = a + bx + c \cdot \exp\left(\frac{(x-d)^2}{e}\right)\ . \quad (2.6)$$

a is the background, b is the slope of the background, c is the height of the Gaussian, d is its center and e the width. By fitting the transmission spectrum given by equation 2.5 by the Gaussian function in equation 2.6, the center of the transmission spectrum is easily found. In Figure 2.4, equation 2.6 is fitted to equation 2.5.

The choice of using uniform Bragg gratings to measure the effect of poling of waveguides was two-fold. Firstly, uniform gratings are the only type of grating for which it is possible to find analytical solutions [27]. Secondly, they are very simple to make compared to many of the grating types used within telecommunication (sinc grating, Gaussian gratings). An example of a transmission spectrum of a uniform Bragg grating made in a waveguide is shown in Figure 4.3.

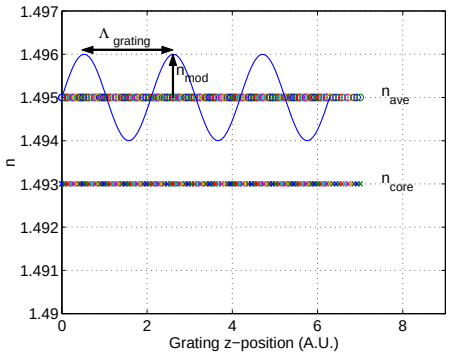

Figure 2.3: The periodic refractive index modulation constituting a Bragg grating in a waveguide.

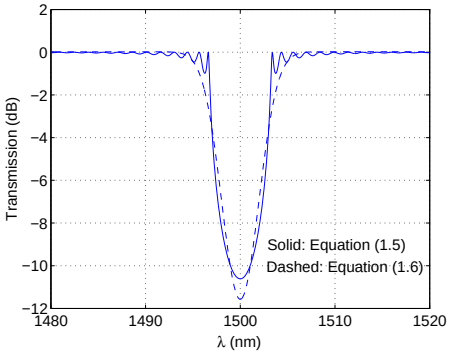

Figure 2.4: The transmission spectrum of a uniform grating plotted versus wavelength (solid curve) and a Gaussian fit (dashed curve).

2.4 Nonlinear optics

Nonlinear optics characterize a dielectric medium in a large electric field, E, i.e. when E takes on the size of the inter-atomic electric fields $\left(10^5 - 10^8 \frac{V}{m}\right)$. In a large E field, the polarization density P can be written as a power series

$$P(E) = \epsilon_0 \left(\chi E + \chi^{(2)} E^2 + \chi^{(3)} E^3 + \cdots\right) , \tag{2.7}$$

where ϵ_0 is the vacuum permittivity, χ is the electric susceptibility, $\chi^{(2)}$ is the second-order nonlinearity and $\chi^{(3)}$ is the third-order nonlinearity. Normally, terms higher than third order in E can be neglected. Equation 2.7 is derived by neglecting anisotropy ($\Rightarrow P = (P_x, P_y, P_z)$), dispersion $\left(\Rightarrow \chi^{(i)} = \chi^{(i)}(\omega)\right)$ and inhomogeneity $\left(\Rightarrow \chi^{(i)} = \chi^{(i)}(\vec{r})\right)$.
The propagation of light in a nonlinear medium is described by the wave equation with a source term included. Writing equation 2.7 as a sum of the linear and nonlinear terms, $P(E) = \epsilon_0 \chi E + P_{NL}$, where $P_{NL}(E)$ represents the nonlinear terms, and inserting into the wave equation yields

$$\nabla^2 E - \frac{1}{c^2} \frac{\partial^2 E}{\partial t^2} = \mu_0 \frac{\partial^2 P_{NL}}{\partial t^2} = -S , \tag{2.8}$$

where c is the speed of light in the nonlinear medium, μ_0 is the magnetic permeability and S represents a source radiating in the linear medium with refractive index n. Equation 2.8 is the basic equation in nonlinear optics and it can be solved using either coupled-wave theory or the Born approximation. See reference [61, Chap. 19] for a further description on solving equation 2.8.
The various nonlinear terms in equation 2.7 yields various interesting effects. For example, a material possessing a nonzero $\chi^{(2)}$ will have a linear electro-optic effect, where an externally electric field applied across the material can change the refractive index of the material [19, 59] i.e. change the wavelength of an optical signal passing through it. A nonzero $\chi^{(2)}$ also gives 3-wave mixing and optical rectification [61, Chap. 19], together with second harmonic generation (SHG) [62, 77], a special case of 3-wave-mixing. Since the nonlinearities are frequency dependent, it is essential to indicate this. In SHG, an optical field, $E(\omega)$, interacts with itself to yield a second field with twice the frequency, $E(2\omega)$, and thus the second-order nonlinearity is written as $\chi^{(2)}(2\omega; \omega, \omega)$. In the linear electro-optic effect, a DC field, $E(0)$, modifies an optical field, $E(\omega)$, and therefore the second-order nonlinearity is written as $\chi^{(2)}(\omega; \omega, 0)$.
Silica glass is an amorphous and, therefore, macroscopic inversion symmetric material. To obey the inversion symmetry, equation 2.7 has to obey $P(E) = -P(-E)$. Inserting into equation 2.7 yields $\chi^{(2)} = 0$ [1], which is

[1] Actually, all even-order nonlinear terms are zero.

characteristic for a Kerr medium. The lack of a second-order nonlinear effect in silica has prevented the invention of nonlinear silica glass components such as electro-optic switches, modulators, tunable filters and wavelength converters.
Since silica is a Kerr medium, the dominant nonlinear term in equation 2.8 is

$$P_{NL} = \epsilon_0 \chi^{(3)} E^3 \ . \tag{2.9}$$

This term yields third harmonic generation, electro-optic Kerr effect and 4-wave mixing. In this thesis, the electro-optic Kerr effect is the interesting effect and will be dealt with in the following [2]. Let us assume that the electric field, $E(t) = E(0) + Re\{E(\omega)\exp(i\omega t)\}$, in the Kerr medium is a sum of a harmonic component, $E(\omega)$, and a DC electric field $E(0)$ and that $|E(\omega)|^2 \ll |E(0)|^2$. Inserting this into equation 2.9 yields

$$P_{NL}(t) = P_{NL}(0) + Re\left\{P_{NL}(\omega)e^{i\omega t}\right\} \ , \text{where} \tag{2.10}$$

$$P_{NL}(\omega) = 3\epsilon_0 \chi^{(3)} E(0)^2 E(\omega) = \epsilon_0 \Delta\chi E(\omega) \ , \tag{2.11}$$

where $\Delta\chi$ is the change in susceptibility due to $E(0)$. Equation 2.10 corresponds to a linearization of equation 2.9 with respect to $E(t)$ as seen in Figure 2.5. Using $n^2 = 1 + \chi$ together with equation 2.11 yields

$$\Delta n = \frac{3\chi^{(3)} E(0)^2}{2n} \ . \tag{2.12}$$

Equation 2.12 shows that the Kerr medium has an effective refractive index $n + \Delta n$, quadratically determined by $E(0)$.

2.5 Poling

In 1981, Sasaki *et al.* [62] reported that SHG was observed for the first time in $Ge : SiO_2$ fiber, which is in contradiction to the inversion symmetric nature of silica and thus to the zero second-order nonlinearity. Myers *et al.* [53] discovered a way to incorporate a second-order nonlinearity in silica by electric field poling of glass in 1991. The thermal poling is performed by heating the sample while applying a large static electric field across the sample. In 1995 Fujiwara *et al.* [19] discovered UV poling, where a second-order nonlinearity is induced in silica by applying a large static electric field across the sample while it is excited by UV irradiation. The induced second-order nonlinearities obtained by these methods are either too small, unstable or difficult to reproduce and thus not yet suitable to be used in components. A significant effort is therefore put into achieving a large reproducible second-order nonlinear effect in silica. An understanding of the poling is key to achieving this

[2] For the electro-optic Kerr effect $\chi^{(3)} = \chi^{(3)}(-\omega; \omega, 0, 0)$.

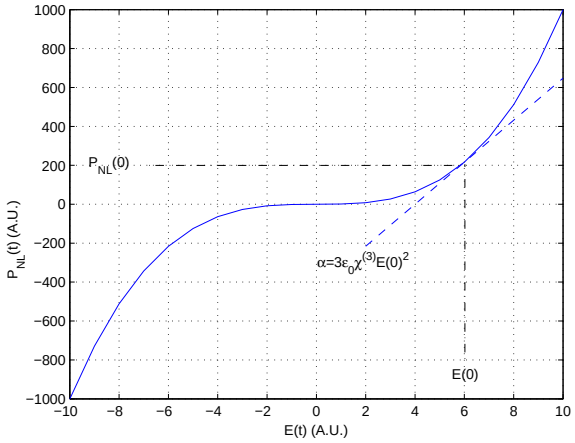

Figure 2.5: A plot of the linearization of $P_{NL}(t)$ with respect to $E(t)$. The solid line represents equation 2.9 and the dashed line is the linearization, equation 2.10. α represents the slope of the linearization.

goal. Two different models exist describing the effect induced by poling [32]: The dipole model, see subsection 2.5.2 and the charge separation model, see subsection 2.5.1. It is important to understand that these two models are not mutually exclusive and during poling, both a dipole orientation and a charge separation can take place. According to Keilich [33] the second-order nonlinearities in a transparent isotropic medium are related by

$$\gamma = \frac{\chi^{(2)}_{TM}}{\chi^{(2)}_{TE}} = 3 \ , \tag{2.13}$$

in the case where the second-order nonlinearities are made by charge separation. If the dipole model is the valid model, two limits exist [32]. In the low external field limit, $E_{ext} < \frac{10kT}{\mu} = 5.4 \cdot 10^7 \frac{V}{cm}$, where T is the poling temperature ($T = 630$K), k is Boltzmann's constant and μ is the dipole moment for an electron and a proton separated by 1Å, the ratio between the second-order nonlinearities for the two polarizations is given by equation 2.13. In the high field limit, $E_{ext} \geq \frac{10kT}{\mu}$, the γ ratio depends on the hyperpolarizability components. A γ value close to three will indicate the validity of the space charge model but not exclude the dipole model. A value far from three will support the dipole model. It is, however, very important to emphasize that the result obtained in equation 2.13 is calculated for SHG thus for $\chi^{(2)} = \chi^{(2)}(2\omega;\omega,\omega)$ which is not affected by electric field induced stress (electrostriction) in the sample. Electrostriction is discussed in subsection 2.5.3. Dispersion in $\chi^{(3)}$ can also change the value of γ. Unfortunately, the wavelength dependency of $\chi^{(3)}$ has not been extensively investigated.

2.5.1 The charge separation model

The charge separation model, illustrated in Figure 2.6, assumes that mobile charges (e^-, Na^+, etc.) in the glass move towards the electrodes during poling [32, 53] when a high external voltage and heating is applied. These charges may predominantly be trapped at the interfaces between the core and cladding layers after poling due to the Maxwell-Wagner effect [74, p. 94] and [73, p. 138] where space charges accumulate on the interfaces between materials with different conductivities. This charge trapping gives rise to a sheet of charge with different polarity on both sides of the core layer, yielding an internal frozen-in DC electric field, E_{int}. When an external electric field is applied across the sample after poling, the total DC electric field is $E(0) = E_{int} + E_{ext}$. Inserting this expression into equation 2.12 yields

$$\Delta n(E_{ext}) = \frac{3\chi^{(3)}E_{int}^2}{2n} + \frac{\chi_{eff}^{(2)}}{n}E_{ext} + \frac{3\chi^{(3)}}{2n}E_{ext}^2 \ , \tag{2.14}$$

$$\text{where } \chi_{eff}^{(2)} \equiv 3\chi^{(3)}E_{int}. \tag{2.15}$$

Equation 2.15 is the poling induced second-order nonlinearity.

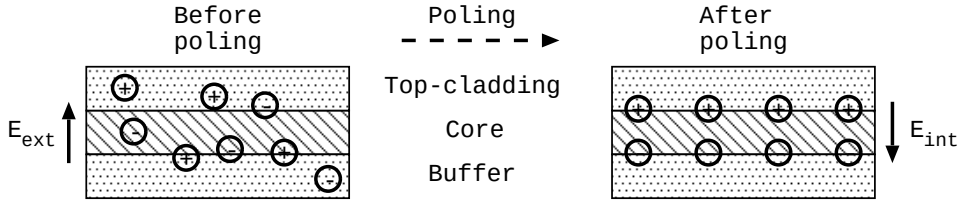

Figure 2.6: An illustration of the charge separation model before (left) and after poling (right).

2.5.2 The dipole model

In the dipole model, see Figure 2.7, it is assumed that dipoles in the material are oriented according to the externally applied electric field during poling [53]. Under the subsequent cooling, the dipole orientation according to the field is retained, yielding a polar axis in the sample. The material is no longer disordered and a second-order nonlinear effect is thus not prohibited by symmetry. The ordering of dipoles will yield a refractive index change as the one described in equation 2.14.

2.5.3 Electrostriction

In this section, the effect of electrostriction on the second- and third-order nonlinearities is described. Equation 2.13 is a consequence of the Kleinmann

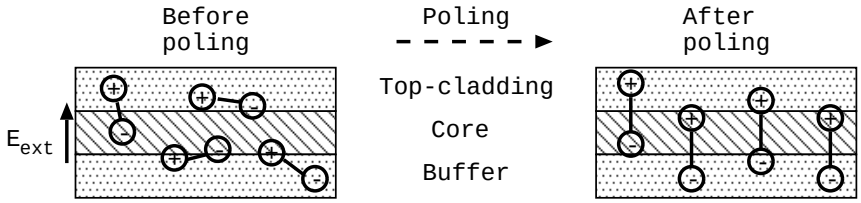

Figure 2.7: An illustration of the dipole model before (left) and after poling (right).

symmetry: When the polarization density is calculated for a Kerr medium subjected to a DC field, $E_y(0)$, along the y-axis of Figure 2.8 and an optical transverse field, $E_x(\omega) + E_y(\omega)$, one obtains

$$P_{NL}^{TE}(\omega) = \epsilon_0 \chi^{(3)} E_y(0)^2 E_x(\omega) \quad (2.16)$$

$$P_{NL}^{TM}(\omega) = 3\epsilon_0 \chi^{(3)} E_y(0)^2 E_x(\omega) \ , \quad (2.17)$$

when the terms resonant with the optical field and the square of the DC field are sought out. Thus, $P_{NL}^{TM}(\omega) = 3 \cdot P_{NL}^{TE}(\omega)$ for the two polarizations yielding equation 2.13.

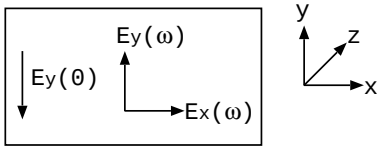

Figure 2.8: An illustration of a Kerr medium subjected to a DC field and a transverse optical field.

The Kleinmann symmetry condition is equivalent to stating that the third-order nonlinearity is dispersion-less [20]. As will become clear later in chapter 5, the Kleinmann symmetry is not obeyed by the samples treated in this thesis. The most likely source of dispersion is electric field induced stress, known as electrostriction.
The contribution from electrostriction to the refractive index is treated in [20]: Assuming that the material only contracts or expands in the axis parallel to the externally applied field [20] finds the electric field induced stress, $\sigma_{||}$, and from this the strain, $\epsilon_{||} = \frac{\sigma_{||}}{Y}$, where Y is Young's modulus. The refractive index variation due to electrostriction is found using the strain-optic relation and finally, the electrostrictive contribution to the third-order nonlinearities is found to be

$$\chi_{TM}^{(3)ES} = \frac{-n^4 p_{11} \sigma_{||}}{3E^2 Y} \quad (2.18)$$

$$\chi_{TE}^{(3)ES} = \frac{-n^4 p_{12}\sigma_{\|}}{3E^2 Y} , \tag{2.19}$$

where p_{11} and p_{12} are the diagonal and off-diagonal elements of the strain-optic tensor.
Defining

$$\alpha \equiv \frac{\chi_{TM}^{(3)}}{\chi_{TE}^{(3)}} , \tag{2.20}$$

[20] finds $\alpha = 1.24$ when electric field induced stress is included and if the Onsager law is used to calculate the electrostrictive constant yielding $\gamma^{ES} = 3.04$. $\alpha = 1.07$ if the Lorentz-Lorenz law is used to calculate the electrostrictive constant, $\gamma^{ES} = 5.36$. Other groups have found values for γ^{ES} ranging from 0.97 to 4.25 [41, 66, 54, 34] allowing for a very large window of α-values.
Thus, the γ-value defined in equation 2.13 cannot be utilized in determining whether the dipole model or the charge-separation model is the valid model describing the poling induced symmetry breaking when electric field induced stress is present in the system.
According to [58, p. 79] an ordering of dipoles gives a change in $\chi^{(3)}$ and thus the behavior of the third-order nonlinearity during poling indicates which of the models is the valid one.

Chapter 3

Fabrication and preparation of waveguides

3.1 Introduction

This chapter describes the cleanroom fabrication of the waveguides and the subsequent UV preparation used to fabricate all the samples used in this thesis. The lower cladding layer (buffer layer) was made by thermal oxidation of silicon as described in subsection 3.2.1. The top-cladding layer was deposited using Plasma Enhanced Chemical Vapor Deposition (PECVD) as described in subsection 3.2.2 and consists of un-doped silica in the case of UV-written waveguides and of boron and phosphorus doped silica in the case of etched waveguides. The core is germanium doped silicon-oxy-nitride (Ge:SiON) deposited using PECVD. The nitrogen gives the core a higher refractive index than the cladding layers, thereby making miniaturization more feasible. In Figure 3.1, the refractive index, n, of the core layer is plotted versus the nitrogen flow rate. Another reason for doping the core with nitrogen is an improved stability of the poling induced effects. In the semiconductor industry, it is customary to make non-volatile memory components using Metal-Nitride-Oxide-Silicon (MNOS) transistors [16, 17]. The nitride layer is included into the transistor due to its high trapping density. When passing an electron current from the gate (metal) to the n-silicon substrate, some of the electrons will be trapped in the nitride-oxide interface. In our samples, the nitrogen doping will result in two charge sheets with different polarity, one at each of the interfaces between the core layer and the cladding layers.
The germanium doping makes the core sensitive to UV light [24] which allows us to define the waveguides and Bragg gratings by UV exposure as described in section 3.2.7.
This chapter is divided into three sections. The first section, section 3.2, describes the processing equipment used to make the samples. It is followed

by section 3.3 describing the UV written waveguides. Section 3.4 describes the etched waveguides.

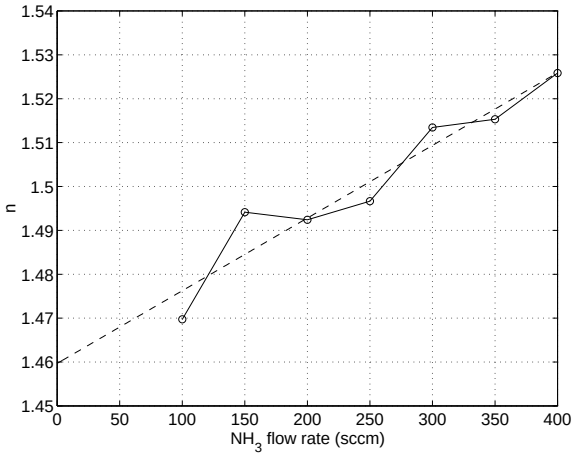

Figure 3.1: The refractive index of Ge:SiON layers for different flow rates of NH_3 after annealing at 800°C in a nitrogen atmosphere for two hours. The flow rate of Ge is kept constant at 3sccm for all the thin films in the figure. The open circles represent the measurements and the dashed line represent a linear fit (extended to a flow rate of 0sccm nitrogen). n is measured with a prism coupler at $\lambda = 632.8\,\text{nm}$.

3.2 Processing equipment

This section describes the work performed in the cleanroom at the Technical University of Denmark. All the samples were processed in the cleanroom environment until the UV treatment, which was the last step before the thermal poling.

3.2.1 Thermal oxidation

Thermal oxide (TOX) was used as a buffer layer in all samples due to its high purity and therefore high dielectric breakdown voltage. The oxidation of the Sb doped Si wafer was performed in a wet (H_2O) atmosphere at 1150°C for a minimum of 32 hours. Since the oxidation of the Si wafer happens at an equal rate at both sides of the wafer, the curvature of the oxidized films is canceled out [1]. The refractive index of thermal oxide is $n = 1.458$ measured at $\lambda = 632.8\,\text{nm}$. The typical thickness obtained was $\gtrsim 4\mu\text{m}$. The disadvantage using TOX is the long process time as illustrated in Figure 3.2. This is somewhat outbalanced by the parallel processing

[1] Compressive stress is still present in TOX films.

method used in the oxidation of the wafers and the fact that it does not require more manpower than the PECVD method.

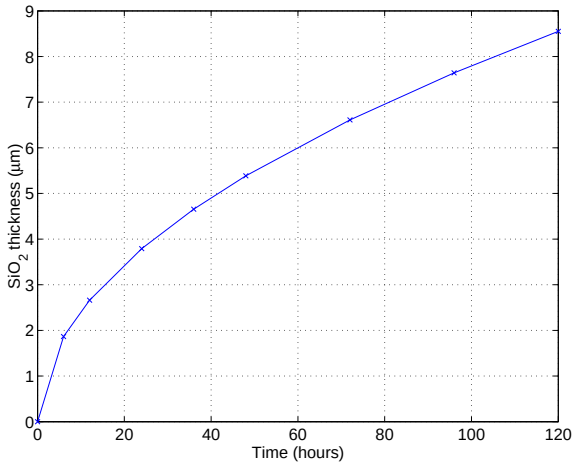

Figure 3.2: The calculated thickness of an oxide film made at 1150°C in a wet atmosphere on the [100] direction of a silicon wafer. The thickness was calculated using [37].

3.2.2 PECVD

Using a plasma, it is possible to reduce the required substrate temperature compared to standard CVD processes by supplying the necessary energy from an electrically-excited gas plasma rather than as heat. The lower substrate temperature reduces the strain in the deposited films. A PECVD chamber is sketched in Figure 3.3. The process gases are let into the reaction chamber through inlet holes in the top electrode. A high power RF signal is applied to the top electrode, while the bottom electrode is grounded (as the rest of the chamber). Residual gases from the plasma are pumped out. The chamber is made of aluminum and therefore it is not possible to use chlorine based process gases because the chlorine would react with the aluminum. Thus hydrogen based gases are used e.g. silane and germane (SiH_4 and GeH_4). By controlling the flow rates of the process gases, the temperature of the substrate and the RF power, the properties of the deposited films are varied. Pure silica, used to make the top-cladding layers in the UV written samples, is made by a gas mixture of silane and nitrosoxide:

$$SiH_4(g) + 2N_2O(g) \rightarrow SiO_2(s) + 2N_2(g) + 2H_2(g) \ .$$

The germanium and nitrogen doped core layers were made by mixing ammonia, silane, germane and nitrosoxide. The germanium replaces silicon in the glass matrix and nitrogen replaces oxygen [49]:

$$GeH_4(g) + 2N_2O(g) \rightarrow GeO_2(s) \quad + \quad 2N_2(g) + 2H_2(g) \ ,$$

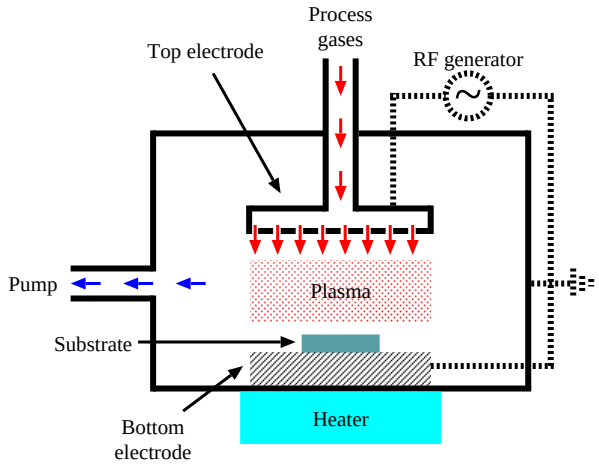

Figure 3.3: A schematic representation of a PECVD chamber.

$$\begin{aligned} XSiH_4(g) + (2X + Y + \frac{3}{2}Z)N_2O(g) \quad &+ \quad ZNH_3(g) \rightarrow \\ Si_XO_YN_Z(s) + (2X + \frac{3}{2}Z)H_2O(g) \quad &+ \quad (2X + Y + \frac{3}{2}Z)N_2(g) \end{aligned}$$

In the case of etched waveguides, the top-cladding was made of silica doped with boron and phosphor, called soft top-cladding or soft glass. Soft top-cladding floats when wet annealed at 1000°C. This gives a nice even surface without voids between the closely spaced cores. Phosphor and boron replaces Si in the glass matrix and the reactions are

$$\begin{aligned} 2PH_3(g) + 5N_2O(g) \quad &\rightarrow \quad P_2O_5(s) + 5N_2(g) + 3H_2(g) \ , \\ B_2H_6(g) + 3N_2O(g) \quad &\rightarrow \quad B_2O_3(s) + 3N_2(g) + 3H_2(g) \ . \end{aligned}$$

There are two reasons to dope the soft top-cladding with these two materials. Firstly, there is the well-known phenomenon of depression of melting point. By adding a new substance to silica, the melting point of the mixture is lowered compared to that of pure silica [63, Sect. 2.3] thus allowing BP-doped top-cladding to flow at the obtainable temperatures in the anneal ovens. Secondly, boron decreases and phosphor increases the refractive index of the silica glass in which it is incorporated, thus enabling an index matching of the top-cladding and buffer layers [80].
The process parameters used for glass deposition in this thesis were: Process temperature= 300°C, process pressure=400mTorr/500mTorr, RF frequency=380kHz and RF power=380W/800W. The low RF power (380W) was used for the core layer and pure silica layer depositions and the high RF power (800W) was used for the soft top-cladding depositions. The flow rate of the gases depended on the type of glass deposited. The same flow rates were used for the same types of glass on the different samples.

3.2.3 Annealing

The annealing of the PECVD grown thin films is performed in order to densify the glass [49] and thus obtain a cross-linkage of the glass network and in order to out-diffuse hydrogen bound in the glass layers during deposition.

Core annealing

The UV-written samples presented in section 3.3 all had their core annealed at 800°C for two or four hours. The temperature was chosen in order to reduce fabrication problems. During the sample fabrication in the cleanroom, it was observed that annealing at temperatures higher than 800°C yielded a large reduction in the number of successfully processed samples. Layers deposited with high incorporation of NH_3 were almost always destroyed during subsequent annealing at high temperatures. A disadvantage using this low anneal temperature is that only a small cross-linkage of the core layer is obtained [49] yielding a lower densification of the core layer and thereby a lower refractive index increase during annealing.
For the etched samples presented in section 3.4, different types of anneal were performed. Batch one had their cores annealed at 800°C for the reasons mentioned above and in order to be able to compare the results directly to the UV-written waveguides.
The second batch had their cores annealed either at 1000°C in a nitrogen atmosphere or at 1100°C in a wet (H_2O) atmosphere. The higher temperature $\geq$ 1000°C was chosen to be able to float the soft cladding without having hydrogen out-diffusing in an uncontrolled manner from the core layer. The wet anneal at 1100°C was also an attempt to check the properties of the core glass when maximum cross-linking was applied to the layer.
As can be seen in Figure 3.4, the refractive index of samples annealed in a wet atmosphere is almost constant, while those annealed in a dry atmosphere have an increasing refractive index as a function of the ammonia flow rate. This can be explained by evaporation of nitrogen from the core in the wet anneal if the H_2O acts as a catalyst creating (probably) N_2 from the core by oxidation of Si_3N_4. In the dry anneal, a similar process will not happen due to the inertness of the N_2 atmosphere. Two interesting points are noticed in the dry anneal of Figure 3.4. Firstly, the 0sccm NH_3 measurement yields a refractive index of the $Ge : SiO_2$ below the value of pure silica ($n = 1.458$ measured at 632.8nm). Since germanium doping increases the refractive index of silica [31, Chap. 1], this result is unexpected. The measurement can be explained by 1000°C not being a high enough temperature for annealing of pure $Ge : SiO_2$ and thus the annealing induced densification of the glass is not complete. Secondly, the 400sccm NH_3 measurement is lower than expected from the linear fit, indicating that above the 325sccm NH_3 flow-rate, the glass becomes saturated with nitrogen.

Dictated by our experience with the annealing of batch two, the samples in batch number 3 were annealed for 12 hours at 800°C in a nitrogen atmosphere followed by four hours at 1000°C in a nitrogen atmosphere. This special anneal procedure was invented in an attempt to remedy the problem mentioned above with the low yield at high anneal temperatures of the core layer. The problems could be explained by H_2 out-diffusing too fast from the core. A long anneal at low temperature could make the lightly bound hydrogen out-diffuse slowly and the high temperature would remove the rest of the hydrogen. The choice of dry anneal of the etched batch number 3 was also made since it ensured a varying nitrogen content as opposed to the wet anneal.

Top-cladding annealing

The top-cladding of the UV-written samples, section A.2, was annealed at 800°C because a higher temperature would make hydrogen flow out of the core (annealed at 800°C) and into the top-cladding (and parts of the core). This would give small hydrogen bubbles in the core and top-cladding layers yielding a large loss in the power transmitted through the waveguides.
Top-cladding for the etched samples in batch one, section 3.4.1, were annealed at 800°C for the same reason as above. Another reason was that the hard top-cladding cannot flow and thus a low temperature anneal was sufficient. The reason for annealing the samples with soft top-cladding at 800°C was also to be able to compare the results to the UV-written samples. Batch two, section 3.4.2, and three, section 3.4.3, all had their top-cladding annealed wet at 1000°C to flow the top-cladding.

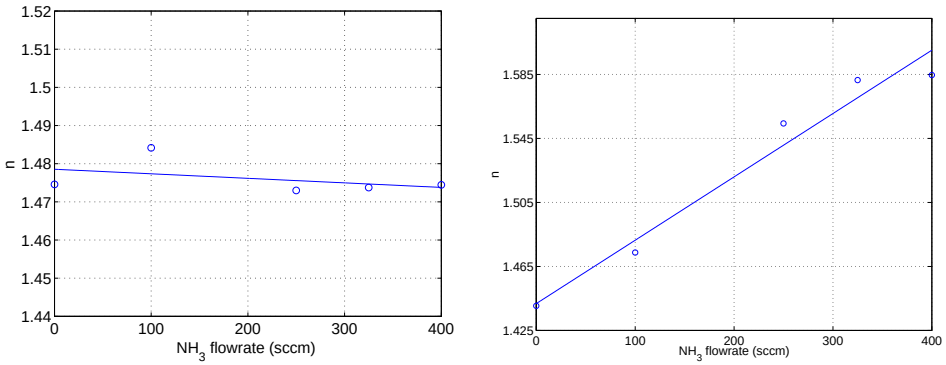

Figure 3.4: The refractive index of Ge:SiON films for different flow rates of NH_3 after annealing wet at 1100°C (left) and dry at 1000°C (right). The flow rate of Ge is 2sccm for all films in both figures. n is measured at $\lambda = 632.8$ nm.

3.2.4 UV lithography

UV lithography is used to define the areas where waveguides are wanted. For the UV written waveguides, this step was performed after annealing of the top-cladding. In the case of etched waveguides, this step was performed after annealing of the core. In both cases, the following process was used for a positive process (called positive process because the resulting photo-resist pattern represents a direct copy of the mask pattern) as seen in Figure 3.5:

1. Photo-resist was spun onto the sample surface (2.2μm) and baked.
2. The photo-resist was exposed to UV light through a chromium mask containing the desired pattern. The solubility of the exposed areas is increased through a chemical reaction.
3. The photo-resist was developed in a basic (NaOH) solution.

In a negative process, where the resulting photo-resist pattern is the inverted of the mask pattern, two extra steps were included in the lithography. After step two, the sample would be heated for two minutes at 120°C causing the photo-resist to become insoluble in the exposed areas again. Then the sample would be exposed to UV light without a mask, leading to the situation where only the areas exposed in step two are insoluble.
In Figure 3.5 the chromium mask is shown in proximity mode, i.e. the mask is held between $10-50\mu$m above the sample. This removes the risk of photo-resist sticking to the mask as opposed to the contact mode, where the mask is in contact with the sample.
In the case of etched samples, the samples were hard baked for 30 minutes at 250°C before reactive ion etching (RIE) in order to make the photo-resist more resistant to the etching, see subsection 3.2.5. For the UV written samples, an aluminum layer ($\sim 1\mu$m thick) was deposited on top of the photo-resist coated wafers. Only the aluminum deposited in the resist-free areas of the wafer remained when the photo-resist was removed in acetone.

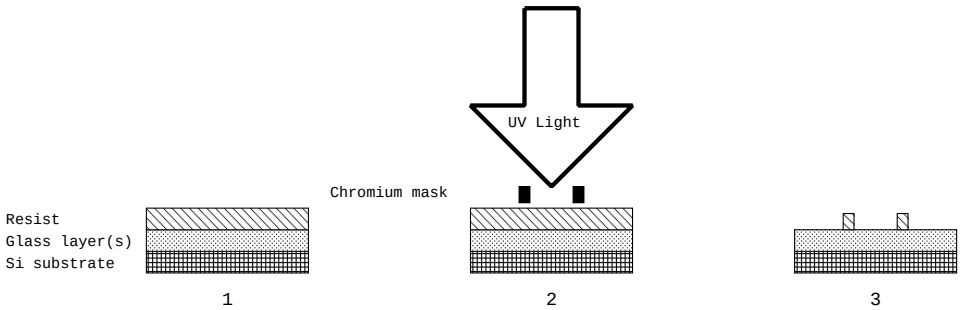

Figure 3.5: A schematic describing how the UV lithography is performed. The illustration is not to scale.

3.2.5 Reactive Ion Etching

The RIE transfers the photo-resist pattern to the core layer of the etched samples. RIE is performed in a reactor much like the PECVD chamber shown in Figure 3.3. The differences are that the substrate is not heated, the top electrode is a normal one, i.e. no inlet holes, and the process gases are different. A plasma is established by applying a high power RF signal to the top electrode while grounding the bottom electrode. The substrate is subsequently exposed to reactive radicals (like fluorine) generated from the process gases by the RF field.
Reactive ion etching has many advantages over wet etching. The RIE can perform vertical, anisotropic etching, directional etching and isotropic etching as illustrated in Figure 3.6, while only isotropic etching is possible using wet etching on amorphous materials [2]. The wet etching also has the problem with reproducibility of the etch rate. The isotropic etching with RIE is achieved at low ion energies, i.e. at high pressures. As the pressure is reduced, the ion energy increases to the regime where the material is mechanically ejected from the substrate yielding anisotropic etching. Between these two regimes, there exists a parameter space yielding directional etching which is desirable due to high etch rates and directional selectivity.
The etched samples in this thesis had their cores etched in an atmosphere of CHF_3, an RF power level of 200W and an RF frequency of 13.56MHz. The burned photo-resist was removed by etching in an O_2 atmosphere, 100W RF power and 13.56MHz RF frequency.

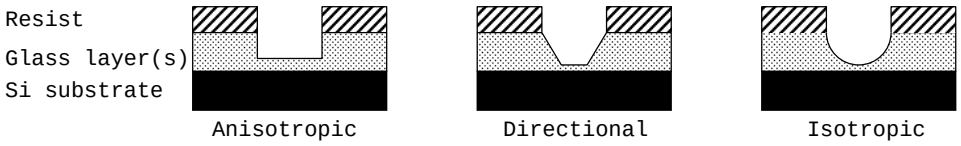

Figure 3.6: A schematic illustration of the different etching profiles possible using a RIE.

3.2.6 Characterization of thin films and samples

To characterize the deposited thin films and samples, three different instruments were used. The prism coupler was used to determine the refractive index and thickness of thin films, the TENCOR profilometer was used to measure the etched depth of waveguides and the scanning electron microscope (SEM) was used to take pictures of the samples with a resolution down to approximately 10-20nm.

[2] On some crystalline materials (e.g. Si) directional etching is possible using wet etching along the crystal axes.

Prism coupler

The prism coupler is an extremely simple device used to determine the refractive index and thickness of thin films as illustrated in Figure 3.7. It consists of a prism, with refractive index somewhat higher than the thin film, and a light beam (normally 632.8nm and/or 1550nm). If the air gap between prism and thin film is small enough, there is the possibility of power coupling from the prism to the thin film [69, Sect. 7.4]. For certain angles of the input beam, φ, the beam power will be transferred to the thin film and thus by varying the angle of the input beam and monitoring the output power, the refractive index and thickness of the thin film can be calculated from the minima in the reflectivity curve representing the different guided modes.

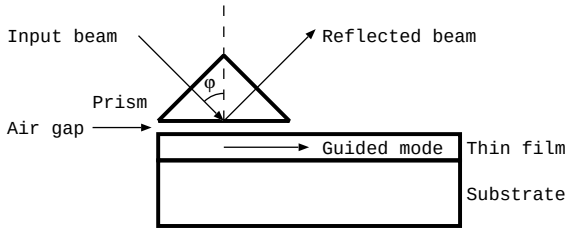

Figure 3.7: A schematic illustration of a prism coupler used to determine the refractive index and thickness of thin film.

Profilometer

The TENCOR profilometer consists of a probe (cone with sides angled 60° and tip radius of curvature 5μm) and is mostly used to determine etch depths. The probe is lowered down to the sample surface and scans the surface through a scanning routine. The height of the etched structures is determined within ±50nm. It is not possible to measure a profile accurately if the angles of the structure are above 60°.

Scanning Electron Microscope

A Scanning Electron Microscope (SEM) consists of an electron emitter, usually a tungsten crystal, across which a high voltage is applied. The extracted electrons are accelerated towards the sample by an anode. Some of the electrons hitting the sample are reflected back from the sample. Two detectors are present, the first monitors the electrons reflected back at right angles from the sample surface and the second monitors the electrons reflected at an angle. All SEM pictures in this thesis were made using the first detector described. The SEM pictures were used to determine etch depth, etch profile, layer thicknesses, sample dimensions, photo-resist thickness and profile.

3.2.7 UV writing of waveguides and Bragg gratings

As mentioned in the beginning of this chapter, germanium doping makes silica UV-photosensitive [24] enabling permanent changes in the refractive index of the core by UV laser radiation. The mechanism behind the germanium induced photo-sensitivity is not fully understood and several different models exist on this subject [36, 7, 22]. Reference [36] is a microscopic model describing the photo-sensitivity by an interaction between the UV light and the germanium oxygen deficient centers acting as gates for transferring the excitation energy into the silica. Reference [7] is a macroscopic model where the photo-sensitivity is explained by UV induced changes of the silica volume. Reference [22] describes the UV changes in the refractive index by the creation of GeE' centers, the so-called Color-Center model. Though the models are different, they are not mutually exclusive and are in fact describing the same thing through two different reference systems. The description of germanium induced photo-sensitivity will not be pursued further in this thesis.
To increase the UV-photo-sensitivity, hydrogen or deuterium loading can be used [39]. Deuterium is preferred over hydrogen since OH^- has a strong absorption peak around 1400nm with a tail into the telecommunication s-band [69, p. 181]. Deuterium has a larger mass and the resonance is thus moved to longer wavelength.
The laser source used in this thesis was a pulsed excimer laser using a gas mixture of krypton and fluorine. The emitted wavelength of the excimer laser is 248 nm. The energy is between $100 - 300$ mJ per pulse and the repetition rate of the laser is limited to 50 Hz. The pulse duration is approximately 20 ns yielding a pulse peak power of 15 MW. The excimer laser used in this thesis has been extensively studied by [27, 29] and the reader is referred to these for a more detailed description of the excimer laser system.

UV writing of waveguides

When writing waveguides with the excimer laser, the light was guided in free space using high power mirrors and lenses as seen in Figure 3.8. The lenses were mounted on a translation stage enabling movement of the beam in the direction of the waveguides to be written (the y-direction in Figure 3.8). Two lenses were used to focus the beam in the direction of writing. The first lens was focusing and had a focal length of $f1 = 500$mm. The second lens was expanding and had a focal length of $f2 = -200$mm. Separating the lenses by the distance $f1 + f2 = 300$mm yielded a collimated beam focussed by a factor $\left|\frac{f1}{f2}\right| = 2.5$ [23, Chap. 5].
The UV written samples were all deuterium loaded before UV exposure to increase the UV photo-sensitivity. The deuterium pressure in the loading

chamber was between 1700 and 2000psi (117 and 137bar). At room temperature, the equilibrium concentration of deuterium is [64] $c_{eq} = 116\frac{\text{ppm}}{\text{bar}} \cdot \text{p}$, where 1ppm $= 10^{-6}$ mole D_2 per mole SiO_2 and p is the deuterium pressure. Inserting the loading chamber pressures yields between 1.4 and 1.6 mole % D_2 in the samples. Using the diffusion constant governing in and out diffusion of deuterium in silica [38]

$$\text{D}_{\text{D}_2} = 2.28 \cdot 10^{-4} \cdot \exp\left(\frac{4838\text{K}}{\text{T}}\right)\frac{\text{cm}^2}{\text{s}} ,$$

where T is the sample temperature, together with equations in [65] yields a formula to calculate the time needed to reach 95% of c_{eq} called $\tau_{0.95}$. Inserting the thickness values of the samples used in this thesis yields that $\tau_{0.95}$ is reached after $\sim$ 14h for a 10μm thick sample and $\sim$ 31h for a 15μm thick sample. The normal loading time used in this thesis is approximately one week. After loading, the samples were kept at -80°C until UV exposure. The low temperature is necessary in order to reduce the out-diffusion of the D_2. Svalgaard [68] has found that the D_2 concentration decays in an exponential manner with a 1/e decay time of 11.8 hours at 23°C. The decay time $\tau(T)$ at temperature T can be written as

$$\tau(T) = ln(\alpha)\tau_0 \exp\left(\frac{4838\text{K}}{T} - \frac{4838\text{K}}{T_0}\right), \qquad (3.1)$$

where α is the remaining D_2 concentration, τ_0 is the decay time at temperature T_0. Using equation 3.1 and inserting 95% remaining D_2 at a temperature of -80°C one finds that at this low temperature it takes 155 days to loose five percent of the initial D_2 concentration.
The fluence used to write the waveguides in section 3.3 was either 2 $\frac{\text{kJ}}{\text{cm}^2}$ or 3 $\frac{\text{kJ}}{\text{cm}^2}$. No visible difference in waveguide properties were observed between the two different fluences. After the waveguide writing, the Al-mask was removed in phosphoric acid, 85% H_3PO_4, to prevent Al from the mask to sputter onto the phase mask during writing of the Bragg gratings described in the next section.

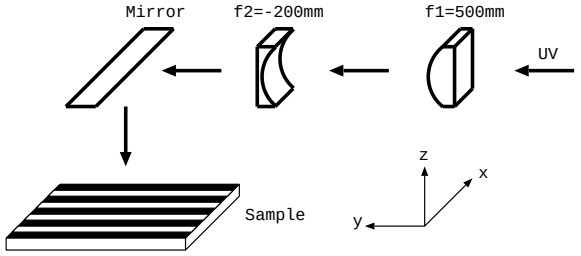

Figure 3.8: A schematic illustration of the setup used to UV write the waveguides.

UV writing of uniform Bragg gratings

The writing of the Bragg gratings in the samples was performed using the phase mask method described in [25] after out-diffusion of the D_2. The temporal coherence length of the excimer laser is of the order 30μm and the spatial coherence length is of the order 100μm. The laser is therefore only suited for Bragg grating writing using methods where only a short coherence length is required. The phase mask method relaxes the requirements on the coherence of the laser [29] compared to the holographic writing method presented in [50]. A simple schematic of the phase mask method is illustrated in Figure 3.9. Incident UV light traverses the UV transparent glass. In the bottom of the phase mask, a grating has been etched with period Λ. The height of the etched grating, h, is chosen, so a phase difference between light traveling in the glass and air is π after h. This gives destructive interference in the zeroth order ($m = 0$) diffracted light. The +1 and -1 order diffracted beams interfere and give a pattern (Bragg grating) in the waveguide beneath the phase mask. Light traveling in a waveguide with a Bragg grating will be reflected from the grating if it obeys the Bragg condition, equation 2.2

$$\lambda_{Bragg} = n_{eff} \cdot \Lambda \ , \tag{3.2}$$

where λ_{Bragg} is the wavelength of the light and n_{eff} is the effective index of the waveguide. The relation between $\Lambda = 2\Lambda_{\text{Grating}}$ has been used, i.e. that the periodic structure in the waveguide is half the period of the phase mask. An extra pair of non-spherical lenses were introduced to the setup when writing Bragg gratings to focus the beam in the direction perpendicular to the waveguides (the x-direction in Figure 3.8). The extra focusing lens had a focal length of $f3 = 500$mm and the extra expanding lens had $f4 = -250$mm. The extra set of lenses were separated by the distance $f3 + f4 = 250$mm. The beam was thus focussed by a factor of $\left|\frac{f3}{f4}\right| = 2$. In order to make the Bragg gratings uniform, the excimer beam was scanned across the phase mask with a constant velocity. The approximate fluence used to write the gratings was $200\frac{J}{cm^2}$.
The Bragg gratings made during this thesis were medium strength, i.e. $n_{mod} < 6 \cdot 10^{-5}$ [11] and approximately 2cm long, in order to make the Bragg grating a perturbation to the measurement.

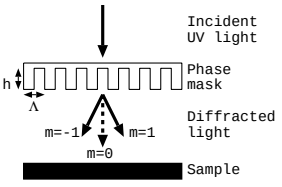

Figure 3.9: A schematic illustration of a phase mask and its use.

3.2.8 Final preparations

After writing the Bragg grating, the samples were annealed at 375°C. Small scratches were made on the back of the sample through the thermal oxide and filled with a silver containing paste in order to make an electric contact to the Si wafer. On top of the sample, an electrode of centimeter dimension was made with silver paste to cover the region with the Bragg gratings.

3.3 UV written waveguides

This section gives an overview of the UV written waveguides, i.e. the deposited layers, the refractive indices of the layers, their thicknesses and the anneal procedures and times used.

3.3.1 UV written samples with low PDL

The first UV written samples made in this thesis were made in order to test the polarization dependence of $\chi^{(3)}$ and thus low polarization dependent loss (PDL) was required. This was obtained by increasing the buffer layer thickness compared to the one used in a previous study [6]. In Figure 3.10, a schematic view of the UV written samples is presented. It consists of a thermal oxide buffer layer (TOX), PECVD deposited core layer (Ge:SiON) and pure silica top-cladding (SiO_2). The core and top-cladding layers were deposited in one step. Content estimation of the core layer dopants yields 5.9 atomic% (18.9 molar%) Ge and 4.5 atomic% (3.2 molar%) N [6]. The content estimation measurements in [6] were performed using Secondary Ion Mass Spectrometry. In Table A.2, the refractive indices and thicknesses, measured using the prism coupler, of the different layers in the UV written samples are presented. The core and top-cladding layers of the samples made in this batch were all annealed in an atmosphere of N_2 at 800°C for two hours in one step.
The mask used for these samples was a dark field (negative process) mask. The waveguides were all nominally seven micrometer wide and separated by 250μm.

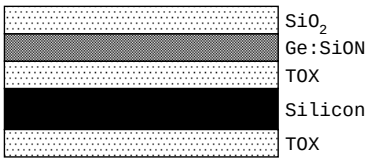

Figure 3.10: A schematic illustration of a UV written sample.

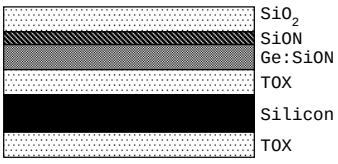

Figure 3.11: A schematic illustration of a UV written sample with a trapping layer made from SiON.

3.3.2 UV written samples with trapping layer

Another type of UV written samples used in this thesis were samples with a trapping layer as seen in Figure 3.11. The intention was to increase the frozen-in electric field using an extra layer to trap charges during poling. Four different versions of this type of sample were made. One type had a high refractive index SiON trapping layer deposited directly on the core layer, a second type had low n SiON on the core layer. The third type had a thin SiO_2 buffer layer in between the core layer and a high n trapping layer. The fourth type had a thin buffer layer between the core and a low n trapping layer.
In the samples without a buffer layer, the thickness of the trapping layer was chosen so that only a small amount of the guided light was coupled into it. The buffer layer serves two purposes: First, it reduces the amount of light coupled into the trapping layer by separating it from the core and secondly, it serves as a test to see if this structure is advantageous compared to the samples without the buffer layer.
These samples had their core layer annealed in nitrogen at 800°C for four hours and after the deposition of the trapping and top-cladding layers, they were annealed using the same program. The mask used for the samples with a trapping layer was a dark field mask. The mask was divided into blocks with 500μm between each block. Each block consisted of four waveguides of either four, six or eight micrometer width. The inter-waveguide spacing was 125μm.
In Table A.3, the layer structure of a sample of type one is given, type two is given in Table A.4, type three in Table A.5 and type four in Table A.6.

3.4 Etched waveguides

In the same way as above, this section gives an overview of the etched waveguides. Three different batches of etched samples were made and they are described below. Generally for the etched waveguides the core layer was deposited using PECVD on a TOX layer and annealed. After annealing, UV lithography was performed defining the waveguides in the photo-resist. Subsequently, the core was etched in the RIE followed by top-cladding deposition in the PECVD chamber. In the case of soft top-cladding, a thin buffer layer (approximately 0.4μm thickness) consisting of pure silica is made to separate the core and the top-cladding. The buffer layer prevents unwanted reaction between the boron/phosphor in the cladding and the germanium in the core and also reduces the change in optical properties of the core as a result of in-diffusion of boron and phosphor. Finally, the top-cladding was annealed.
In the samples with soft top-cladding annealed at 1000°C, the total height of the deposited layers is not the sum of the thin film thicknesses, since the

core is etched and the top-cladding flowed. In this case, the total height is approximately the sum of the top-cladding and the buffer layer.

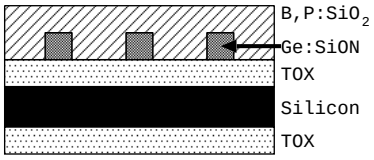

Figure 3.12: A schematic illustration of a sample where the waveguides are etched and the top-cladding is soft. A thin pure silica layer is deposited between the core and top-cladding, but not shown in the illustration.

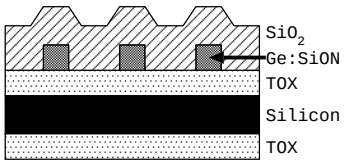

Figure 3.13: A schematic illustration of an etched sample with hard top-cladding.

3.4.1 Batch one

This batch of samples was made to test whether the UV fluence used in the UV written samples had an effect on $\chi^{(3)}$. Since the waveguides in this batch were etched, the only UV fluence the samples were subjected to was the small (compared to the fluence used to make the UV-written waveguides) UV fluence used to make the Bragg gratings. The measurements on the low PDL samples had indicated such a relation.
The first batch of samples was made using low temperature anneal of core and top-cladding, 800°C for two hours (core) and four hours (top-cladding). Some samples had hard and some soft top-cladding. Since the hard top-cladding is not able to flow in the anneal step and since the temperature is too low to flow the soft top-cladding, the schematic view of these samples is presented in Figure 3.13. Tables A.7 and A.8 display the refractive indices and thickness of the different layers in this batch of samples. The mask used for this batch was a light field (positive process) mask. Blocks of waveguides, width four, six, eight and ten micrometer (inter-waveguide distance 125μm), were separated by 250μm.

3.4.2 Batch two

The samples made in this batch with flow-rates for $NH_3 = 250$sccm [3] and $GeH_4 = 2$sccm were annealed wet at 1100°C for four hours. The samples made with flow-rates of $NH_3 = 100$sccm and $GeH_4 = 3$sccm were annealed dry at 1000°C for four hours. The top-cladding consisted of $B, P : SiO_2$ glass annealed wet at 1000°C for four hours. The batch was made to check the UV influence on $\chi^{(3)}$ and to increase the knowledge on fabrication of etched waveguides. The structure of this batch of samples is seen in Figure 3.12 and

[3] sccm=standard cubic centimeters per minute.

the refractive indices and thicknesses of the thin films are given in Tables A.9 and A.10.

3.4.3 Batch three

This batch was made to investigate the influence of nitrogen on $\chi^{(3)}$. Therefore, the samples were subjected to the same anneal type, dry N_2 atmosphere for 12 hours at 800°C followed by four hours at 1000°C as described in subsection 3.2.3, but different flow-rates of NH_3 during PECVD growth of the core layers. Top-claddings were annealed wet at 1000°C for four hours and the resulting sample structure is seen in Figure 3.12. The sample presented in Table A.11 had zero flow-rate of NH_3, the one in Table A.12 had 100sccm NH_3 flow-rate, in Table A.13 the sample had 175sccm NH_3 flow-rate and in Table A.14 the sample had 250sccm NH_3 flow-rate. The samples all had a GeH_4 flow-rate of 2sccm.

Chapter 4

Experimental Setup

4.1 Introduction

This chapter gives an introduction to the experimental setups used in this project. In section 4.2, the setup used to thermally pole the samples is described and in section 4.3, the setup used to measure $\chi^{(3)}$ and E_{int} using a Bragg grating is presented. In section 4.4, a comparison with a competing experimental method used to determine nonlinearities in silica glass is given.

4.2 Thermal poling

The thermal poling performed in this thesis was made by heating the sample on a heating plate while applying a large electric field across it. The sample was heated to the poling temperature, which was either 357°C or 375°C. When the desired temperature was reached, the poling voltage was applied to the top-electrode of the sample and the Si wafer was used as back-electrode, grounded through the heater. If the voltage applied to the top-electrode is negative, the poling is called negative thermal poling and if a positive voltage is applied, the poling is called positive thermal poling. Typically, the poling voltage was between -2kV and -2.5kV, but the maximum voltage that can be applied across the sample varies from sample to sample. The parameters, poling temperature and voltage, have been optimized by [59] for the waveguides used in this thesis. The temperature and poling voltage was maintained during the poling time, which usually was 15-30 minutes. After this period of time, the heater was turned off and the sample was allowed to cool down still having the poling voltage across it. When the sample temperature reached approximately 100°C, the high voltage was turned off and the sample cooled down to room temperature. A schematic of the poling setup is shown in Figure 4.1.

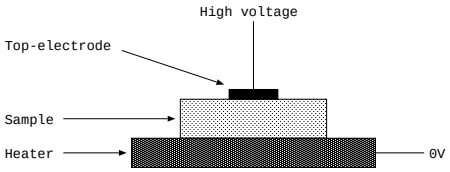

Figure 4.1: A schematic illustration of the thermal poling setup.

4.3 Bragg gratings as probes to find $\chi^{(3)}$ and E_{int}

The experimental setup, used to determine $\chi^{(3)}$ and E_{int} by measuring the change in resonance wavelength of a Bragg grating, is shown in Figure 4.2. Light from a source, illustrated as a tunable laser (TLS), passed through a polarization controller, where the wanted polarization was chosen. The light travels in the z-direction in Figure 4.2. When the electric field component is in the y-direction in Figure 4.2, i.e. in the film plane, the polarization is called Transverse Electric (TE), since the E-field is perpendicular to the H-field vectors. When the magnetic field component is in the y-direction, the polarization is called Transverse Magnetic (TM), since the H-field is perpendicular to the E-field vectors. In the case where the light source was an erbium doped fiber amplifier, a polarizer was included in the setup between the source and the polarization controller. This step was not necessary when using the tunable laser source due to its highly polarized output. From the polarization controller, the light was coupled into the planar waveguide of the sample using a translation stage. After the sample, the light was coupled out into the setup again and into an optical spectrum analyzer (OSA) where a transmission spectrum was recorded.

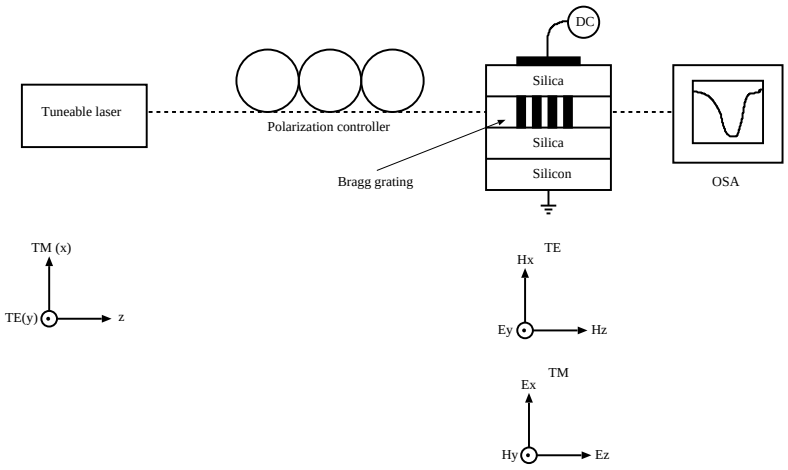

Figure 4.2: A schematic illustration of the experimental setup.

Transmission spectra were recorded with different voltages applied across the sample for both polarizations before and after poling. Typical transmission spectra are shown in Figure 4.3.
Birefringence is seen in the figure and the size of it is

$$\Delta \mathrm{n}_{\mathrm{eff}}^{\mathrm{total}} = \frac{\lambda_{\mathrm{Bragg}}^{\mathrm{TE}} - \lambda_{\mathrm{Bragg}}^{\mathrm{TM}}}{\Lambda} \sim -4.7 \cdot 10^{-4} \tag{4.1}$$

and is due to compressive stress in the grown layers. $\Delta \mathrm{n}_{\mathrm{eff}}^{\mathrm{total}}$ consists of two contributions: The geometrical birefringence, found through simulations [71] $\Delta \mathrm{n}_{\mathrm{eff}}^{\mathrm{geo}} \equiv \mathrm{n}_{\mathrm{eff}}^{\mathrm{TE}} - \mathrm{n}_{\mathrm{eff}}^{\mathrm{TM}} \sim 3.8 \cdot 10^{-4}$ and the stress-related birefringence $\Delta \mathrm{n}_{\mathrm{eff}}^{\mathrm{stress}} \sim -9.1 \cdot 10^{-4}$ found from calculations following reference [75] and [49]. Clearly, the stress-related birefringence is the dominant birefringence term. Calculating the total birefringence from the geometrical and stress-related birefringence terms yields $\Delta n_{eff}^{total} = n_{eff}^{geo} + n_{eff}^{stress} \sim -5.2 \cdot 10^{-4}$ in accordance with the value found experimentally (equation 4.1).
The polarization dependent loss is low, $PDL < 1$dB, since the buffer layer is sufficiently thick to prevent the TM mode to probe the silicon wafer allowing for both polarizations to be examined.
In the setup, the position of the Bragg wavelength was measured versus the externally applied DC electric field, E_{ext}. Since the Bragg wavelength and the effective refractive index are related by equation 3.2, the change in Bragg wavelength as function of E_{ext} can be written as $\Delta\lambda_{Bragg}(E_{ext}) = \Lambda \cdot \Delta n_{eff}(E_{ext})$. Using equation 2.14 and fitting $\Delta\lambda_{Bragg}(E_{ext})$ with a parabola yields:

$$\begin{aligned} \Delta\lambda_{Bragg}(E_{ext}) &= \frac{3\Lambda\chi^{(3)}E_{int}^2}{2n} + \frac{\Lambda\chi_{eff}^{(2)}}{n}E_{ext} + \frac{3\Lambda\chi^{(3)}}{2n}E_{ext}^2 \\ &= A + BE_{ext} + CE_{ext}^2 \ . \end{aligned} \tag{4.2}$$

The phase-mask pitch is $\Lambda = \frac{A}{n}$ and therefore E_{int} and $\chi^{(3)}$ can be found from

$$E_{int} = \frac{B}{2C} \quad \text{and} \quad \chi^{(3)} = \frac{2n^2C}{3A} \ . \tag{4.3}$$

4.4 Competing method(s)

In this section, other experimental setups used to determine the nonlinearities of silica glass are presented and compared to the method described in this thesis. Subsection 4.4.1 describes a method used for waveguides and fibers and subsection 4.4.2 describes a method used for bulk material. In subsection 4.4.3 a comparison between the Bragg grating method and the

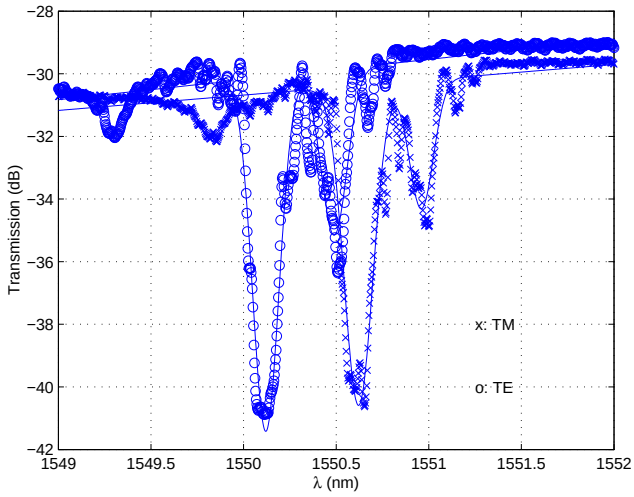

Figure 4.3: Typical transmission spectra for a sample (UV written).

Mach-Zehnder interferometer method is made and in subsection 4.4.4 the main problem of the Bragg grating method, namely in-coupling to the planar waveguides, is illustrated.

4.4.1 Waveguides and fibers

Mach-Zehnder interferometric (MZI) setups are used by references [5, 59, 19] to determine the electro-optic Kerr coefficient $\chi^{(2)}(\omega;\omega,0)$ in silica waveguides and fibers. In [8] an MZI setup is used to determine the DC Kerr coefficient $\chi^{(3)}(\omega;\omega,0,0)$ and the electro-optic Kerr coefficient in silica glass fibers. A simplified MZI setup is illustrated in Figure 4.4. Light from the source is split up into the two arms of the MZI via a 3dB coupler. The upper arm acts as reference and is made up of a $LiNbO_3$ modulator. The lower MZI arm consists of the sample, modulated by an AC signal or by an AC and DC signal. As the light interferes at the second 3-dB coupler, the output signal will depend on the phase relation between the signal in the two arms. The phase dependence is controlled by the AC (or AC+DC) voltage. From the measured phase shift, the nonlinearities can be calculated.
In the case where the signal generator only generates an AC signal, only the second-order nonlinearity $\chi^{(2)}(\omega;\omega,0)$ can be found as seen in [5, 59, 19]. When a DC and an AC signal are generated, both $\chi^{(2)}(\omega;\omega,0)$ and $|\chi^{(3)}(\omega;\omega,0,0)|$ can be found as seen in [8].
The advantage of the MZI setup is its sensitivity and speed. The phase shift between the two arms can be determined very precisely and fast, yielding the value of $\chi^{(2)}(\omega;\omega,0)$ (and $\chi^{(3)}(\omega;\omega,0,0)$).
At the same time, the greatest disadvantage of the MZI setup is its sensitivity. The setup is very sensitive to temperature changes and vibrations in the

surroundings. Vibrations will modulate the transmitted intensity through the sample, which could be misinterpreted as a phase shift between the two signals interfering at the second 3dB coupler. Temperature gradients will not affect the MZI setup if they are constant in time, since it only yields a fixed change in the path length of the light. Temperature changes during measurement changes the path length of the two arms and thus the phase-shift.
Another disadvantage is the complexity of the setup, especially when both a DC and an AC signal have to be supplied to the sample.

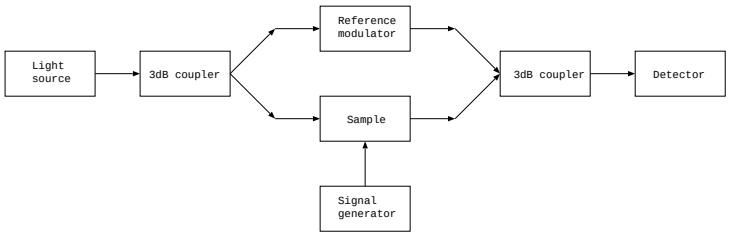

Figure 4.4: A simplified schematic of an MZI setup.

4.4.2 Bulk material

To determine the second- and third-order nonlinearities in bulk silica, an MZI setup can be used (described above) as done in reference [41]. The advantages and disadvantages are as described above. An extra advantage is that is is possible to make very clean bulk silica samples which can take high poling voltages. An extra disadvantage is that free space optics have to be used to couple light into the samples.

4.4.3 Comparison

The Bragg grating setup has the advantage that it is very simple compared to the MZI setup but it also requires an extra preparation step, namely the writing of the Bragg grating which is unnecessary in the MZI setup.
The limiting factor of the sensitivity in the Bragg grating method is the precision in the determination of the Bragg wavelength. Therefore, medium strength Bragg gratings with small FWHM are used, since they do not reach the noise floor of the OSA and the center of the Bragg grating is precisely determined. The maximum resolution of the detection system (TLS and OSA) used in this project is 1pm [3].
Vibrations in the surroundings should in theory not be a problem in the Bragg grating setup since λ_{Bragg} does not depend on the transmitted, low power, signal. Temperature changes during measurements will be a problem in this setup, since λ_{Bragg} is a function of temperature as seen in [55, p. 99]

$$\Delta\lambda_{Bragg} = \lambda_{Bragg}(\alpha_\Lambda + \alpha_n)\Delta T \ , \tag{4.4}$$

where $\alpha_\Lambda \sim 0.6 \cdot 10^{-6}/K$ is the thermal expansion coefficient (of a silica fiber) and $\alpha_n \sim 8.6 \cdot 10^{-6}/K$ is the thermo-optic coefficient (of a Ge-doped silica fiber core). Thus, a constant temperature during the measurements is important. The effect of a temperature gradient depends on the direction of the gradient. In the direction of the grating (waveguide), a temperature gradient can infer a chirp in the uniform grating since the gradient will change the effective refractive index along the waveguide and the grating in this direction has a macroscopic dimension (cm). In the two directions perpendicular to the waveguides a temperature gradient will have a limited effect due to the small dimensions of the core $\lesssim 8 \cdot 8\mu m^2$ over which the temperature has to change significantly. The only effect of a temperature gradient in these directions will be an induced birefringence.

4.4.4 In-coupling

The biggest problem facing the Bragg grating method is the possible misalignment of the in-coupling from the fibers into the planar waveguides. A slight misalignment will yield a voltage dependent transmission and Bragg grating form as illustrated in Figure 4.5. This misallignment will result in incorrect measurements of the nonlinearities and frozen-in field. Since the MZI method does not depend on a Bragg grating, this method is less dependent on the in-coupling into the waveguides. Bad in-coupling will only mean a worse signal-to-noise ratio due to the lower transmission.

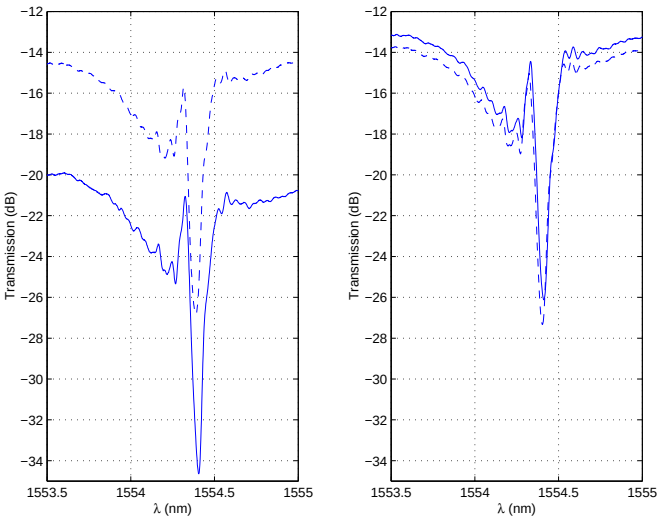

Figure 4.5: A figure illustrating the effect of good (right) and bad (left) in-coupling. The dashed curves have been measured at 0V and the solid lines represent the measurements performed at -2kV. The measurements represent the TM polarization of sample #65.

Chapter 5

Results

5.1 Introduction

In this chapter, the results obtained in the project are presented. In section 5.2, the second- and third-order nonlinearities and the frozen-in field are found using the Bragg grating method. In section 5.3, the method is used to analyze a sample in which both polarizations are measurable. Possible explanations to the observed transmission spectra are given. A similar sample is analyzed in section 5.4, where the optimized poling parameters found by [59] have been used and the impact of these poling parameters is described. Section 5.5 contains the analysis of samples with soft top-cladding. In section 5.6, the influence of UV fluence and thermal poling on $\chi^{(3)}$ is investigated. In section 5.7, samples with etched core and hard top-cladding are analyzed. The influence of the NH_3 flow-rate on the third-order nonlinearity is examined in section 5.8. Section 5.9 describes other possible explanations to the observed transmission spectra and in section 5.10, samples containing a trapping layer are investigated.

5.2 Measurements using a Bragg grating

In this section, the first sample investigated using the Bragg grating method is presented and the results obtained from the measurements are analyzed. The sample was made by [6] and the composition is described in section A.1. To determine the internal electric field and the second- and third-order nonlinearities of a sample using the Bragg grating method, the transmission spectrum is measured for different applied voltages across the sample before and after poling for both polarizations (where possible). Each transmission spectrum is fitted with one or more Gaussian functions in a logarithmic plot, one Gaussian function for each transmission dip in the waveguide, as illustrated in Figure 5.1. From the Gaussian fit, the center wavelength of the Bragg grating is determined. The so-called Bragg wavelength is subse-

quently plotted versus the externally applied DC voltage and fitted with a parabola as illustrated in Figure 5.2 for the transmission dip in Figure 5.1.

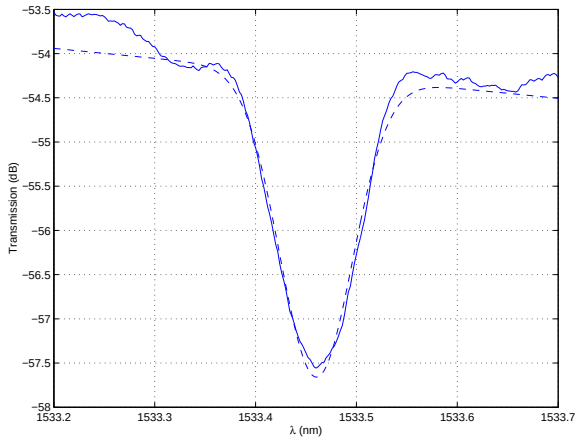

Figure 5.1: A transmission spectrum of a UV written sample with thin buffer layer, solid line, fitted with a Gaussian function, dashed line.

It is important to note that the error-bars presented in Figure 5.2 (and in all subsequent parabolic plots) are over-estimates since they are determined as the Root-Mean-Square (RMS) difference between the spectrum and the Gaussian function given in equation 2.6. This yields a larger error than if the spectrum had been fitted with the correct function. Since all the spectra are fitted with Gaussian functions, this gives a systematic over-estimation of the error in the determination of the Bragg wavelength, λ_{Bragg}. This over-estimate does not influence the parabolic fit as the error in the parabolic fit is determined as RMS. This approximation for the error is valid as long as the number of points fitted with the parabola is large.

Due to the thin buffer layer of this sample, only the TE polarization can be measured. The TM polarization is absorbed by the Si wafer and is thus reduced by more than 30dB compared to the TE polarization. Thus only the TE polarization is analyzed for this sample.
The sample n4 was poled using a poling voltage of -2kV and a temperature of 375°C for 16 minutes [1]. Inserting the coefficient of the parabolas into the equations derived in sections 2.5.1 and 4.3 yields the frozen-in DC electric field $E_{int} = \frac{B}{2C}$, the second-order nonlinearity $\chi^{(2)}_{eff} \equiv \frac{n^2 B}{A}$ and the third-order nonlinearity $\chi^{(3)} = \frac{2n^2 C}{3A}$. The measured values of sample n4 are presented in Table B.1. From the table and from Figure 5.2 it is evident that a frozen-in field has been induced into the sample during poling since the lowest point of the parabola is shifted from $\sim$ 0V to ~ -1000V. The

[1] This sample was analyzed in [43].

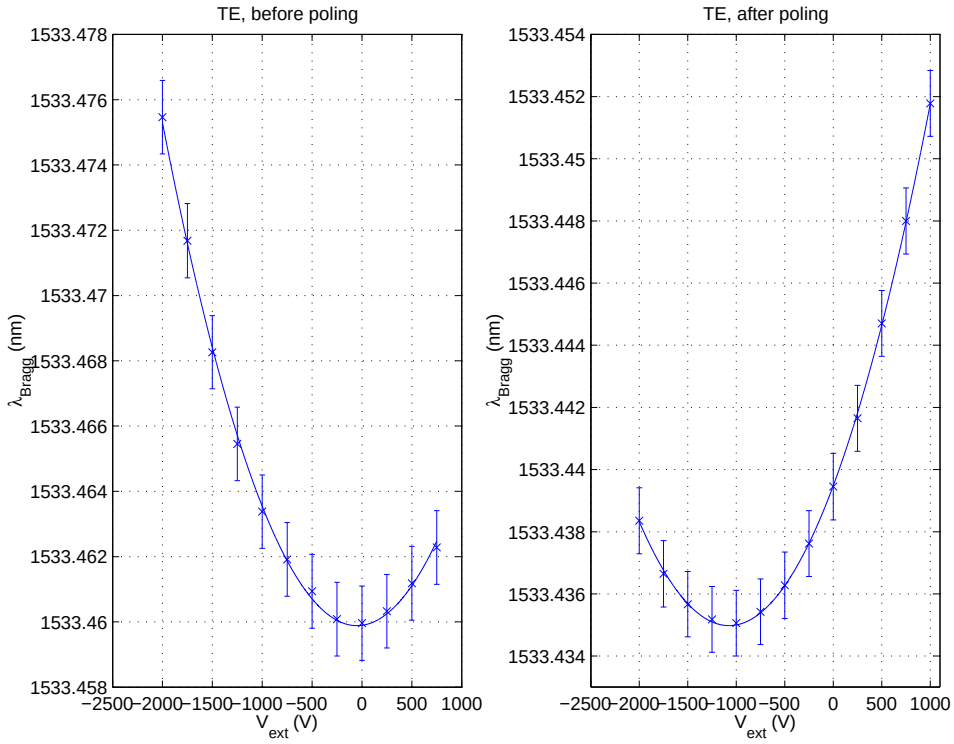

Figure 5.2: The Bragg wavelength, λ_{Bragg}, plotted versus the externally applied DC voltage, V_{ext}. The transmission spectrum of the sample is shown in Figure 5.1. x represents the center of the Bragg grating, the vertical lines represent the uncertainties and the solid line the parabolic fit.

measured built-in field is found to be approximately $122\frac{V}{\mu m}$.

5.2.1 The high values of $\chi^{(3)}$ found for sample n4

For pure silica Liu *et al.* find the DC third-order nonlinearity $\chi^{(3)} = 1.9 \cdot 10^{-22}\frac{m^2}{V^2}$ [41, 40]. Since the sample has been doped with germanium and nitrogen, it would be natural to expect an $\chi^{(3)}$ value different from the pure silica value. According to Boskovic *et al.* [9] and Philen *et al.* [56], germanium doping increases the optical Kerr effect coefficient (measured at $1.55\mu m$)

$$n_2 = \frac{3\eta_0}{4n^2}\chi^{(3)} \ , \tag{5.1}$$

where η_0 is the impedance of free space ($\sim 377\Omega$). For a sample containing 21 molar% Ge in the core and no fluor in the cladding, [9] finds $n_2 = 2.67 \cdot 10^{-20}\frac{m^2}{W}$. This value is for a core with a diameter of $2.07\mu m$ and a mode field diameter of $4.92\mu m$. Calculating the confinement factor yields $c = 0.3$. From $n_2 = c \cdot n_{2,Ge:SiO_2} + (1-c) \cdot n_{2,SiO_2}$ the optical Kerr coefficient

for Ge doped silica is found to be $n_{2,Ge:SiO_2} \sim 3.9{\cdot}10^{-20}\frac{m^2}{W}$ and inserting into equation 5.1 yields $\chi^{(3)} \sim 3.0 \cdot 10^{-22}\frac{m^2}{V^2}$. This value is identical to the DC third-order nonlinearity found for Ge doped silica in section 5.8. In Table 5.1 $\chi^{(3)}$ values found by different authors measured at different frequencies are displayed. From the table it is evident that germanium doping of the core increases the third-order nonlinearity. The sample from section 5.8 displayed in the table has a lower germanium concentration (2sccm GeH_4 flow-rate) than the sample in this section, n4, and than the samples in sections 5.3 and 5.4 [2], and one should therefore expect these samples to have a higher third-order nonlinearity due to the germanium doping. On the other hand, the samples n4, A2 and A8 also contain nitrogen in the core and as will become clear in section 5.8 doping with nitrogen reduces the third-order nonlinearity. According to the equation in section 5.8, the reduction of the third-order nonlinearity in samples n4, A2 and A8 due to nitrogen is $\sim 0.7 \cdot 10^{-22}\frac{m^2}{V^2}$.

	[41, 40] (DC)	[9]($1.55\mu m$)	This thesis (DC)
$\chi^{(3)}_{SiO_2} 10^{-22}\frac{m^2}{V^2}$	1.9	1.6	—
$\chi^{(3)}_{Ge:SiO_2} 10^{-22}\frac{m^2}{V^2}$	—	3.0 (21 mol%)	3.0 ± 0.24 ($\sim$ 15mol%)

Table 5.1: $\chi^{(3)}$ measured at different frequencies by different groups for different glasses.

5.2.2 Conclusion

The main results obtained by measuring on sample n4 was that the buffer layer has to have a certain thickness ($> 3.2\mu m$) in order for the sample to sustain the TM polarization. Secondly, the high third-order nonlinearity can be explained by the core dopants, namely Ge and N. Thirdly, it was observed that a frozen-in field was induced into the sample during poling. The size of the second-order nonlinearity obtained through equation 2.15 was of the same order of magnitude obtained using the MZI setup on similar samples in [6]. Finally, the third-order nonlinearity is seen not to change during thermal poling, indicating that the charge separation model is valid. This result is in accordance with results obtained by [72] and [32] whose measurements also indicate that the charge separation is valid.

5.3 Low PDL sample

In this section, a sample having a thick buffer layer is analyzed. As seen in section 5.2, samples having a thin buffer layer ($< 3.2\mu m$) are not able to

[2] All three having 18.9 mol% germanium content obtained using a flow-rate of 3sccm GeH_4.

support the TM polarization. Therefore, one of the first steps in this project was to make samples that were able to support both polarizations and to analyze the results obtained.
In Figure 5.3, the transmission spectra for the sample A2 are presented. The sample composition is presented in section 3.3.1 and the refractive indices and thicknesses of the different layers are shown in Table A.2. The parabolas fitted to the measurements are shown in Figures 5.6 and 5.7 for the low- and high-wavelength transmission dips in Figure 5.3, respectively. As seen in these two figures, two measurements were made at 0V. From the two 0V measurements it is evident that the Bragg wavelength is very well determined in the setup and does not change significantly over short periods of time, less than approximately 1pm in 3 minutes. The measured results are presented in Table B.2.

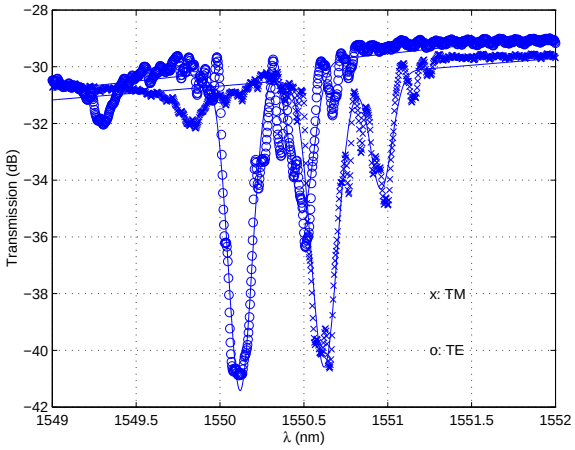

Figure 5.3: A transmission spectrum of a UV written sample. x represents the TM polarization and o the TE polarization. The solid lines represent the Gaussian fits.

The sample A2 discussed in this section was poled at -2kV and 375°C for 16 minutes [3]. As expected, an internal electric field is built into the sample during poling. The built-in field is in the range 87-121$\frac{V}{\mu m}$ depending on the transmission dip analyzed. The discrepancy between E_{int} for the two polarizations is negligible as expected for light traveling in a well-guided core. The size of the built-in field for the low-transmission dip is of the same order of magnitude as the one measured for sample n4 in section 5.2 as was expected since the 1) poling voltage, 2) temperature and 3) time were identical for the two samples.
Naively, one would expect the two transmission dips to represent two different modes, i.e. the fundamental and the first order modes. That would explain the difference in the measured third-order nonlinearity between the high and low wavelength transmission dips. Since the different modes probe

[3] This sample was analyzed in [44].

different parts of the waveguide and cladding and since the third-order nonlinearity is different for the different glass types (see [56, 41, 40]), one would expect a difference in the third-order nonlinearities determined by different modes. This would also explain the different measured frozen-in fields in the case where there is a big difference in confinement factor between the fundamental and the higher order mode [4].
Simulations of the waveguides in [71] indicate a wavelength difference between the fundamental and first order modes of the order of $\Delta\lambda_{calc} \sim 4nm$. Therefore, it is very unlikely that the two transmission dips in Figure 5.3 represent two different modes, since $\Delta\lambda_{meas} \sim 0.34nm \ll \Delta\lambda_{calc}$ and the high wavelength mode (the presumed fundamental mode) is weaker than the low wavelength mode (the presumed first order mode). This is not consistent with the fact that the Bragg grating is in the UV sensitive core and thus predominantly observed by the fundamental mode.
Another possible interpretation of the two transmission dips is that the small dip is a side-lope and the strong transmission dip is the fundamental mode of the uniform Bragg grating. In Figure 5.4, two simulated transmission spectra are shown. The dashed line represents a uniform Bragg grating with abrupt termination of the index modulation amplitude and the solid line represents a uniform Bragg grating with tapering of the refractive index modulation amplitude at the entrance and exit of the grating. As seen in the figure, the side-lopes are suppressed by tapering the ends of the uniform grating. The tapering is realized by starting and ending the scan on the phase mask. In both cases, the transmission spectrum shown in Figure 5.3 is not reproduced since the spectra in Figure 5.4 are symmetric around the center of the Bragg grating.

In Figure 5.5, the refractive index change is plotted versus the D_2 concentration. The measurement was performed by K. Færch *et al.* and is an extended measurement of the one published in [13] performed on UV written waveguides made in a germanium and boron doped core glass. Several waveguides are written in sequence and the time from taking the sample out of the freezer is recorded. After waveguide fabrication, the remaining D_2 is out-diffused by placing the sample on a heater. Subsequently, weak Bragg gratings are made in the samples to determine the effective refractive indices of the different waveguides. The D_2 concentration dependence on the time out of the freezer is determined through outdiffusion experiments thus yielding the effective refractive index versus D_2 concentration. Since it is not known how the refractive index changes as a function of the D_2 concentration, two fits have been presented in the figure. The first fit is an exponential decay and the second is a linear fit with a minimum D_2

[4] In the case where the confinement factors are alike the different modes would approximately probe the same parts of the sample and the measured E_{int} would be the same.

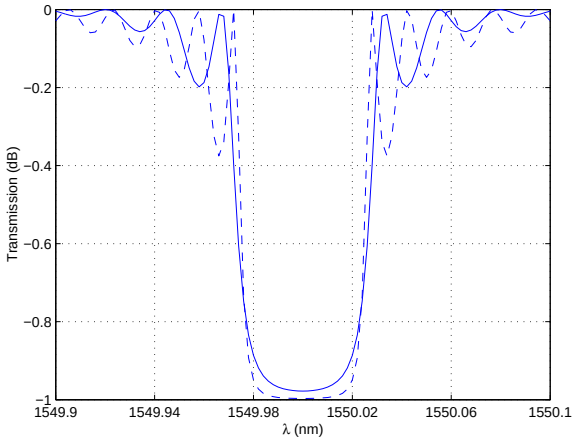

Figure 5.4: Transmission spectra of two uniform gratings, one with a tapering of the refractive index modulation amplitude at the entrance and exit of the grating (solid line), the other with abrupt termination (dashed line).

concentration of 1.17 molar% needed to change the refractive index. Other functions describing the refractive index are possible. In [14] measurements for high contents of H_2 are performed and the refractive index change is a step-like function of the H_2 pressure. Assuming a step-like behaviour, the transmission spectrum in Figure 5.3 can be explained in the following way: In the beginning of the waveguide writing, the refractive index change is due to the germanium doping and the D_2 sensitization. At some point of the waveguide writing, the D_2 concentration reaches a level below the minimum value required to make refractive index changes due to D_2 and from this point on, the refractive index change is only due to the germanium in the sample. The latter part of the waveguide will have a relatively lower refractive index. A Bragg grating made in the waveguide after out-diffusion of the deuterium will thus have two transmission dips. One from the high refractive index part of the waveguide and one from the low refractive index part. In the case where the D_2 concentration drops below the minimum required D_2 concentration fast, the high wavelength transmission dip will be much weaker than the low wavelength dip as seen in Figure 5.3. It is important to note that both dips represent the fundamental mode and thus they should yield the same value for the third-order nonlinearity. As will be seen later in section 5.9, this is not the only possible explanation to the two transmission dips observed because the high wavelength transmission dip also occurs in some etched samples.

As seen in Figure 5.7, the measurements on the Bragg wavelength of the high wavelength transmission dip are not as well determined as λ_{Bragg} of the low wavelength transmission dip presented in Figure 5.6 and thus the low wavelength transmission dip is used in the discussion below. The high

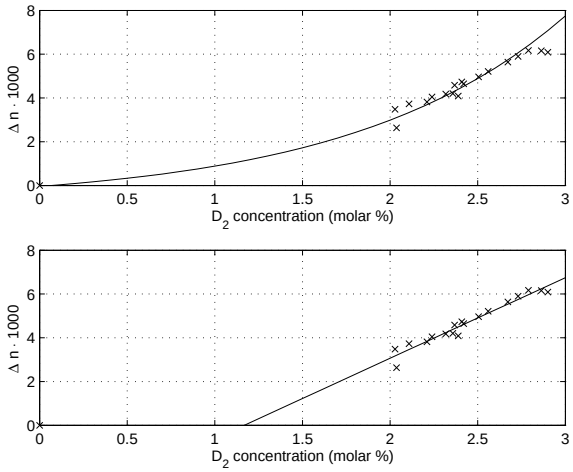

Figure 5.5: The refractive index change as a function of the D_2 concentration in the glass denoted by x's and an exponentially decaying function fitted to the measurement, solid line in the top figure, and a linearly fit, solid line in the lower figure.

wavelength dip results for this sample are disregarded.

The third-order nonlinearity is seen not to change within the uncertainty during poling, indicating that the charge separation model is the valid model. Inserting the induced second-order nonlinearities into equation 2.13 yields $\gamma \sim 1.24 \pm 0.02$ as seen in Table B.3. As mentioned in section 2.5 a value of three is expected in the case of charge separation (or in the case of dipoles in an external field lower than $E_{ext} = 5400\frac{V}{\mu m}$). The maximal external field applied across this sample was $180\frac{V}{\mu m}$, significantly lower than this value. Electrostriction, as described in subsection 2.5.3, can explain the observed discrepancy between the theoretical and measured γ-values. The measured α-values, defined in equation 2.20, of sample A2 are presented in Table B.4. The measured values are in accordance with the values predicted in [20] and thus electrostriction is a very plausible explanation to the observed γ-value. Another explanation to the measured γ-value is anisotropy of the third-order nonlinearities as is also observed in Table B.2. One would expect an isotropic third-order nonlinearity in a Kerr medium. Anisotropic third-order nonlinearities would change the $\gamma = 3$ value.

5.3.1 Conclusion

In this section, it was shown that having a sufficiently thick buffer layer permits the investigation of both the TE and TM polarization of the sample since the TM polarization is not leaking into the Si wafer. Secondly, the frozen-in electric field is comparable to the one obtained for sample n4 in section 5.2. This is expected since the two samples were poled using

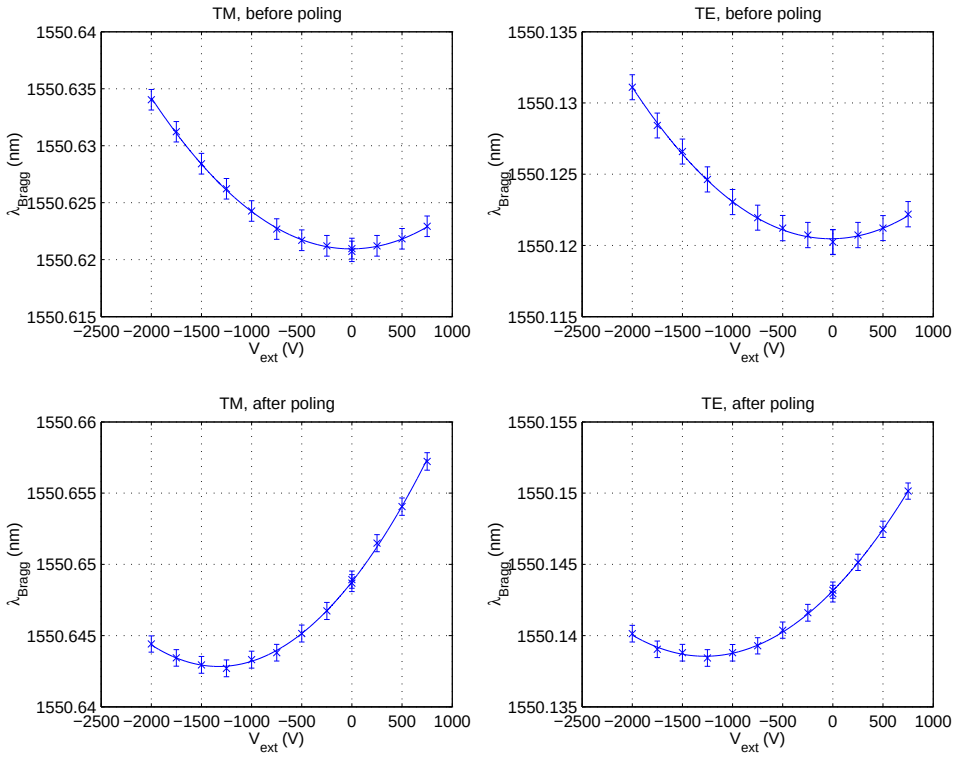

Figure 5.6: The center of the low wavelength transmission dip, λ_{Bragg}, plotted versus the externally applied DC voltage, V_{ext}. The transmission spectrum of the sample is shown in Figure 5.3. x represents the center of the Bragg grating, the vertical lines represent the uncertainties and the solid line the parabola fitted to the measurement.

the same poling parameters and both were UV written. The third-order nonlinearity measured is slightly larger than the one found for sample n4. The core content should be identical but variation in the deposition rate of the PECVD can explain the discrepancy. A possible explanation was given for the two dips observed in the transmission spectra based on an abrupt change in the refractive index of the waveguide due to out-diffusion of D_2 during waveguide writing. Finally, the asymmetry in the γ-values summarized in Table B.3 could be explained either by electric field induced stress or anisotropy of $\chi^{(3)}$.

5.4 Optimized poling parameters

In Table B.5 E_{int}, $\chi^{(2)}_{eff}$ and $\chi^{(3)}$ are found for a sample poled under the optimized parameters found by Ren *et al.* in [59]. The sample is identical to sample A2 described above, the only exception being that it has been poled using a voltage of -2.5kV at 357°C for 36 minutes. In [59] the poling temperature and poling time have been optimized for a constant poling

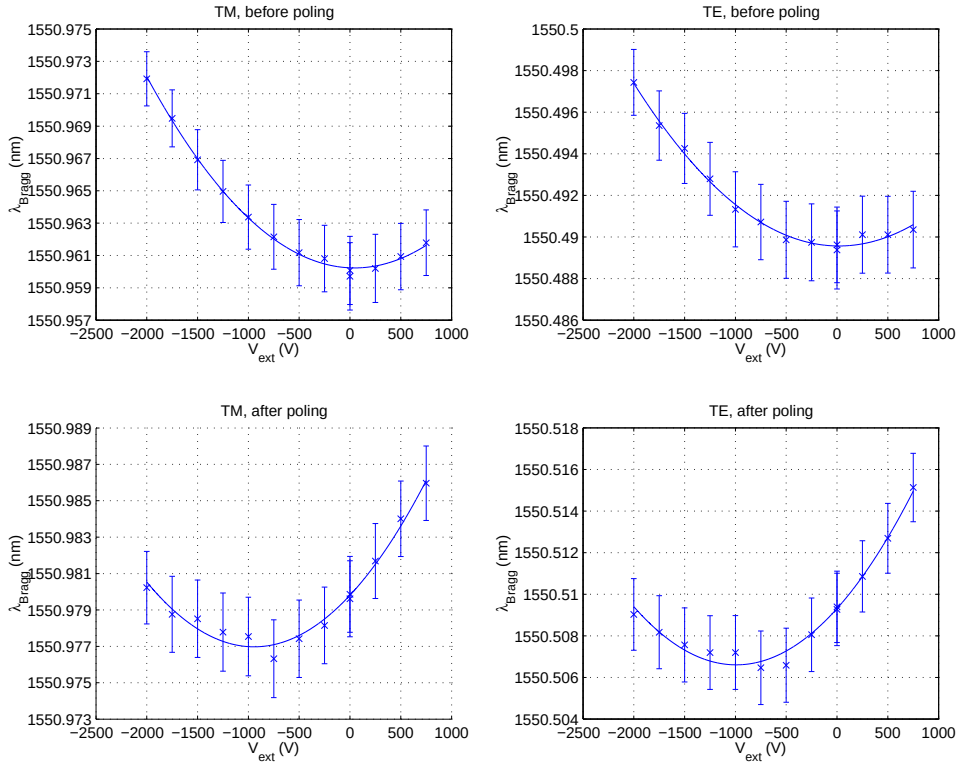

Figure 5.7: The center of the high wavelength transmission dip, λ_{Bragg}, plotted versus the externally applied DC voltage, V_{ext}. The transmission spectrum of the sample is shown in Figure 5.3. x represents the center of the Bragg grating, the vertical lines represent the uncertainties and the solid line the parabola fitted to the measurement.

voltage, namely -2.5kV. This poling voltage was chosen since it yields a very high electric field, $E_{ext} \sim 227\frac{V}{\mu m}$. The dielectric breakdown for silica, $E_{break} = 850\frac{V}{\mu m}$ [21] and going beyond $E_{ext} = -2.5kV$ as poling voltage increases the risk of breakdown considerably for this type of samples.
In Figure 5.8, two transmission spectra of the sample are shown together with the fitted functions. From Table B.5 it is seen that, within the experimental uncertainty, there is a very good coherence between the results obtained from the different transmission dips in this sample. This supports the above speculation that the transmission dips represent the same mode (the fundamental mode) and that the difference in wavelength between the two dips is due to the disappearance of the D_2 contribution to the UV induced refractive index change in the waveguides. Since the high wavelength transmission dip in Figure 5.8 is relatively stronger than the one in Figure 5.3, compared to the low wavelength transmission dips in both figures, it is assumed that the D_2 concentration at the beginning of the waveguide writing is larger in sample A8 than in A2.
The ripples superposing the two transmission dips in Figure 5.8 are prob-

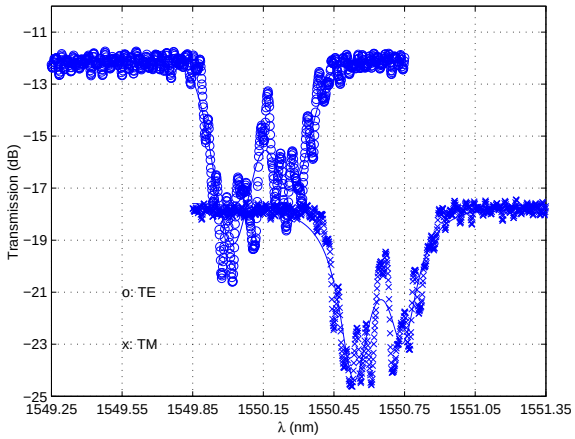

Figure 5.8: A transmission spectrum of the TM polarization, x, and TE polarization, o, of a UV written sample with low PDL together with the fitted functions, solid line.

ably due to Fabry-Perot resonances because of un-perfect cleaving of the sample. From Figure 5.8 it is seen that the wavelength separation between two adjacent ripples is

$$\Delta\lambda \sim 0.05nm \ . \tag{5.2}$$

From [61] the frequency spacing between two resonances in a planar-mirror resonator is $\Delta\nu = \frac{c}{2d}$, where c is the speed of light and d is the mirror separation. Converting the equation to wavelength yields $d = \frac{\lambda^2}{2\Delta\lambda}$. Inserting yields $d \sim 24mm$ which is the same size as the length of the sample, 35mm. For both transmission dips it is observed that $\chi^{(3)}$ is, within the uncertainty, unchanged during poling, again supporting the charge separation model. For this sample $\gamma \sim 1.10 \pm 0.02$ as seen in Table B.6. As seen in Table B.7, the measured α-values are in accordance with the values found in [20], indicating an electrostrictive contribution to $\chi^{(3)}$. Possible anisotropy of $\chi^{(3)}$ is another explanation to the measured γ-value.
In Figure 5.9, the parabolic fits to the measured parabola are shown. As in the two previous sections, a very nice coherence between the measurements and the fit is observed.
The third-order nonlinearities found for this sample are in accordance with the ones found for the low wavelength transmission dip of sample A2. Some of the discrepancy between the measured $\chi^{(3)}$ values of the two samples can be ascribed to the fact that they have been cut out from two different places of the wafer. Thickness variations of PECVD grown films are approximately 5% [80] and the measured $\chi^{(3)}$ scales as the sample thickness squared.
The field built-in during poling is very large, $E_{int} \sim 186\frac{V}{\mu m}$, approximately 50% larger than the built-in field obtained above for the sample poled using non-optimal poling parameters, indicating that the poling parameters found in [59] are optimal because a larger electric field is trapped in the sample.

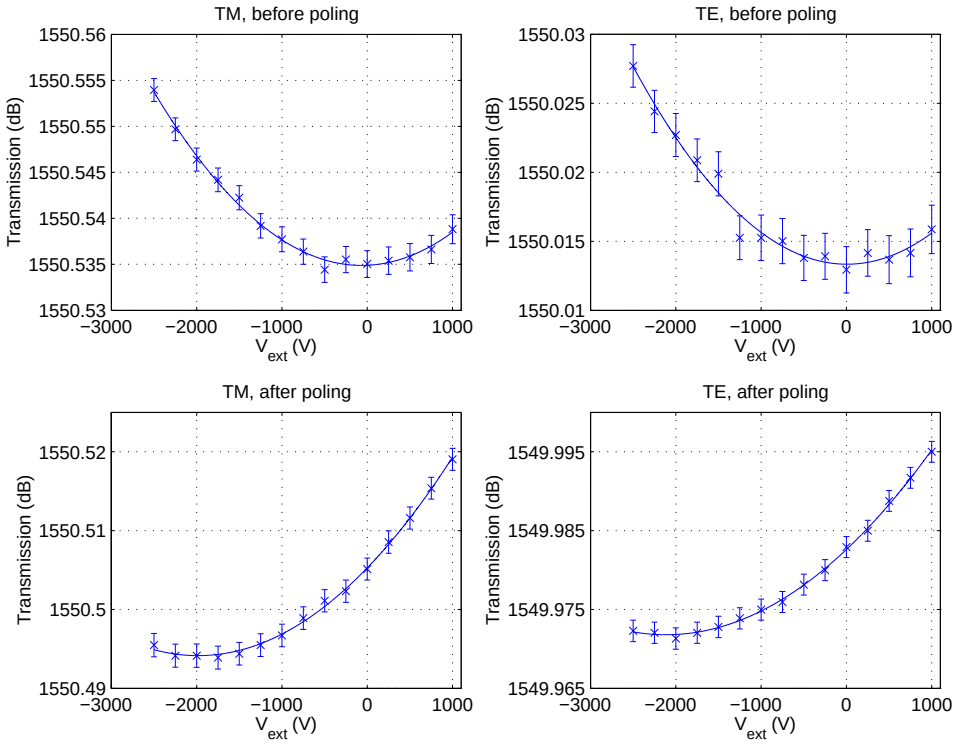

Figure 5.9: The center of the low wavelength transmission dip, λ_{Bragg}, plotted versus the externally applied DC voltage, V_{ext}. The transmission spectrum of the sample is shown in Figure 5.8. x represents the center of the Bragg grating, the vertical lines represent the uncertainties and the solid line the parabola fitted to the measurement.

Obviously, the higher poling voltage should increase the built-in field since more charges are moved towards the electrodes. Temperatures lower than the optimum poling temperature probably reduces the mobility of the ions and temperatures higher than the optimum temperature presumably empties the trapping centers located near the interfaces.
The above analysis gives a good indication of what has to be done in order to increase $\chi^{(2)}_{eff}$, namely an increase of $\chi^{(3)}$, since E_{int} is limited by E_{break}.

5.4.1 Conclusion

Again, a γ-value of approximately one is observed instead of the expected three. The third-order nonlinearities obtained for this sample were identical to the ones of the similar sample A2 described above, which indicates consistency in the measurement method. The measured second-order nonlinearities and the γ-value found using the optimized poling parameters are identical to the ones described in [59], which shows the consistency of the measurement method.

5.5 $\chi^{(2)}_{eff} = 0$ in samples with soft top-cladding

A sample with soft top-cladding as described in section 3.4.1 and Table A.8 was measured upon before and after poling. The thermal poling was performed by applying -2.0kV across the sample while heating the sample to 357°C for 20 minutes. The results of sample 4_3_2 are presented in Table B.8 and transmission spectra for the two polarizations are shown in Figure 5.10. From the table and from Figure 5.12, it is clear that no internal field is built into the sample during thermal poling. This result is confirmed by MZI measurements performed by Yitao Ren on a similar sample taken from the same wafer. No second-order nonlinearity could be measured using the MZI within the experimental error. Others have made similar observations [46]. In Figure 5.11, a possible explanation to the above mentioned results is presented. In the equivalent circuit model presented in the figure, the buffer layer has a resistivity ρ_3 much larger than the resistivities of the core layer ρ_2 and the soft top-cladding ρ_1 i.e. $\rho_3 \gg \rho_2 \gtrsim \rho_1$. In [6] the conductivities corresponding to $\frac{1}{\rho_3}$ and $\frac{1}{\rho_2}$ have been measured at temperatures above room temperatures and they show that $\rho_2 \sim 10^{-4} \cdot \rho_3$. It is likely that $\rho_1 \ll \rho_2$, as the top-cladding is doped with boron and phosphor. Assuming that $\rho_1 \ll \rho_2$, the mobile charges will be trapped in the interface between the high conduction soft top-cladding layer and the buffer layer during thermal poling. Negligible charge density will be accumulated at the core buffer interface due to the relatively higher resistivity of the core compared to the top-cladding. The frozen-in field observed by the core will thus be a fringe field with negligible influence on the light traveling in the core and thus a negligible second-order nonlinearity.

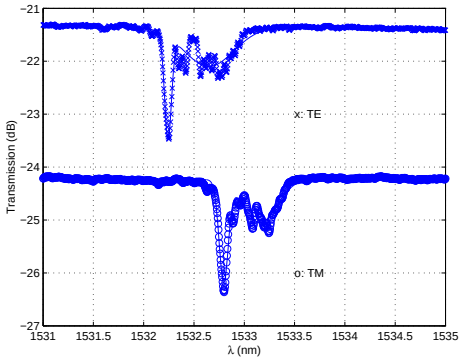

Figure 5.10: Transmission spectra of the TM, o, and TE, x, polarizations of a sample with soft top-cladding. Core and top-cladding are annealed at 800°C. The solid lines represent the fits.

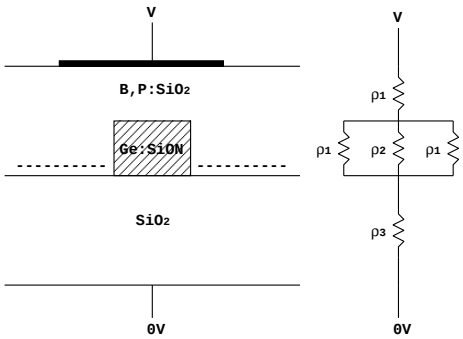

Figure 5.11: A schematic illustration of the sample described in this section together with an equivalent circuit model representing the structure.

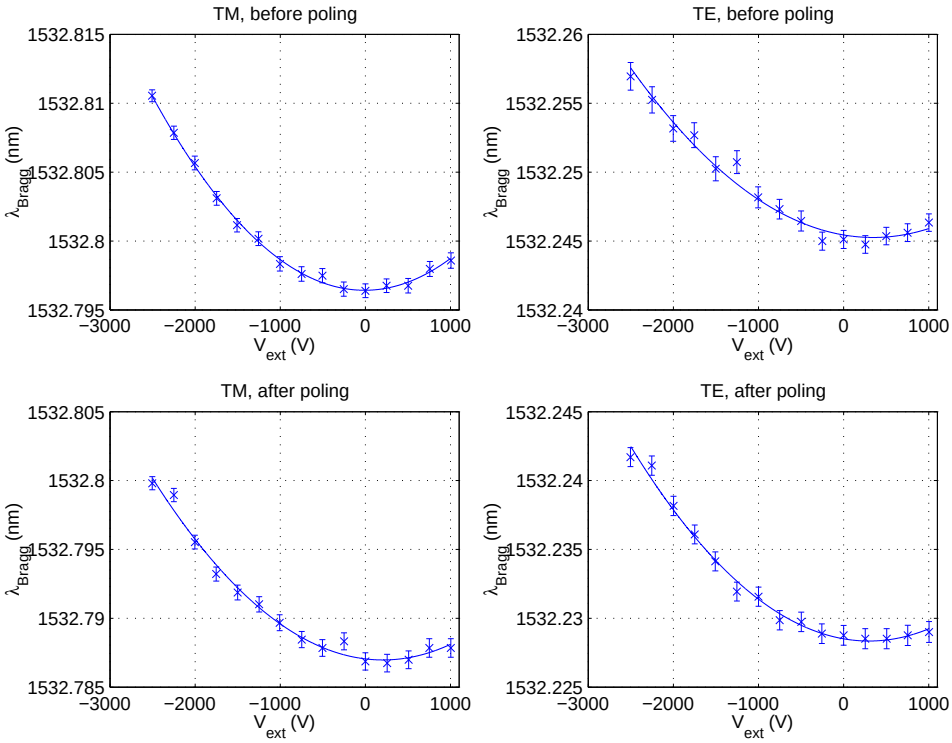

Figure 5.12: The Bragg wavelength, λ_{Bragg}, plotted versus the externally applied DC voltage, V_{ext}. The transmission spectrum of the sample is shown in Figure 5.10. x represents the measured λ_{Bragg}-values, the vertical lines represent the uncertainties and the solid line the parabola fitted to the measurement.

5.5.1 Conclusion

The main conclusion is that samples with soft top-cladding and etched core have zero second-order nonlinearity after thermal poling, probably due to very high conductivity of the boron and phosphorus doped top-cladding at elevated temperatures. Assuming that the model presented in Figure 5.11 is correct, only a fringe field is observed by light traveling in the core.

5.6 Investigation of $\chi^{(3)}$ change during poling

Different groups have published results where the third-order nonlinearity is changed during thermal poling [76] and during UV poling [8, 79, 78, 48] and after UV erasure [79, 78, 8].
As has already been mentioned above, the change in the third-order nonlinearity has been measured to be zero within the experimental error, during negative thermal poling in this thesis. [76] describes an increase of $\chi^{(3)}$ by a factor of two during positive thermal poling of twin-hole fibers. The increase in third-order nonlinearity observed during positive thermal poling

could be explained by in-diffusion of metal ions (either from the electrodes or from the salty ink injected into the holes to remove air pockets or from a combination of the two). An in-diffusion of silver ions is observed by [4] and [15] during positive thermal poling of waveguides using a silver containing top-electrode. Since [76] pole using a large positive voltage across the sample, this is a probable explanation to the change in third-order nonlinearity during poling. An in-diffused metal in a dielectric medium will strongly increase the third-order nonlinearity of the host material at the surface-plasmon resonance of the metal. A draw-back of the in-diffusion of metal ions is an increased loss. Finally, it is possible that cracks from the electrode holes into the core reduce the effective electrode distance yielding an apparently larger second- and third-order nonlinearity than is actually the case. This effect is described in section 5.7.

The effect of UV illumination on the third-order nonlinearity has also been investigated in this project. The measurements were performed in two steps on an etched waveguide with soft top-cladding, sample 17_1, described in section 3.4.2 and Table A.10 [5]. First, measurements were performed on a Bragg grating made using a fluence of $3\frac{kJ}{cm^2}$ without D_2 loading. Secondly, the sample was subjected to flood UV exposure of $10\frac{kJ}{cm^2}$, still without D_2 loading.

In Figure 5.13, the transmission spectra of the sample are shown in the two situations: Before UV flood exposure and after UV flood exposure without D_2 loading for the two polarizations. After the flood exposure, the amplitude of the Bragg grating is reduced from $\sim -2.5dB$ to $\sim -1.8dB$ and the Bragg wavelength is increased by approximately $10^{-2}nm$. This is what is expected from an UV flood exposure without D_2 loading. According to [57], the refractive index change for a non D_2 loaded sample saturates at high accumulated UV fluences. The Bragg grating writing has put our sample in the regime, where the refractive index change is very slow as a function of UV fluence and thus the Bragg wavelength change is small after the flood exposure. During the UV flood exposure, the amplitude of the fringes is reduced and with it the strength of the Bragg grating.

The parabolic fits are shown in Figure 5.14. Two parabolic fits are presented in the TE, before UV flood exposure measurement. The dashed line represents the fit when the linear term in the fit is included as a free parameter, i.e. nonzero second-order nonlinearity. One would expect a zero (within the experimental error) second-order nonlinearity, since the sample has not been poled. The solid curve represents the fit where the linear term in the parabolic fit is fixed to zero i.e. $\chi^{(2)}_{eff} \equiv 0$. The measured values of $\chi^{(2)}_{eff}$, $\chi^{(3)}$ and E_{int} for the solid curves in Figure 5.14 are shown in Table B.10. Within the experimental error it is not possible to observe any change in the third-order nonlinearity due to UV irradiation of a sample with soft

[5] This sample has been analyzed in [45].

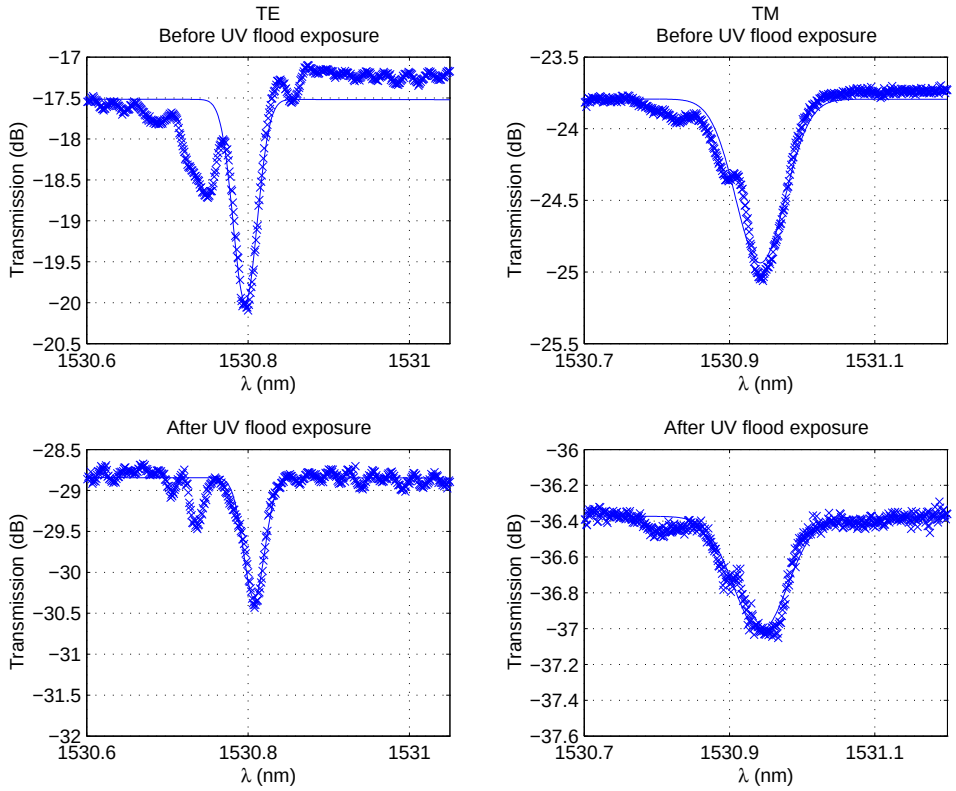

Figure 5.13: Transmission spectra of the sample subjected to different UV exposures. The left column represents TE polarization and the right TM. The first row represents the sample after a UV fluence of $3\frac{kJ}{cm^2}$ to make the Bragg grating without D_2 loading, the second row represents the sample after UV illumination with a fluence of $10\frac{kJ}{cm^2}$ and no D_2 loading.

top-cladding.

An experiment to illuminate the influence of UV fluence and D_2 was performed. The same sample was D_2 loaded and exposed to a UV fluence of $4\frac{kJ}{cm^2}$. The transmission spectra measured after this flood exposure is shown in Figure 5.16. The transmission spectra in this figure are clearly different from the spectra given in Figure 5.13. Two almost equal probable explanations exist to this fact. Either Figure 5.16 represents another waveguide than the one represented in Figure 5.13 or else the confinement factor of the low index waveguide has increased by approximately a factor of two during the D_2 sensitization and subsequent UV flood exposure. In Table B.12, the measured second- and third-order nonlinearities together with the frozen-in field are presented. In the TE measurement, the linear component of the parabolic fit has been fixed to zero since the sample has not been poled. Within the experimental error, the third-order nonlinearity is not changed after the D_2 loading and subsequent UV flooding. This is illustrated in Fig-

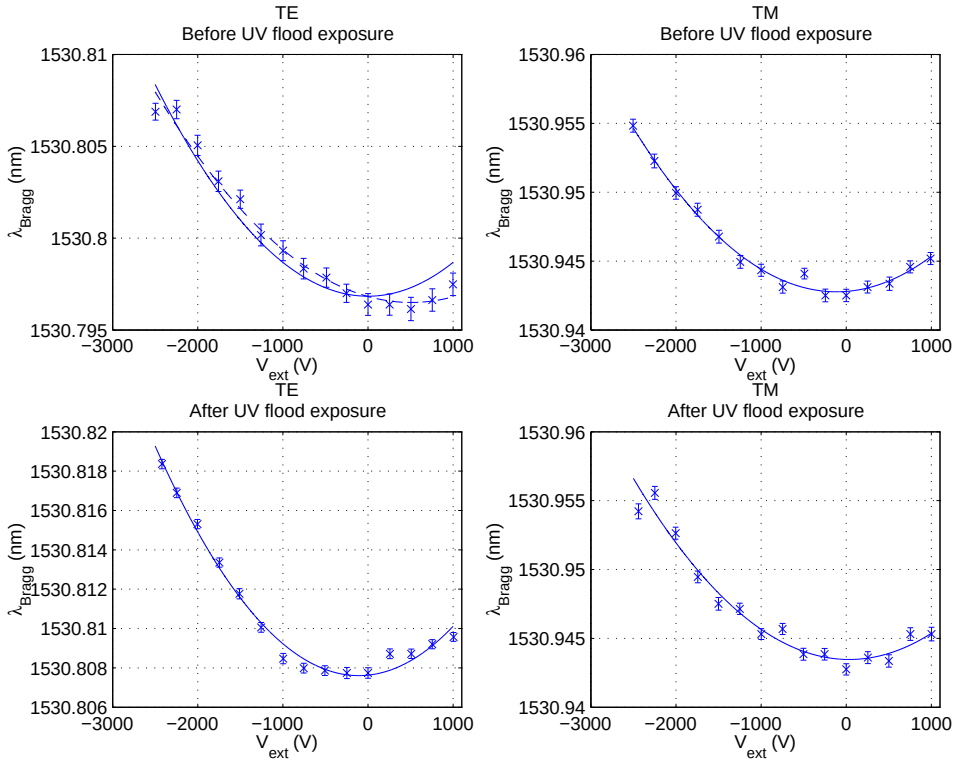

Figure 5.14: The Bragg wavelength, λ_{Bragg}, plotted versus the externally applied voltage, V_{ext}, together with the parabolic fits, solid lines. Vertical lines represent the experimental uncertainty.

ure 5.15, where the measured $\chi^{(3)}$ is plotted versus accumulated UV fluence. Within the uncertainty, only a negligible change in $\chi^{(3)}$ is observed during UV exposure [6].

If the Figures 5.13 and 5.16 do no represent the same waveguide, the comparison between the different waveguides has to be taken with some reservations. In order to be comparable, the 1) electric field induced stress and 2) dopant content in the waveguides have to be identical.

From the measurements it seems that the electric field induced stress levels in the two different waveguides are equal since the α-values found in Table B.11 and B.13 are the same within the experimental uncertainty. Different electrostrictions would have appeared in these ratios as described above in subsection 2.5.3 and in [20].

A different content of dopants in the waveguides would also change the measured third-order nonlinearity. The distribution of dopants should be uniform in the PECVD deposition of the core layer as demonstrated in [80],

[6] Most importance is put in the TM measurement, since the TE measurement has been forced to have a zero linear parabolic coefficient in the $3\frac{kJ}{cm^2}$ and $17\frac{kJ}{cm^2}$ measurements.

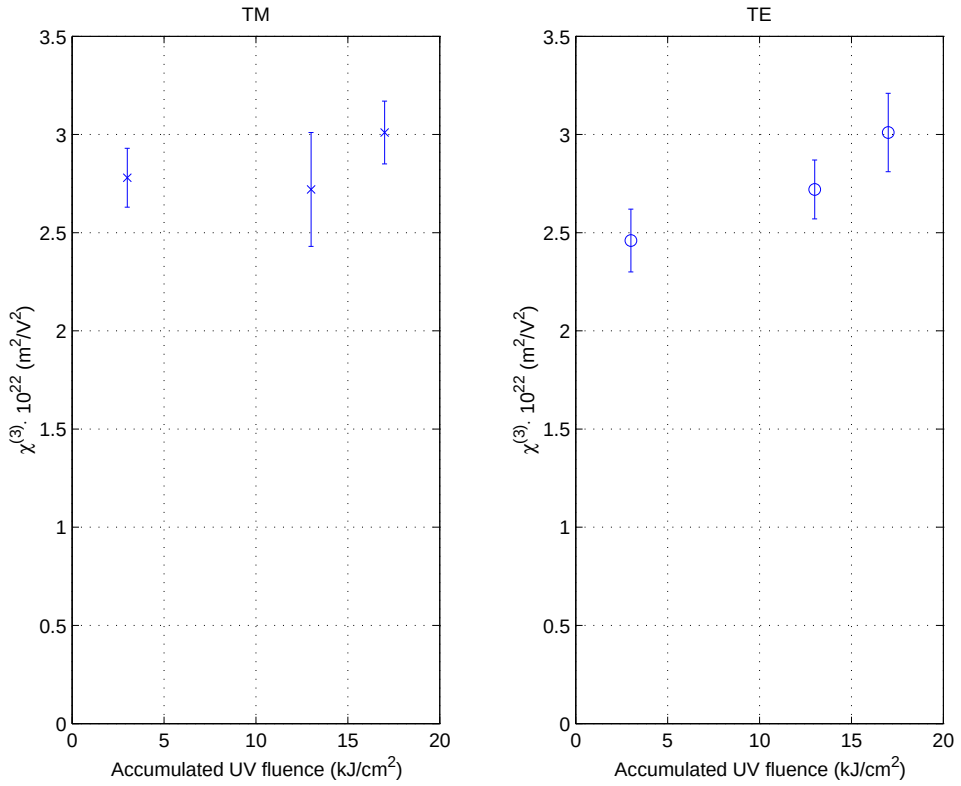

Figure 5.15: The third-order nonlinearity plotted versus accumulated UV fluence. x represent the TM and o the TE polarization. The vertical lines represent the experimental uncertainty.

where the refractive index of PECVD deposited glass only varies $\lesssim 0.02\%$ across the wafer demonstrating high uniformity in the deposited layers.

As mentioned at the beginning of this section, several groups observe a change in the third-order nonlinearity during UV poling [8, 79, 78, 48] and after UV erasure [79, 78, 8] of twin-hole fiber devices. No modification of $\chi^{(3)}$ is observed in this project. Possible explanations to this discrepancy of UV influence on $\chi^{(3)}$ are as mentioned in the discussion of the $\chi^{(3)}$ change during thermal poling, i.e. in-diffusion of metal ions during UV poling or a change in the effective electrode distance due to cracks in the cladding glass as described in section 5.7. The last point is very plausible since large holes to the electrodes are needed (between 40 to 100μm) and the measured $\chi^{(3)}$ scales as the electrode distance squared.

Stress induced during poling may also explain the UV poling $\chi^{(3)}$ change. Some of the groups [8, 79] also observe a small $\chi^{(3)}$ increase by UV erasure alone (UV applied while short circuiting the electrodes), indicating a material change due to UV irradiation. In [8, 79] a borosilicate electron trap is used to trap electrons during poling and they speculate that excited elec-

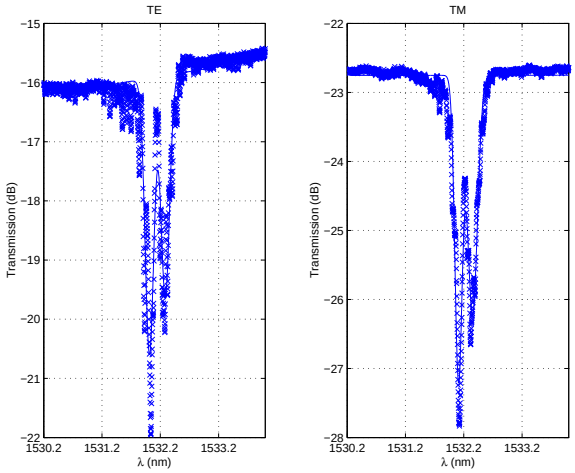

Figure 5.16: The transmission spectra of the sample after D_2 loading and a flood exposure using a UV fluence of $4\frac{kJ}{cm^2}$.

trons trapped in the boron layer are responsible for the increase of $\chi^{(3)}$. [48] suggest the creation of crystallites as the source to the increase of $\chi^{(3)}$ during UV poling.
The change of third-order nonlinearity observed by some groups could also be explained by an increase in the confinement factor. A UV induced increase of the confinement factor will increase the third-order contribution from the core. Since the third-order nonlinearity is larger for Ge doped silica than pure silica, the total third-order nonlinearity measured would increase. However, this effect would not be able to explain the increase of a factor of 2-3.5 as observed in [8, 79]. In the case of a confinement factor of 0.5 before UV treatment and the extreme case of a confinement factor of 1 after UV treatment, the increase of third-order nonlinearity would only amount to $\lesssim 33\%$.
Finally, it is of course possible that UV light applied together with a poling field could change the material yielding a change in the third-order nonlinearity during UV poling.

5.6.1 Conclusion

In this section it is shown that UV irradiation does not change the third-order nonlinearity of the samples used in this thesis. This result is similar to the result obtained in the sections above, where thermal poling is seen not to change the third-order nonlinearity. Results obtained by other groups regarding the influence of UV irradiation on $\chi^{(3)}$ are discussed and possible explanations to their results are given.

5.7 High poling effects with short lifetimes

In this section, results obtained on an etched sample having hard top-cladding as described in section 3.4.1 and Table A.7 are presented and interpretations of the results are made and applied to results obtained by other groups. In Figure 5.17, the transmission spectra of a sample having hard top-cladding, sample 3_5_1, are shown.

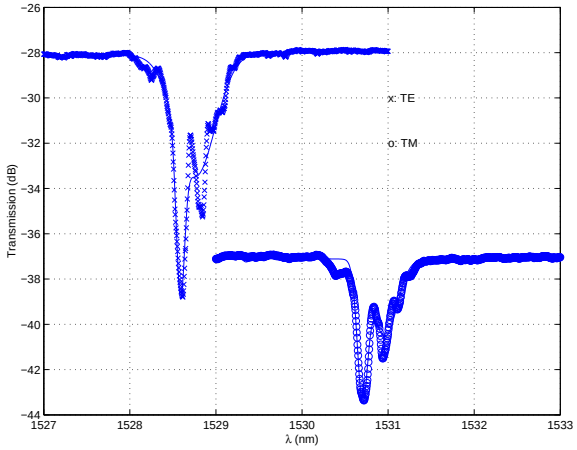

Figure 5.17: The transmission spectra of sample 3_5_1. The solid lines represent the Gaussian fits.

In Figure 5.18, a SEM picture is shown of an etched sample with hard top-cladding. From the SEM picture it is clear that cracks and voids are present in the top-cladding. In Figure 5.19, a SEM picture has been taken of a sample with soft top-cladding, actually this sample is a $6\mu m$ wide version of the sample presented in section 5.6, where a $4\mu m$ sample was used. No cracks and voids are seen in this SEM picture and the surface is nice and even. The dielectric breakdown for glass and air is 850 [21] and 3 $V/\mu m$ [10, p. 108], respectively. As the electric fields used in the Bragg grating measurement and during thermal poling are stronger than $16V/\mu m$, the air-holes/cracks will act as short circuits. Thus, the effective electrode distance in a sample with cracks is much less than the physical electrode separation.
Sample 3_5_1 is poled at temperatures as low as room temperature [7]. This is seen in Fig. 5.20, where the Bragg wavelength is measured in two different sweeps before thermal poling: Firstly, the voltage is swept from 0 to -1.5kV and secondly from -1.5kV to 0.5kV. The step-length in both curves is 0.25kV. The curves are not identical, since a field of approximately $(43.81 \pm 1.94)V/\mu m$ [8] has been built into the sample during the first sweep from 0 to -1.5kV.

[7] This sample has been analyzed in [45].
[8] Assuming no cracks i.e. that the effective electrode distance is $14.5\mu m$.

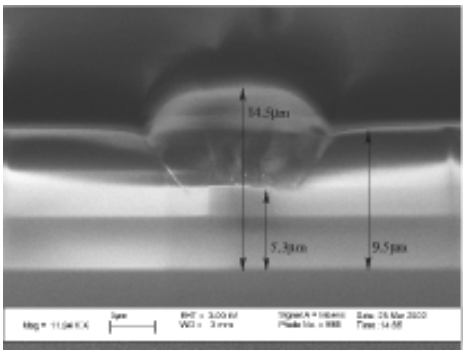

Figure 5.18: A SEM picture of sample with hard top-cladding. Cracks are clearly visible.

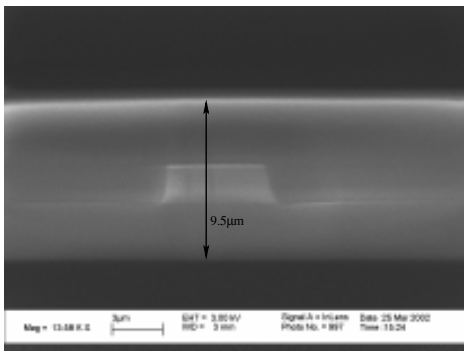

Figure 5.19: SEM picture of a $6\mu m$ wide sample with soft top-cladding. No cracks are observed.

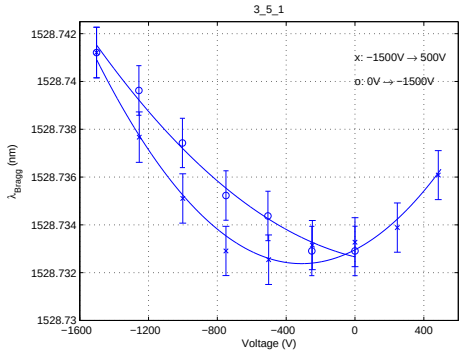

Figure 5.20: Sample 3_5_1, TE polarization, measured from 0 to -1.5kV and from -1.5 to 0.5kV using the Bragg grating as probe before thermal poling.

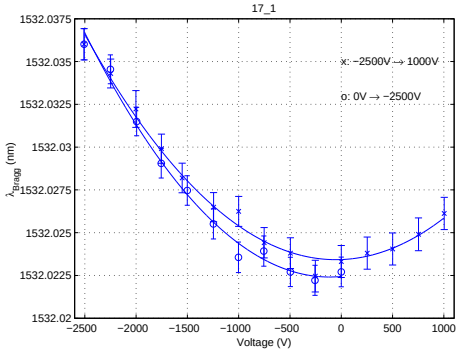

Figure 5.21: Sample 17_1, TE polarization, measured from 0 to -2.5kV and from -2.5 to 1.0kV using the Bragg grating as probe before thermal poling.

Thermal poling of the sample with cracks at $357°C$ for 20 minutes at -2.5kV yields a second-order nonlinear coefficient $\chi^{(2)}_{eff}$ between 0.04 and $0.11pm/V$ measured right after poling using the interferometric setup. One day after poling, $\chi^{(2)}_{eff}$ has decreased with between 60% and 80% of the initially induced value and one week after poling, $\chi^{(2)}_{eff}$ was measured to zero within the measurement error [9]. The built-in field is thus quasi-stable with a lifetime longer than the sweeping time used in the Bragg gratings measurements.
The instability of the poling induced internal field can also be a result of the cracks, since charges trapped at the interfaces can escape through the cracks. The lifetime of the poling at $357°C$ might very well exceed the lifetime of

[9] What is measured in the MZI is the linear electro-optic coefficient r. $r = \frac{2\chi^{(2)}_{eff}}{n^4}$ under the assumption that the overlap between the waveguide and the frozen-in field is perfect [1] and that there is no dispersion in $\chi^{(2)}_{eff}$ [52].

the room temperature poling since the charges can be trapped temporarily at the ends of the cracks.
Room temperature poling is not observed in samples without cracks as seen in Fig. 5.21. The two curves are identical within the experimental error and no internal field has been built-in during the sweep from 0 to -2.5kV.

From the SEM pictures, it is not possible to determine the length of the cracks in the sample presented in Figure 5.18 and therefore the $\chi^{(3)}$ and induced internal electric field E_{int} values are calculated for four different electrode distances as seen in Table 5.2. Three of the four distances are chosen according to distances marked on the SEM picture of sample 3_5_1 (Figure 5.18). The last distance ($7.8\mu m$) illustrates how big the effective electrode distance is, if the material constant $\chi^{(3)}$ is exactly the same for sample 3_5_1 and for sample A8 presented in section 5.4, where the core was made using the same recipe. The measurements were performed using the Bragg grating method.

	Cracks($14.5\mu m$)	Cracks($9.5\mu m$)	Cracks($7.8\mu m$)	Cracks($5.3\mu m$)
$\chi^{(3)}(10^{-22}\frac{m^2}{V^2})$	9.22 ± 0.28	3.96 ± 0.18	2.67 ± 0.08	1.23 ± 0.04
$E_{int}(\frac{V}{\mu m})$	43.81 ± 1.94	66.87 ± 2.96	81.44 ± 3.61	119.86 ± 5.31
	17_1	A8		
$\chi^{(3)}(10^{-22}\frac{m^2}{V^2})$	2.46 ± 0.16	2.64 ± 0.27		
$E_{int}(\frac{V}{\mu m})$	0 ± 0	-3.53 ± 8.31		

Table 5.2: The measured values of $\chi^{(3)}$ and E_{int} of the TE mode for sample 3_5_1 presented in Figure 5.18 poled at room temperature, for different effective electrode distances in parentheses. Sample 17_1, presented in Figure 5.19, is shown for comparison. Sample A8 has the same dopants in the core and has been annealed at the same temperatures as 3_5_1.

The lifetime of UV written samples (no cracks) has been investigated in [6] and found to be approximately 37 years at 25°C assuming second-order reaction kinetics of the space charges or aligned dipoles. As seen above, the lifetime of etched waveguides with cracks in the top-cladding is approximately a couple of days.
Several groups have published very high second-order nonlinearities induced either by thermal poling in twin-hole fibers [28], by thermal poling of D-fiber [42], by UV poling in twin-hole fibers [19] or by UV-poling of bulk silica [18]. The twin-hole fibers consist of a fiber in which two holes have been made and in which electrodes are put. The D-fiber is a commercially available fiber which has been polished down to a suitable size, placed on a Si substrate (ground electrode) surrounded by a polymer at the sides and placed under a top electrode. In [18] grooves have been made in the bulk material ($10 \cdot 10 \cdot 1 mm^3$). The decay times presented in [28, 18, 42] are found to range from 45 days to four months when fitting the decay with

a single exponential function [18] and a stretched exponential $e^{(-kt)^\beta}$ [28]. When [28] instead describes the decay using a sum of two exponential functions, two lifetimes emerge, a fast and a slow decaying component of the induced second-order nonlinearity. The lifetime of the fast decaying component is 1.6 days and 266 days for the slow component. The lifetime of the fast component is comparable to the lifetime found in this section which was due to cracks in the top-cladding, thus making it possible that the high second-order nonlinearity obtained in [28] could be due to cracks in the twin-hole fiber. Making the assumption of cracks all the way from the electrodes to the core in [28], the corrected $\chi^{(2)}_{eff}$ is reduced from 0.8 to 0.2pm/V [10] in the same order of magnitude as observed in section 5.4 and [59].
In [19] no lifetime of the poling induced second-order nonlinearity is given, but it is remarked in the article that room temperature poling is observed indicating, as mentioned above, cracks in the cladding. Again, assuming cracks all the way from the electrode to the core yields that the corrected $\chi^{(2)}_{eff}$ is reduced from $\chi^{(2)}_{TM} = 3.76pm/V$ and $\chi^{(2)}_{TE} = 12.82pm/V$ to $\chi^{(2)}_{TM} = 0.75pm/V$ and $\chi^{(2)}_{TE} = 2.56pm/V$ assuming a core diameter of $2\mu m$. Even if the assumption of cracks is correct, the induced second-order nonlinearity in [19] is still very large, indicating that silica glass is an obvious candidate for use in telecom devices such as modulators, switches etc.

5.7.1 Conclusion

Cracks in poled samples can explain the very high poling results observed by some groups. This has been investigated in this section and the main result is that cracks in the samples yield a very short-lived poling-induced second-order nonlinearity. The apparent measured values of the third-order nonlinearity is also very high before correction for the shorter electrode distance due to the cracks in the samples.

5.8 Reduction of $\chi^{(3)}$ by doping the core

Measurement on the influence of nitrogen on the third-order nonlinearity of Ge-doped SiON is investigated in this section. As already mentioned in section 5.3, it is possible to increase the third-order nonlinear effect in silica by doping with germanium [35, 56, 9].
The flow-rate of ammonia, NH_3, was varied between 0sccm and 250sccm yielding different contents of nitrogen in the sample cores and the germania, GeH_4, flow-rate was kept constant at 2sccm in all the samples. The samples are described in section 3.4.3 and in Tables A.11, A.12, A.13 and A.14. In Figure 5.22, the transmission spectra of the samples (TE polarization) are

[10] Assuming that the core is $2\mu m$x$3.5\mu m$, elongated in the direction of the electrodes.

presented together with the Gaussian fits.
In order to have approximately the same mode field in the different samples interacting with the core, the waveguide widths were calculated from $h < \frac{\lambda_0}{2\sqrt{n_{core}^2 - n_{clad}^2}}$ [69], where λ_0 is the wavelength of the light used in the waveguide, n_{core} and n_{clad} are the core and cladding refractive indices, respectively and h is the width of the waveguide in order to be single moded. Therefore, the width of the waveguide used in sample 128_1 was $8\mu m$, $6\mu m$ for sample 127_1 and $4\mu m$ for samples 126_2 and 125_1. For the low ammonia flow-rate sample (0 and 100sccm), the thickness of the buffer layer is too thin to avoid the TM polarization to probe the Si wafer and thus the TM polarization suffers extreme loss in these samples.

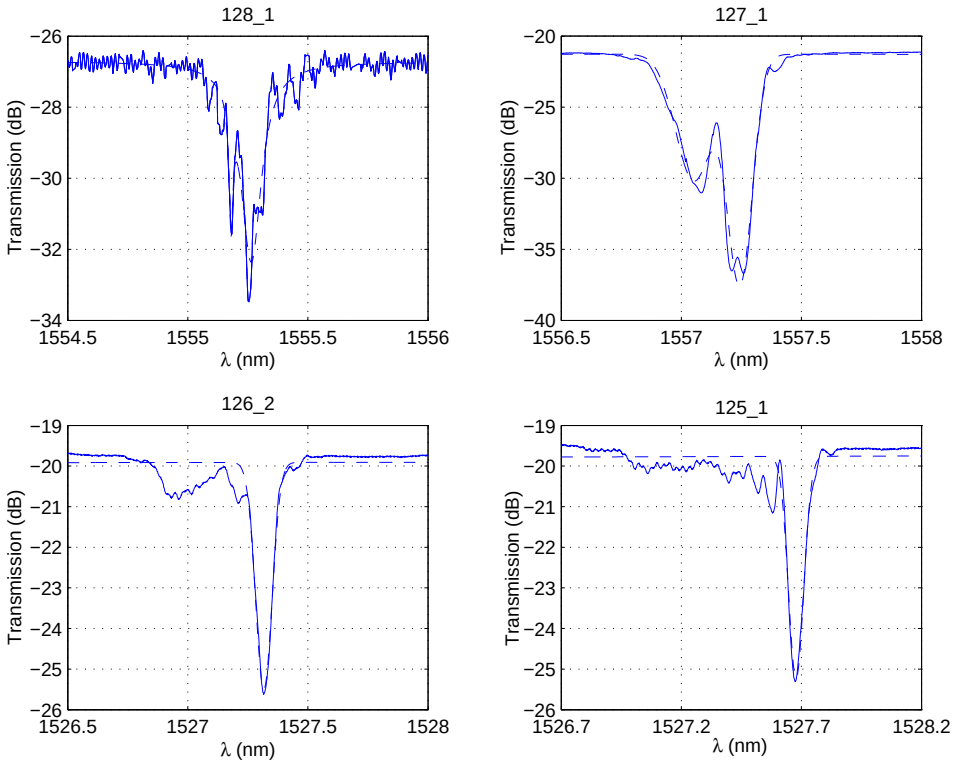

Figure 5.22: The transmission spectra of TE polarization, solid lines, of sample 128_1 (0sccm NH_3), 127_1 (100sccm NH_3), 126_2 (175sccm NH_3) and 125_1 (250sccm NH_3). All the samples had 2sccm flow-rate of GeH_4. The dashed lines represent the fitted functions.

The ripples seen in Figure 5.22, sample 128_1, are probably due to Fabry-Perot resonances from the end surfaces of the sample, as mentioned in section 5.4. Inserting $\Delta\lambda \sim 0.05nm$ into equation 5.2 yields a distance of approximately 24mm between the end facets of the sample in fair accordance with the sample size, which is 44mm.
Tables B.14, B.15, B.16 and B.18 present the measured nonlinearities and

frozen-in field found for samples 128_1, 127_1, 126_2 and 125_1, respectively. Plotting the obtained third-order nonlinearities versus the NH_3 flow-rate yields Figure 5.23.

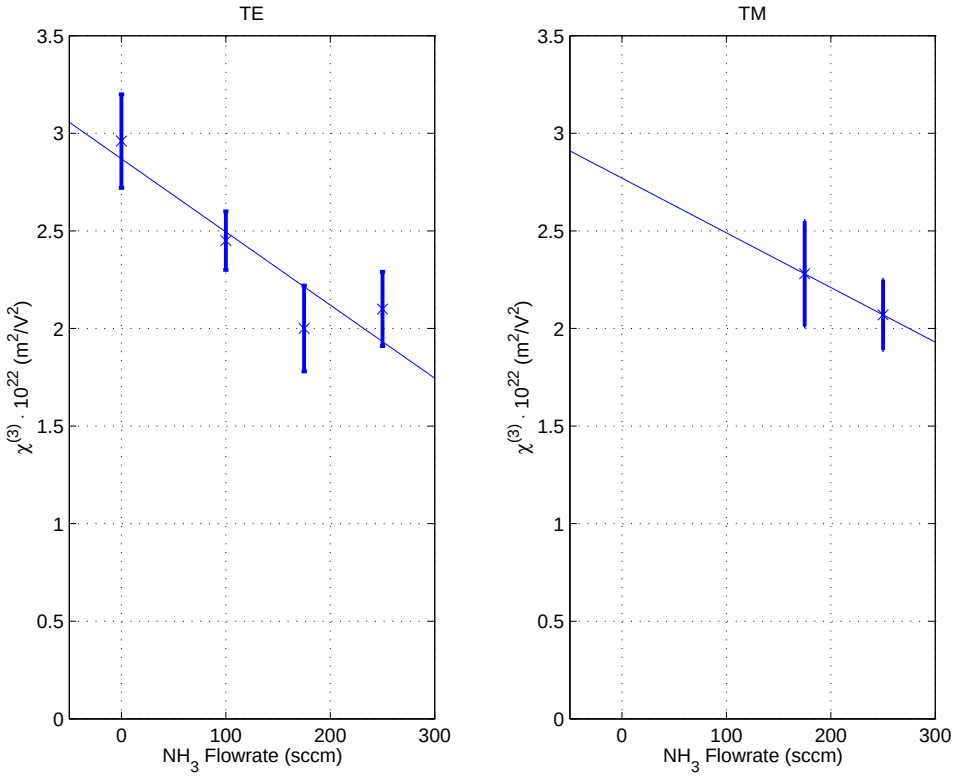

Figure 5.23: The third-order nonlinearity plotted versus the NH_3 flow-rate for the two polarizations. x denotes the measurements and the vertical line the measurement uncertainties. The solid line represents the linear fits.

The linear fits made for TE and TM polarization yields

$$\chi^{(3)} = \begin{cases} (2.83 \pm 0.18) \cdot 10^{-22} \frac{m^2}{V^2} - (3.47 \pm 1.11) \cdot 10^{-25} \frac{m^2}{V^2 \cdot sccm} \cdot x & \text{, TE} \\ 2.77 \cdot 10^{-22} \frac{m^2}{V^2} - 2.80 \cdot 10^{-25} \frac{m^2}{V^2 \cdot sccm} \cdot x & \text{, TM} \end{cases}$$

where x is the NH_3 flow-rate. In both equations, the third-order nonlinearity is reduced as the ammonia flow rate is increased, indicating that the third-order nonlinearity is a decreasing function of the amount of nitrogen incorporated into the core. This result is very important, since it yields that in order to optimize the induced second-order nonlinearity in silica glass, one should dope the waveguide heavily with germanium and refrain from using nitrogen doping of the core layer. On the other hand, this discovery also opens the door to an almost perfect linear silica material, namely silica heavily doped with nitrogen. It would be extremely interesting to measure the optical third-order nonlinearity $\chi^{(3)}(\pm\omega_1 \pm \omega_2 \pm \omega_3; \pm\omega_1, \pm\omega_2, \pm\omega_3)$ in a

nitride waveguide, but unfortunately this could not be done within the time limits of my Ph.D. project.

5.8.1 Conclusion

Other groups have investigated the influence of germanium on the third-order nonlinearity [56, 9] and found that the third-order nonlinearity is increased by Ge-doping. In this section it is found that nitrogen reduces the third-order nonlinearity in the waveguides. This result is very important, since it demonstrates that in order to obtain a large second-order nonlinearity, one should avoid using nitrogen doping and at the same time increase the germanium doping. The result can also be used in the attempt to make a perfectly linear material. Fibers made without a third-order nonlinearity would, e.g., not suffer from four-wave mixing.

5.9 Transmission spectra

In this section, the discussion about possible explanations for the form of the transmission spectra observed in this thesis is continued. As mentioned in section 5.3, the form of the transmission spectra for the UV written samples can be explained by changes in the D_2 concentration during waveguide writing. Using Differential Interference Contrast (DIC) this has been investigated. DIC measurements were made on a UV written sample, A8 (section 5.4), and on an etched sample, 17_1 (section 5.6).
The DIC microscope is described in [51, Chap. 10]. The microscope uses dual-beam interference to transform local gradients in the optical path length, OPL [11], in the object into regions of contrast in the object image as seen in Figure 5.24. This figure represents a DIC measurement on sample A8.
From the DIC image in Figure 5.24 it is possible to find the amplitude profile, $A = \frac{\partial OPL}{\partial x}$, across the sample given as the cross-sectional picture of the DIC image. Such a measurement is given in Figure 5.25. Since the amplitude A is constant outside the waveguide region of Figure 5.25 it is plausible to assume that the thickness variation of the core layer is negligible and that the waveguide region is due to a change in refractive index.
From Figure 5.25, the width of the UV written waveguide is determined as the difference between the two peaks and is found to be approximately $9.0\mu m$. As described in section 3.3.1 the width of the mask used for the UV defined waveguides with low PDL is $7\mu m$. The discrepancy between the two widths can be explained by over-exposure of the resist during the UV lithography. From both figures it is clear that a resonance structure is present inside the waveguide.

[11] OPL is the product of the refractive index and thickness between two points on an optical path.

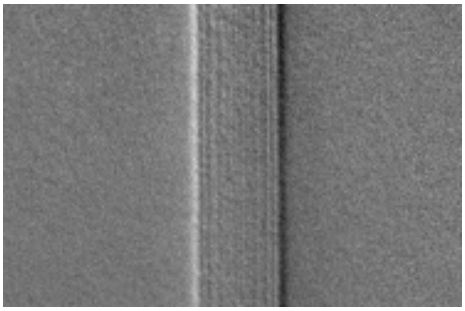

Figure 5.24: A DIC picture of sample A8. This picture shows the gradient of OPL across the sample.

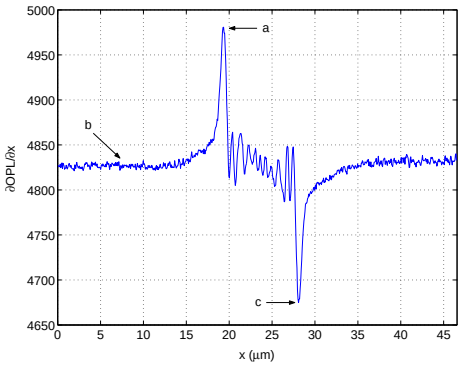

Figure 5.25: A cross-sectional picture of Figure 5.24 taken in the x-direction. x is the direction perpendicular to the waveguide in Figure 5.24.

According to [67], the peaks in the amplitude profile are proportional to the change in refractive index. Thus, by performing DIC measurements along a UV written waveguide, the explanation given in section 5.3 can be verified. In Figure 5.26 the UV induced refractive index increase is plotted versus the waveguide position. The behavior described in section 5.3, a step function in the refractive index versus position in the waveguide, is not reproduced and thus this explanation cannot be supported by the DIC measurements.

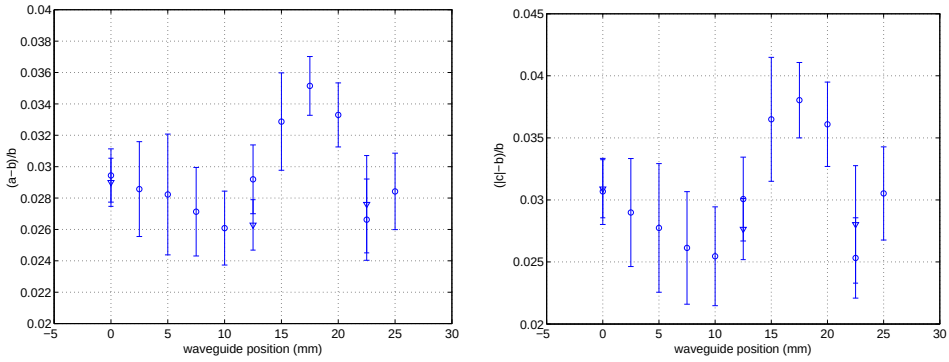

Figure 5.26: The UV induced refractive index increase measured along the waveguide. The left figure represent the left peak in Figure 5.25 and the right figure the right peak. a, b and c are defined in Figure 5.25 and are related to the UV induced refractive index increase. o and ▽ represent different measurements performed to show the consistency of the measurement method. The vertical lines represent the measurement uncertainties.

It is also possible to determine the width variation along the waveguide using the DIC measurements. The result for sample A8 is plotted in Figure 5.27. The variation of the measured waveguide width can be explained by damage to the Al mask during UV writing of the waveguides as observed by [47]. The above mentioned explanation with out-diffusion of D_2 is clearly not

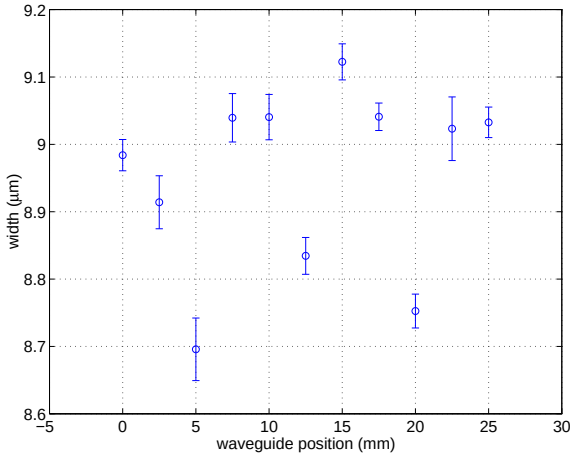

Figure 5.27: The width of a waveguide of sample A8 measured along the waveguide direction. o represent the measured values and the vertical lines the experimental uncertainties.

applicable in the case of etched waveguides where the sample has either not been D_2-loaded as is the case of samples 17_1 (Figure 5.13) and 3_5_1 (Figure 5.17) presented in sections 5.6 and 5.7, respectively, or the D_2 has out-diffused before writing of the Bragg grating as is the case of sample 4_3_2 (Figure 5.10) presented in section 5.5. The form of these transmission spectra can be explained by a variation in the average UV induced refractive index change, n_{avg} in Figure 2.3, along the waveguide. From Figure 5.26, the change in n_{avg} is seen to happen over approximately 5mm. Using a top-hat variation of n_{avg} as illustrated in Figure 5.28, the simulation using [11] yields a transmission spectrum of the Bragg grating as illustrated in Figure 5.29. The wavelength difference between the two transmission dips of sample A8 in Figure 5.8 is $\Delta\lambda_{meas} = 0.21$nm. The corresponding wavelength difference found from the simulation yields $\Delta\lambda_{calc} = 0.19$nm in very good agreement with $\Delta\lambda_{meas}$.
The variation in n_{avg} could be due to variations in the refractive index of the core layer, variations in the scan speed during waveguide writing/Bragg grating writing (but since the scan speed in both situations is constant this is not likely). Another possibility is that light reflected by the Si-wafer yields a variation in the average refractive index change in the core layer. A variation in core refractive index is exactly observed in Figure 5.26 and similar measurements performed on etched waveguides.

5.9.1 Conclusion

The transmission spectra of the uniform Bragg gratings used in this thesis have been investigated in this section. The most likely explanation to the

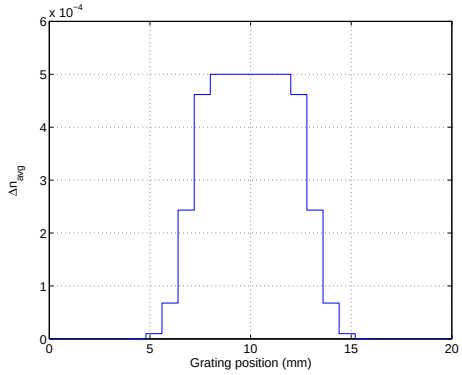

Figure 5.28: Top-hat n_{avg} variation across the Bragg grating region, FWHM∼5mm.

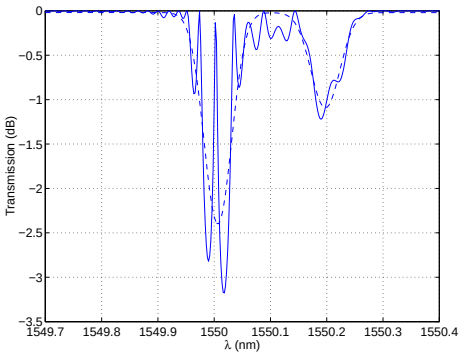

Figure 5.29: The simulated transmission spectrum for a sample with a n_{avg} as illustrated in Figure 5.28. The dashed curve represents the fitted function.

side-lobes, initially assumed as being modes, observed is probably due to variations in core layer refractive index along the waveguides. Not all samples presented in the thesis have been measured upon with the DIC method but by changing the distance over which n_{avg} varies in the simulations, the transmission spectra seen throughout this thesis e.g. samples #65 (Figure 5.31), 126_2 (Figure 5.22) and 4_3_2 (Figure 5.10) can be reproduced. It is important to note that the side-lobes have no influence on the measurements of the nonlinearities performed in this thesis. The nonlinearities and frozen-in field are consistently determined from the Bragg wavelength.

5.10 Increased E_{int} in samples with trapping layer

In this section, the results obtained on samples containing a trapping layer are presented. Time only permitted three of the four samples described in section 3.3.2 to be analyzed. The samples measured upon are #52, presented in Table A.6, #57, presented in Table A.5, and #65, presented in Table A.3. In Figure 5.30, a schematic illustration of the samples with a trapping layer analyzed in this thesis is presented.

The transmission spectra of the samples measured before poling are presented in Figure 5.31. From the figure it is noted that I did not succeed in eliminating the TM polarization from the TE measurements of sample #57. Interestingly, the transmission spectra of sample #52 look like the ones expected for a uniform sample with an abrupt termination of the index modulation amplitude, as seen in the dashed curve in Figure 5.4. Both sample #57 and sample #65 have transmission spectra which can be explained by the discussion in sections 5.3 and 5.9.

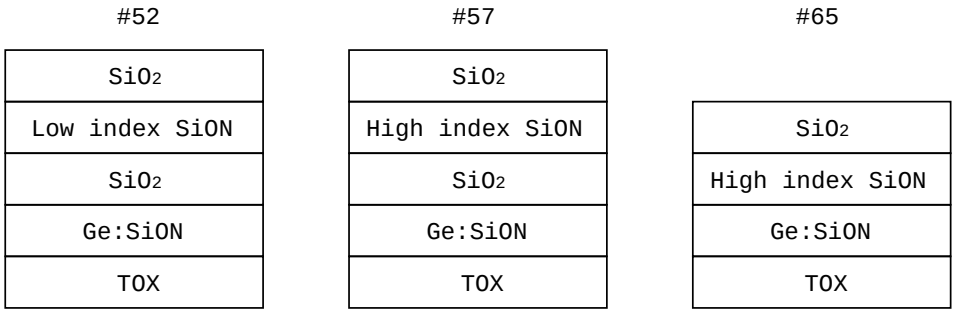

Figure 5.30: A schematic illustration of the samples with trapping layer.

5.10.1 Sample #57

Sample #57 was the first of the samples with trapping layer that was poled. Poling was first attempted at -2.8kV and 357°C but due to unfortunate electrode geometries of these samples, dielectric breakdown occurred very fast. -2.5kV also yielded dielectric breakdown. Using 357°C and -2kV the poling succeeded until the cool-down period, during which a third breakdown occurred and destroyed one of the facets. Therefore, only results before poling are presented in Tables B.21 and B.22. The values obtained are in fair accordance with the values obtained for samples A2, section 5.3, and sample A8, section 5.4. The core layers of the samples having a charge trapping layer are similar to samples A2 and A8 i.e. same dopants, doping levels, and annealing. Nevertheless it is important to note that the third-order nonlinearity for the TM polarization of sample #57 is slightly smaller (even within the experimental uncertainty) than the TM polarization values of A2 and A8. Several plausible explanations present themselves. Approximately three per cent of the mode of sample #57 is confined to the charge trapping layer. This layer is nitrogen doped. According to section 5.8, nitrogen reduces the third-order nonlinear coefficient of germanium doped SiON. If the same effect is valid for pure SiON, this could explain some of the discrepancy i.e. a reduction of $\chi^{(3)}$ by $\sim 0.007 \cdot 10^{-22} \frac{m^2}{V^2}$. If PECVD chamber conditions have changed during the deposition of the different types of samples, one would also expect a change in the core layers with a subsequent change in third-order nonlinearity. This is very probable since A2 and A8 were made a year and a half before the samples with trapping layers. A third and also very plausible explanation is a difference in electric field induced stress of the samples. The samples having a trapping layer will clearly have another electric field induced stress distribution due to the SiON layer than samples without. Looking at the α-values found in Tables B.4 and B.22, a change in electric field induced stress is evident since $\alpha_{\#57} = 0.92 \pm 0.18$ and $\alpha_{A8} = 1.09 \pm 0.03$. Unfortunately, the large uncertainty in the $\alpha_{\#57}$ measurement obscures the picture.

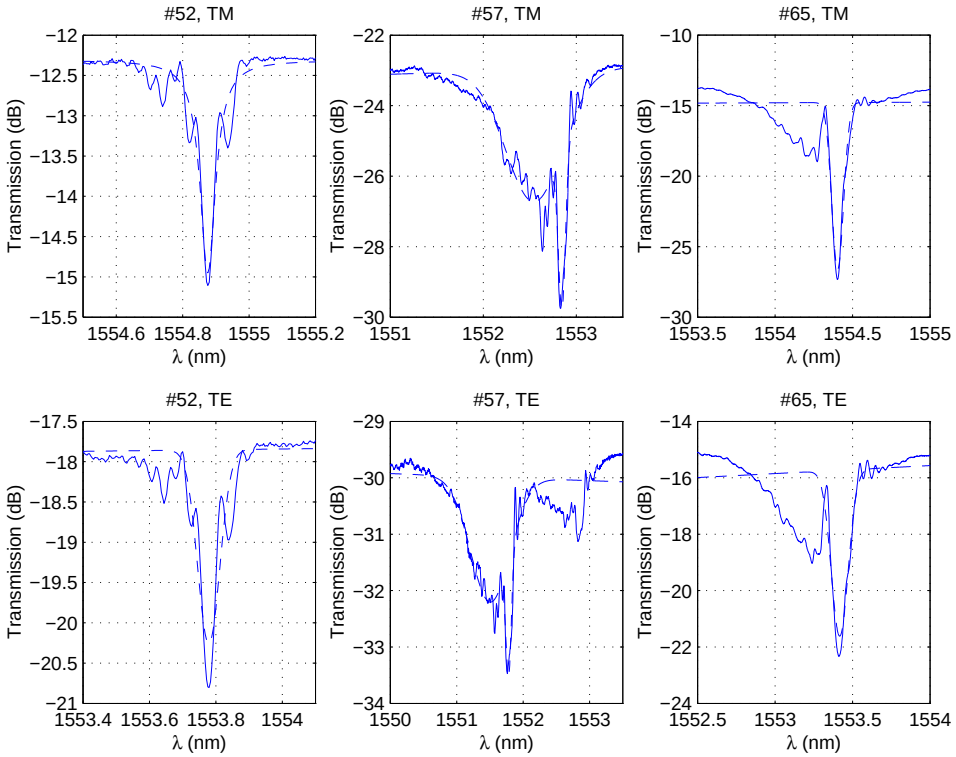

Figure 5.31: The transmission spectra measured for samples containing a trapping layer. The solid lines represent the measurements and the dashed lines the fits.

5.10.2 Sample #65

A poling temperature of 357°C and poling voltage -2kV was used to pole sample #65. In Figure 5.32, the parabolic fits are presented for the two polarizations of the sample before and after poling. Two parabolic fits are shown in the TE polarization, before poling, measurement in Figure 5.32. The solid line represents the parabolic fit, where all the points in the figure have been fitted and the dashed line represent the fit, where the -2kV and -1.75kV have been omitted. The solid line fit yields $\chi^{(3)}_{TE} = (5.82 \pm 0.65) \cdot 10^{-22} \frac{m^2}{V^2}$ which is a very high value. Three possible explanations exist for such a high third-order nonlinearity. The first is that cracks in the trapping-layer and top-cladding reduce the effective electrode distance. This explanation is very unlikely, since the same should then be observed for both polarizations and all samples with a trapping layer, which is not the case. The second possible explanation is that the third-order nonlinearity of the SiON trapping layer is extremely high. From simulations using [71] it is found that $\sim 82\%$ of the mode is in the Ge:SiON layer, $\sim 7\%$ is in the trapping layer and $\sim 11\%$ is in the top-cladding and buffer layer. Inserting these confinement factors and the values of the third-order nonlinearities of

the cladding layers and the core layer yields that $\chi^{(3)}_{trap}$ of the trapping layer has to be $\sim 39 \cdot 10^{-22} \frac{m^2}{V^2}$, ten times larger than any of the third-order nonlinearities measured in this thesis. Though not impossible [12], such a large $\chi^{(3)}_{trap}$ is not physically sensible for the samples presented in this thesis. The third possible explanation is that electrostriction could change the third-order nonlinearities. But since this is not observed for both polarization and since it is not observed for the other samples presented in this thesis, the -2kV and -1.75kV measurements were disregarded and the measurement yielded $\chi^{(3)}_{TE} = (3.49 \pm 0.59) \cdot 10^{-22} \frac{m^2}{V^2}$ as seen in Table B.23.

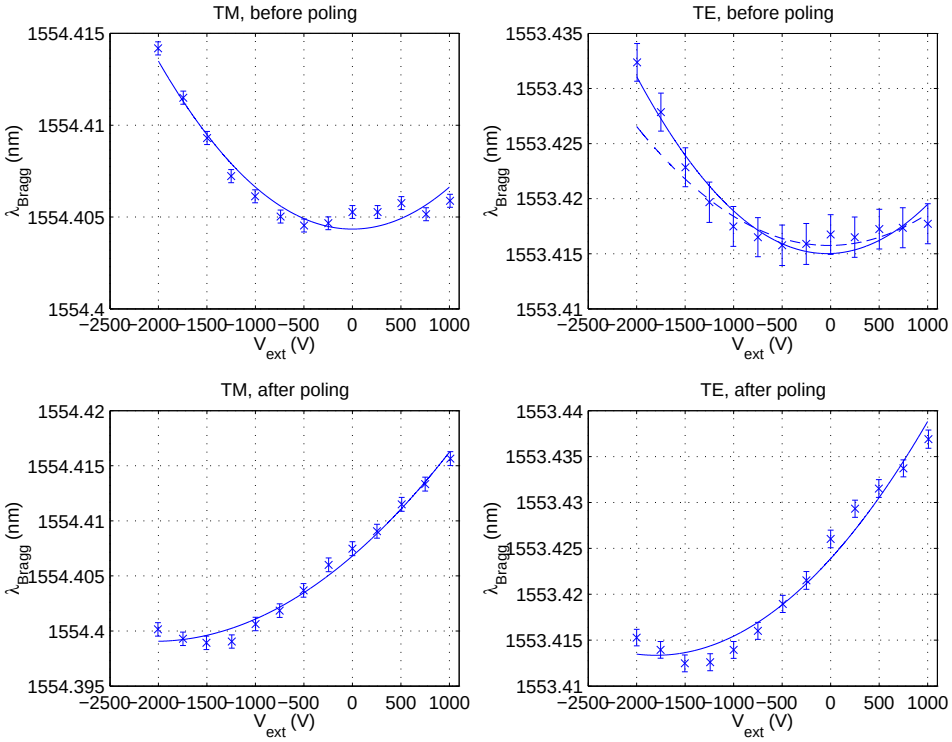

Figure 5.32: The Bragg wavelength, λ_{Bragg}, plotted versus the externally applied voltage, V_{ext}, together with the parabolic fits of sample #65. Vertical lines represent the experimental uncertainty.

From the figure, it is evident that a frozen-in field is present after thermal poling. The measured values of the frozen-in field, the second- and third-order nonlinearities are presented in Table B.23. The third-order nonlinearity is, within the rather large uncertainty, comparable to the values found for samples A2, A8 and #57 with similar type core layer. The value found for the TE polarization, after poling, has only to be given limited importance due to the rather high value and enormous experimental uncer-

[12] [48] observes $\chi^{(3)}(2\omega;\omega,\omega) \sim 10^{-19} \frac{m^2}{V^2}$ after UV poling.

tainty. The frozen-in field of sample #65 is 39% (TM) and 28% (TE) larger than the values found for sample A2, poled using the same voltage, -2kV, and almost the same temperature. Apart from the charge trapping layer, the samples are similar and thus the increase in frozen-in field is ascribed to the charge trapping layer.
The γ-value presented in Table B.24 is rather low compared to similar samples (A2 and A8). This is probably due to the rather high $\chi^{(3)}_{TE}$-value described above which is also expressed in the low α-value measured after poling in Table B.25. The before poling α-value is comparable to the value found for sample #57 in Table B.22.
MZI measurements performed by [60] on samples with trapping layers also yield an increased second-order nonlinearity for samples of the same type as #65 indicating consistency in the measurements and that this type of sample has an increased trapping efficiency. [60] poled the samples at -2.8kV, 357°C for 20 minutes. Assuming perfect overlap between the frozen-in field and the waveguides yields $\chi^{(2)}_{eff,TM} = 0.225\frac{pm}{V}$ and $\chi^{(2)}_{eff,TE} = 0.199\frac{pm}{V}$ from the measurements in [60]. If a linear relation exists between $\chi^{(2)}_{eff}$ and the poling voltage, this corresponds to $\chi^{(2)}_{eff,TM} = 0.161\frac{pm}{V}$ and $\chi^{(2)}_{eff,TE} = 0.142\frac{pm}{V}$ if [60] had used -2kV as poling voltage. The accordance with the results presented in Table B.23 is fair.

5.10.3 Sample #52

Sample #52 was poled at -2kV, 412°C for 20 minutes. Unfortunately, I was only able to measure the TM polarization of this sample. The TE polarization measurement was destroyed by bad in-coupling from the fibers to the waveguide. The results are presented in Table B.20. As above, a frozen-in field is built-in during poling. The field is smaller than the one observed for samples n4, A2 and #65 with a similar core layer poled under the same conditions as seen in Figure 5.33. It is difficult to explain how the incorporation of a trapping layer should reduce the built-in field with approximately 25% compared to a sample without trapping layer. The only possible explanation is that the polarity of the low index trapping layer in sample #52 has been inverted. This could happen if the charge carriers in the low index SiON layer have opposite charge of the ones in Ge:SiON and in the high index SiON layer as in #65. A similar sample has been investigated by [60] who finds $\chi^{(2)}_{eff,TM} = 115.0 \cdot 10^{-3}\frac{pm}{V}$ when the result has been corrected for the higher poling voltage used in [60]. This result is in better accordance with what would be expected for a sample without a trapping layer.
The third-order nonlinearity is comparable to the one observed for samples #65 and #57 as expected.

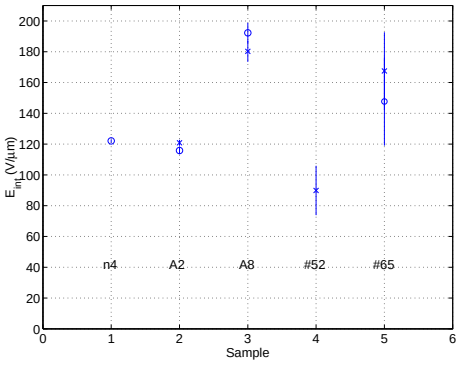

Figure 5.33: The frozen-in fields of samples n4, A2, A8, #52 and #65. x and o denote TM and TE polarization, respectively. The vertical lines represent the experimental uncertainties.

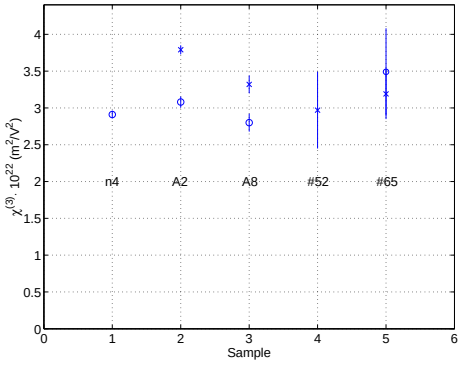

Figure 5.34: The measured third-order nonlinearity of samples n4, A2, A8, #52 and #65. x and o denote TM and TE polarization, respectively. The vertical lines represent the experimental uncertainties.

5.10.4 Conclusion

From the measurements on the samples with charge trapping layers it has become evident that a high index trapping layer deposited directly on-top of the core increases the frozen-in electric field. From Figure 5.34 it is seen that the third-order nonlinearity of the samples with the same type of core material is identical within the experimental error. Thus, the increase in the measured second-order nonlinearity is solely due to an increase in the frozen-in field caused by the trapping layer.
Inserting a low index trapping-layer on top of a pure silica buffer layer does not increase (or decrease) the frozen-in field. The reason probably being that the nitrogen doping is too small to make an effect in the trapping efficiency of the trapping layer.

Chapter 6

Conclusion

This thesis reflects my work on switchable Bragg gratings performed during my Ph.D. study. The study was performed at COM at the Technical University of Denmark and funded by ADC Denmark Aps. (in the first half of the study) and the Danish Academy of Technical Sciences (ATV). Unfortunately, ADC Denmark Aps. closed 30 November 2001 due to the recession in the telecom sector. My project was continued under NKT Research A/S together with ATV from the 1^{st} of December 2001 and until the handing in of the thesis.
The goal of the project was to make a switchable Bragg grating in germanium doped silicon-oxy-nitride waveguides. The samples were made in the cleanroom at MIC and at COM. In order to switch the Bragg gratings, they were thermally poled in order to induce a second-order nonlinear effect in the region with the Bragg gratings.

Using Bragg gratings to determine the nonlinearities of a material is a good and reliable method. Only two serious problems of the method exist. The first is that the temperature has to be kept constant and the second is that the in- and out-coupling from the fibers to the waveguides has to be very good in order to ensure that observed changes in the Bragg wavelength are due to electro-optic effects.
During my project, our research group has succeeded in increasing the induced second-order nonlinearity of the waveguides from $\sim 0.14\frac{pm}{V}$ to $\sim 0.23\frac{pm}{V}$ i.e. a 64% increase. This was done by optimizing the poling parameters and introducing a high refractive index SiON trapping layer. Even though the achieved second-order nonlinearity is not sufficient to switch a Bragg grating to make it useful in telecommunication, it is enough to make an optical switch. Using an MZI for the switch, the voltage needed for switching would be approximately $\pm$300V which is easily achievable with today's electronics.
The measurements performed in this thesis showed that the optimized pol-

ing parameters and the trapping layers increased the frozen-in field interacting with the third-order nonlinearity of the material to yield the effective second-order nonlinearity. Since the frozen-in field is limited by the dielectric breakdown of silica, another method to increase the second-order nonlinearity would be to increase the third-order nonlinearity.
Measuring the third-order nonlinearity before and after thermal poling did not indicate a change in the third-order nonlinearity. Several measurements were made to investigate if it was possible to change the third-order nonlinearity by flood UV exposure of the samples. Again, the third-order nonlinearity remained constant prior to and after UV flood exposure. Other groups [76, 8, 79, 78, 48] had seen a change in third-order nonlinearity during poling. Possible explanations to their results were among others in-diffusion of metal ions into the waveguide or cracks in the cladding.
It is a well-known fact that the optical third-order nonlinearity is increased as the germanium content of the core is increased [9, 56]. In this project it was shown that increasing nitrogen content in germanium doped silica decreases the third-order nonlinearity. This opens the possibility for making a true linear glass and also indicates that nitrogen is to be avoided in order to increase the second-order nonlinearity.
During the investigation of etched waveguides, two interesting facts became clear. Firstly, it was discovered that etched samples with soft top-cladding did not posses a second-order nonlinearity due to the high conductivity of the boron and phosphorus doped top-cladding at poling temperatures. Secondly, it was found that etched samples with hard top-cladding had very high third-order nonlinearities, could be poled at room temperature and the lifetime of the thermal poling induced second-order nonlinearities was very short. The explanation of these phenomena was cracks in the top-cladding acting as short-circuits reducing the effective electrode distance. This effect could explain the high, short-lived second-order nonlinearities observed by some groups [28, 42, 19, 18].

6.0.5 Outlook

To further increase the induced second-order nonlinearity in the waveguides, it is necessary to increase the frozen-in field and/or the third-order nonlinearity.
A further increase in the frozen-in field can be achieved by inserting a trapping layer, e.g. a boron doped silica layer, below the core layer and/or by changing the composition of the existing trapping layer.
Regarding the third-order nonlinearity, it has become evident from this thesis, that the most probable method of changing $\chi^{(3)}$ is by doping the core with different elements. Since only a limited number of elements are available in the PECVD machine, plans have been made to incorporate different types of elements by ion-implantation.

Finally, a new MZI setup consisting of an AC and a DC generator has been made by R. Shim Jacobsen which is able to measure the second- and third-order nonlinearities of non-UV-sensitive materials, which are not easily characterized by the Bragg grating method. This new setup also allows confirmation of the results obtained by the Bragg grating method.

Appendix A

n and t of the samples

In this appendix, the tables containing the refractive indices and thicknesses of the different samples are given. All measurements are performed in a prism coupler using $\lambda = 632.8\,\text{nm}$. All films are measured after annealing.

A.1 Sample with thin buffer layer

	Glass type	Refractive index	Thickness (μm)
Top-cladding	SiO_2	1.458	3.2
Core	Ge:SiON	1.493	2.4
Buffer layer	SiO_2	1.458	3.2

Table A.1: The refractive index and thickness of the different layers in a UV-written sample with thin buffer layer. The sample was made by [6]. The buffer layer was deposited using PECVD.

A.2 UV written samples with low PDL

	Glass type	Refractive index	Thickness (μm)
Top-cladding	SiO_2	1.463	4.6
Core	Ge:SiON	1.493	2.2
Buffer layer	TOX	1.458	4.2

Table A.2: The refractive index and thickness of the different layers in a UV-written sample with low PDL.

A.3 UV written samples with a trapping layer

	Glass type	Refractive index	Thickness (μm)
Top-cladding	SiO_2	1.462	3.8
Trapping layer	SiON	1.500	0.3
Core	Ge:SiON	1.504	3.3
Buffer layer	TOX	1.458	4.8

Table A.3: The refractive index and thickness for the different layers in a UV written sample with a high index trapping layer directly on the core layer.

	Glass type	Refractive index	Thickness (μm)
Top-cladding	SiO_2	1.462	3.8
Trapping layer	SiON	1.455	0.3
Core	Ge:SiON	1.504	3.3
Buffer layer	TOX	1.458	4.8

Table A.4: The refractive index and thickness for the different layers in a UV written sample with a low index trapping layer directly on the core layer.

	Glass type	Refractive index	Thickness (μm)
Top-cladding	SiO_2	1.462	3.8
Trapping layer	SiON	1.500	0.3
Buffer layer	SiO_2	1.462	0.6
Core	Ge:SiON	1.504	3.3
Buffer layer	TOX	1.458	4.8

Table A.5: The refractive index and thickness of the different layers in a UV written sample with a buffer layer between a high index trapping layer and the core layer.

	Glass type	Refractive index	Thickness (μm)
Top-cladding	SiO_2	1.462	3.8
Trapping layer	SiON	1.455	0.3
Buffer layer	SiO_2	1.462	0.6
Core	Ge:SiON	1.504	3.3
Buffer layer	TOX	1.458	4.8

Table A.6: The refractive index and thickness of the different layers in a UV written sample with a buffer layer between a low index trapping layer and the core layer.

A.4 Etched samples batch 1

	Glass type	Refractive index	Thickness (μm)
Top-cladding	SiO_2	1.463	7.6
Core	Ge:SiON	1.504	2.9
Buffer layer	TOX	1.458	4.2

Table A.7: The refractive index and thickness of the different layers in an etched sample with hard top-cladding.

	Glass type	Refractive index	Thickness (μm)
Top-cladding	$B, P : SiO_2$	1.459	6.2
Buffer layer	SiO_2	1.463	0.9
Core	Ge:SiON	1.504	2.9
Buffer layer	TOX	1.458	4.2

Table A.8: The refractive index and thickness of the different layers in an etched sample with soft top-cladding.

A.5 Etched samples batch 2

	Glass type	Refractive index	Thickness (μm)
Top-cladding	$B, P : SiO_2$	1.458	8.3
Buffer layer	SiO_2	1.466	0.4
Core	Ge:SiON	1.484	2.9
Buffer layer	TOX	1.458	4.0

Table A.9: The refractive index and thickness of the different layers in an etched sample annealed wet at 1100°C.

	Glass type	Refractive index	Thickness (μm)
Top-cladding	$B, P : SiO_2$	1.458	8.3
Buffer layer	SiO_2	1.466	0.4
Core	Ge:SiON	1.458*	3.16
Buffer layer	TOX	1.458	4.0

Table A.10: The refractive index and thickness of the different layers in an etched sample annealed in N_2 at 1000°C. * The fact that this waveguide guides light can only be explained by a densification of the core layer during the wet anneal of the soft top-cladding.

A.6 Etched samples batch 3

	Glass type	Refractive index	Thickness (μm)
Top-cladding	$B,P:SiO_2$	1.458	8.0
Buffer layer	SiO_2	1.466	0.4
Core	$Ge:SiO_2$	1.433*	2.8
Buffer layer	TOX	1.458	4.8

Table A.11: The refractive index and thickness of the different layers in an etched sample with 0sccm flowrate NH_3 and annealed dry at $1000°C$. * The fact that this waveguide guides light can only be explained by a densification of the core layer during the wet anneal of the soft top-cladding.

	Glass type	Refractive index	Thickness (μm)
Top-cladding	$B,P:SiO_2$	1.458	8.0
Buffer layer	SiO_2	1.466	0.4
Core	Ge:SiON	1.474	3.3
Buffer layer	TOX	1.458	4.8

Table A.12: The refractive index and thickness of the different layers in an etched sample with 100sccm flowrate NH_3 and annealed dry at $1000°C$.

	Glass type	Refractive index	Thickness (μm)
Top-cladding	$B,P:SiO_2$	1.458	8.0
Buffer layer	SiO_2	1.466	0.4
Core	Ge:SiON	1.504	3.1
Buffer layer	TOX	1.458	4.8

Table A.13: The refractive index and thickness of the different layers in an etched sample with 175sccm flowrate NH_3 and annealed dry at $1000°C$.

	Glass type	Refractive index	Thickness (μm)
Top-cladding	$B, P : SiO_2$	1.458	8.0
Buffer layer	SiO_2	1.466	0.4
Core	Ge:SiON	1.535	2.9
Buffer layer	TOX	1.458	4.8

Table A.14: The refractive index and thickness of the different layers in an etched sample with 250sccm flowrate NH_3 and annealed dry at $1000°C$.

Appendix B

E_{int}, $\chi^{(2)}_{eff}$ and $\chi^{(3)}$ of the samples

In this appendix, the frozen-in field E_{int}, the induced second-order nonlinearity $\chi^{(2)}_{eff}$ and the third-order nonlinearity $\chi^{(3)}$ of the different samples are presented in tables together with the measured γ-values.

B.1 UV written sample with thin buffer layer

	Before poling	After poling
E_{int} $\left(\frac{V}{\mu m}\right)$	5.64 ± 1.55	122.09 ± 1.02
$\chi^{(3)}$ $\left(10^{-22}\frac{m^2}{V^2}\right)$	2.91 ± 0.05	2.80 ± 0.02
$\chi^{(2)}_{eff}$ $\left(10^{-3}\frac{pm}{V}\right)$	4.92 ± 1.35	102.55 ± 0.44

Table B.1: E_{int}, $\chi^{(2)}_{eff}$ and $\chi^{(3)}$ for sample n4. The sample was D_2 loaded before writing of the waveguides, where the UV fluence was $2\frac{kJ}{cm^2}$. After D_2 outdiffusion a Bragg grating was made using $1.2\frac{kJ}{cm^2}$. The sample was poled at -2kV, 375°C for 16 minutes.

B.2 UV written sample with low PDL

	Before poling		After poling	
	TM	TE	TM	TE
	Low wavelength transmission dip			
$E_{int}\ \left(\frac{V}{\mu m}\right)$	0.84 ± 1.03	1.94 ± 1.59	120.85 ± 1.90	115.85 ± 2.32
$\chi^{(3)}\ \left(10^{-22}\frac{m^2}{V^2}\right)$	3.79 ± 0.06	3.08 ± 0.07	3.82 ± 0.05	3.21 ± 0.06
$\chi^{(2)}_{eff}\ \left(10^{-3}\frac{pm}{V}\right)$	0.96 ± 1.18	1.79 ± 1.47	138.40 ± 1.07	111.43 ± 1.11
	High wavelength transmission dip			
$E_{int}\ \left(\frac{V}{\mu m}\right)$	-4.31 ± 2.38	-1.85 ± 3.56	86.56 ± 6.37	91.18 ± 6.83
$\chi^{(3)}\ \left(10^{-22}\frac{m^2}{V^2}\right)$	3.19 ± 0.11	2.17 ± 0.11	3.52 ± 0.20	3.09 ± 0.19
$\chi^{(2)}_{eff}\ \left(10^{-3}\frac{pm}{V}\right)$	-4.13 ± 2.27	1.21 ± 2.32	91.37 ± 4.14	84.52 ± 3.74

Table B.2: E_{int}, $\chi^{(2)}_{eff}$ and $\chi^{(3)}$ for sample A2. The sample was D_2 loaded before writing of the waveguides, where the UV fluence was $3\frac{kJ}{cm^2}$. After D_2 outdiffusion a Bragg grating was made using $1\frac{kJ}{cm^2}$. The sample was poled at -2kV, 375°C for 16 minutes.

High wavelength transmission dip	Low wavelength transmission dip
1.08 ± 0.07	1.24 ± 0.02

Table B.3: The measured γ-values after of sample A2.

	Before poling	After poling
Low λ_{Bragg} dip	1.23 ± 0.03	1.19 ± 0.03
High λ_{Bragg} dip	1.47 ± 0.09	1.14 ± 0.10

Table B.4: The measured α-values of sample A2.

B.3 Sample poled using optimal poling-parameters

	Before poling		After poling	
	TM	TE	TM	TE
	Low wavelength transmission dip			
$E_{int}\ \left(\frac{V}{\mu m}\right)$	5.96 ± 3.32	-0.50 ± 6.99	180.24 ± 6.75	192.28 ± 6.46
$\chi^{(3)}\ \left(10^{-22}\frac{m^2}{V^2}\right)$	3.61 ± 0.14	2.59 ± 0.22	3.21 ± 0.11	2.74 ± 0.08
$\chi^{(2)}_{eff}\ \left(10^{-3}\frac{pm}{V}\right)$	6.45 ± 3.59	0.39 ± 5.42	173.53 ± 2.63	157.93 ± 2.04
	High wavelength transmission dip			
$E_{int}\ \left(\frac{V}{\mu m}\right)$	9.80 ± 4.35	-3.53 ± 8.31	175.83 ± 6.95	190.79 ± 8.87
$\chi^{(3)}\ \left(10^{-22}\frac{m^2}{V^2}\right)$	3.66 ± 0.18	2.64 ± 0.27	3.32 ± 0.12	2.80 ± 0.12
$\chi^{(2)}_{eff}\ \left(10^{-3}\frac{pm}{V}\right)$	10.77 ± 4.74	-2.80 ± 6.58	175.12 ± 2.91	160.38 ± 2.89

Table B.5: E_{int}, $\chi^{(2)}_{eff}$ and $\chi^{(3)}$ for sample A8. The sample was D_2 loaded before writing of the waveguides, where the UV fluence was $3\frac{kJ}{cm^2}$. After D_2 outdiffusion a Bragg grating was made using $1\frac{kJ}{cm^2}$. The sample was poled at -2.5kV, 357°C for 36 minutes.

High wavelength transmission dip	Low wavelength transmission dip
1.09 ± 0.03	1.10 ± 0.02

Table B.6: The measured γ-values after poling for sample A8.

	Before poling	After poling
Low λ_{Bragg} dip	1.39 ± 0.13	1.17 ± 0.05
High λ_{Bragg} dip	1.39 ± 0.16	1.19 ± 0.07

Table B.7: The measured α-values of sample A8.

B.4 Etched waveguide with soft topcladding

	Before poling		After poling	
	TM	TE	TM	TE
$E_{int}\ \left(\frac{V}{\mu m}\right)$	0.69 ± 1.89	-14.00 ± 4.87	-14.69 ± 5.58	-12.98 ± 4.25
$\chi^{(3)}\ \left(10^{-22}\frac{m^2}{V^2}\right)$	4.11 ± 0.16	2.86 ± 0.24	3.27 ± 0.26	3.31 ± 0.21
$\chi^{(2)}_{eff}\ \left(10^{-3}\frac{pm}{V}\right)$	0.86 ± 2.33	-12.03 ± 4.06	-14.41 ± 5.35	-12.90 ± 4.14

Table B.8: E_{int}, $\chi^{(2)}_{eff}$ and $\chi^{(3)}$ for sample 4_3_2. The sample was D_2 loaded. After D_2 outdiffusion a Bragg grating was made using $0.5\frac{kJ}{cm^2}$. The sample was poled at -2kV, 357°C for 20 minutes.

Before poling	After poling
1.44 ± 0.13	0.99 ± 0.10

Table B.9: The measured α-values of sample 4_3_2.

B.5 Waveguide exposed to different UV fluences

	Before UV flood exposure		After UV flood exposure	
	TM	TE	TM	TE
$E_{int}\ \left(\frac{V}{\mu m}\right)$	9.43 ± 3.97	0 ± 0	-2.95 ± 7.69	9.03 ± 3.83
$\chi^{(3)}\ \left(10^{-22}\frac{m^2}{V^2}\right)$	2.78 ± 0.15	2.46 ± 0.16	2.72 ± 0.29	2.72 ± 0.15
$\chi^{(2)}_{eff}\ \left(10^{-3}\frac{pm}{V}\right)$	7.86 ± 3.28	0 ± 0	-2.41 ± 6.27	7.36 ± 3.10

Table B.10: E_{int}, $\chi^{(2)}_{eff}$ and $\chi^{(3)}$ for sample 17_1. The sample was not D_2 loaded before writing of the Bragg grating using $3\frac{kJ}{cm^2}$. $10\frac{kJ}{cm^2}$ was used in the flood UV exposure.

Before UV flood exposure	After UV flood exposure
1.13 ± 0.10	1.00 ± 0.12

Table B.11: The measured α-values for sample 17_1 measured before and after UV flood exposure.

	Low λ_{Bragg} dip		High λ_{Bragg} dip	
	TM	TE	TM	TE
E_{int} $\left(\frac{V}{\mu m}\right)$	-4.07 ± 3.47	0 ± 0	0.15 ± 3.80	0 ± 0
$\chi^{(3)}$ $\left(10^{-22}\frac{m^2}{V^2}\right)$	2.95 ± 0.14	3.08 ± 0.13	3.01 ± 0.16	3.01 ± 0.20
$\chi^{(2)}_{eff}$ $\left(10^{-3}\frac{pm}{V}\right)$	3.60 ± 3.07	0 ± 0	0.13 ± 3.43	0 ± 0

Table B.12: E_{int}, $\chi^{(2)}_{eff}$ and $\chi^{(3)}$ for sample 17_1 after D_2 loading and a UV exposure using a fluence of $4\frac{kJ}{cm^2}$.

High λ_{Bragg} dip	Low λ_{Bragg} dip
0.98 ± 0.08	0.96 ± 0.06

Table B.13: The measured α-values for sample 17_1 after D_2 loading and UV flood exposure.

B.6 Varying nitrogen content in the core

	TE
$E_{int}\ \left(\frac{V}{\mu m}\right)$	1.39 ± 2.74
$\chi^{(3)}\ \left(10^{-22}\frac{m^2}{V^2}\right)$	2.96 ± 0.24
$\chi^{(2)}_{eff}\ \left(10^{-3}\frac{pm}{V}\right)$	1.23 ± 2.43

Table B.14: E_{int}, $\chi^{(2)}_{eff}$ and $\chi^{(3)}$ for sample 128_1. The sample was D_2 loaded prior to Bragg grating writing. The grating fluence was $0.8\frac{kJ}{cm^2}$.

	TE
$E_{int}\ \left(\frac{V}{\mu m}\right)$	22.04 ± 2.43
$\chi^{(3)}\ \left(10^{-22}\frac{m^2}{V^2}\right)$	2.45 ± 0.15
$\chi^{(2)}_{eff}\ \left(10^{-3}\frac{pm}{V}\right)$	16.21 ± 1.49

Table B.15: E_{int}, $\chi^{(2)}_{eff}$ and $\chi^{(3)}$ for sample 127_1. The sample was D_2 loaded prior to Bragg grating writing. The grating fluence was $0.8\frac{kJ}{cm^2}$.

	TE	TM
$E_{int}\ \left(\frac{V}{\mu m}\right)$	4.35 ± 3.66	3.27 ± 3.97
$\chi^{(3)}\ \left(10^{-22}\frac{m^2}{V^2}\right)$	2.00 ± 0.22	2.28 ± 0.27
$\chi^{(2)}_{eff}\ \left(10^{-3}\frac{pm}{V}\right)$	2.61 ± 2.18	2.24 ± 2.71

Table B.16: E_{int}, $\chi^{(2)}_{eff}$ and $\chi^{(3)}$ for sample 126_2. The sample was D_2 loaded prior to Bragg grating writing. The grating fluence was $0.2\frac{kJ}{cm^2}$.

α	1.14 ± 0.18

Table B.17: The measured α-value for sample 126_2.

	TE	TM
E_{int} $\left(\frac{V}{\mu m}\right)$	-2.43 ± 3.07	-0.70 ± 2.70
$\chi^{(3)}$ $\left(10^{-22}\frac{m^2}{V^2}\right)$	2.10 ± 0.19	2.07 ± 0.17
$\chi^{(2)}_{eff}$ $\left(10^{-3}\frac{pm}{V}\right)$	-1.53 ± 1.93	-0.43 ± 1.68

Table B.18: E_{int}, $\chi^{(2)}_{eff}$ and $\chi^{(3)}$ for sample 125_1. The sample was D_2 loaded prior to Bragg grating writing. The grating fluence was $0.2\frac{kJ}{cm^2}$.

α	0.99 ± 0.12

Table B.19: The measured α-value for sample 125_1.

B.7 Samples having a trapping layer

	Before poling		After poling	
	TM	TE	TM	TE
$E_{int}\ \left(\frac{V}{\mu m}\right)$	-8.35 ± 10.96	‡	89.89 ± 15.83	‡
$\chi^{(3)}\ \left(10^{-22}\frac{m^2}{V^2}\right)$	2.97 ± 0.52	‡	2.53 ± 0.39	‡
$\chi^{(2)}_{eff}\ \left(10^{-3}\frac{pm}{V}\right)$	-7.45 ± 9.68	‡	68.18 ± 5.82	‡

Table B.20: E_{int}, $\chi^{(2)}_{eff}$ and $\chi^{(3)}$ for sample #52. The sample was D_2 loaded and the core was UV written using a fluence of $3.0\frac{kJ}{cm^2}$. After D_2 outdiffusion a Bragg grating was made using $1\frac{kJ}{cm^2}$. The sample was poled at -2kV, 357°C for 20 minutes. ‡indicates that meaningfull measurements on the TE polarization were not possible.

	Before poling		After poling	
	TM	TE	TM	TE
$E_{int}\ \left(\frac{V}{\mu m}\right)$	5.07 ± 8.66	6.59 ± 6.11	†	†
$\chi^{(3)}\ \left(10^{-22}\frac{m^2}{V^2}\right)$	2.62 ± 0.43	2.84 ± 0.32	†	†
$\chi^{(2)}_{eff}\ \left(10^{-3}\frac{pm}{V}\right)$	3.98 ± 6.76	5.61 ± 5.16	†	†

Table B.21: E_{int}, $\chi^{(2)}_{eff}$ and $\chi^{(3)}$ for sample #57. The sample was D_2 loaded and the core was UV written using a fluence of $3.0\frac{kJ}{cm^2}$. After D_2 outdiffusion a Bragg grating was made using $1\frac{kJ}{cm^2}$. The sample was poled at -2kV, 357°C for 20 minutes. †indicates that dielectric breakdown occurred during poling preventing further measurements on the sample.

α	0.92 ± 0.18

Table B.22: The measured α-value before poling for sample #57.

	Before poling		After poling	
	TM	TE	TM	TE
$E_{int}\ \left(\frac{V}{\mu m}\right)$	-0.02 ± 5.70	1.82 ± 5.93	167.54 ± 25.07	147.71 ± 28.38
$\chi^{(3)}\ \left(10^{-22}\frac{m^2}{V^2}\right)$	3.19 ± 0.34	3.49 ± 0.59	2.59 ± 0.37	4.53 ± 0.82
$\chi^{(2)}_{eff}\ \left(10^{-3}\frac{pm}{V}\right)$	-0.02 ± 5.46	1.91 ± 6.20	130.14 ± 5.96	200.68 ± 13.29

Table B.23: E_{int}, $\chi^{(2)}_{eff}$ and $\chi^{(3)}$ for sample #65. The sample was D_2 loaded and the core was UV written using a fluence of $3.0\frac{kJ}{cm^2}$. After D_2 outdiffusion a Bragg grating was made using $1\frac{kJ}{cm^2}$. The sample was poled at -2kV, 357°C for 20 minutes.

γ	0.65 ± 0.05

Table B.24: The measured γ-value of sample #65.

Before poling	After poling
0.91 ± 0.18	0.57 ± 0.13

Table B.25: The measured α-value of sample #65.

Bibliography

[1] M. Abe, T. Kitagawa, K. Hattori, A. Himeno, and Y. Ohmori. Electro-optic switch constructed with a poled silica-based waveguide on a si substrate. *Electron. Lett.*, 32(10):893–894, 1996.

[2] G. P. Agrawal. *Fiber-optic communication systems.* John Wiley & Sons, Inc., 1997. ISBN 0-471-17540-4.

[3] Ando Electric Co., Ltd. *Tunable Laser Source AQ4321A/4321D.* http://www.ando.com/mid/pdfs/AQ4321AD1219.pdf.

[4] J. Arentoft, M. Kristensen, S. I. Bozhevolnyi, and P. Shi. Poling of silica with silver-containing electrodes. *Electron. Lett.*, 36(19):1635–1636, 2000.

[5] J. Arentoft, M. Kristensen, and J. B. Jensen. Poling of planar silica waveguides. *OSA trends in optics and photonics*, 29:227–234, 1999.

[6] Jesper Arentoft. *Poling of planar silica-based waveguides.* PhD thesis, COM, Danish Technical University, 2000.

[7] J. P. Bernardin and N. M. Lawandy. Dynamics of the formation of Bragg gratings in germanosilicate optical fibers. *Opt. Commun.*, 79(3):194–199, 1990.

[8] P. Blazkiewicz, W. Xu, and S. Fleming. Modification of the third-order nonlinearity in poled silica fibers. *Proc. of SPIE - The International Society for Optical Engineering*, 4216:129–138, 2001.

[9] A. Boskovic, S. V. Chernikov, J. R. Taylor, L. Gruner-Nielsen, and O. A. Levring. Direct continuous-wave measurement of n_2 in various types of telecommunication fiber at $1.55\mu m$. *Opt. Lett.*, 21(24):1966–1968, 1996.

[10] D. K. Cheng. *Fundamentals of engineering electromagnetics.* Addison-Wesley, 1993. ISBN 0-201-56611-7.

[11] Optiwave Corporation. IFO Gratings 4.0. http://www.optiwave.com/.

[12] Photon Design. CrystalWave. www.photond.com.

[13] K. Færch and M. Svalgaard. Symmetrical waveguide devices fabricated by direct UV writing. *IEEE Photon. Technol. Lett.*, 14(2):173–175, 2002.

[14] K. Færch and M. Svalgaard. UV-written waveguides with a high index step. *POWAG'2002*, FA5:77–79, 2002.

[15] J. Fage-Pedersen and M. Kristensen. Poling of glass waveguides by a metal-induced $\chi^{(3)}$ enhancement. *Accepted for CLEO-EUROPE*, 2003.

[16] D. Frohman-Bentchkowsky and M. Lenzlinger. Charge transport and storage in metal-nitride-oxide-silicon (MNOS) structures. *Jour. of Appl. Phys.*, 40(8):3307–3319, 1969.

[17] Dov Frohman-Bentchkowsky. The metal-nitride-oxide-silicon (MNOS) transistor-characteristics and applications. *Proc. of the IEEE*, 58(8):1207–1219, 1970.

[18] T. Fujiwara, M. Takahashi, and A. J. Ikushima. Decay behaviour of second-order nonlinearity in GeO_2-SiO_2 glass poled with UV-irradiation. *Electron. Lett.*, 33(11):980–982, 1997.

[19] T. Fujiwara, D. Wong, Y. Zhao, S. Fleming, S. Poole, and M. Sceats. Electro-optic modulation in germanosilicate fibre with UV-excited poling. *Electron. Lett.*, 31(7):573–575, 1995.

[20] N. Godbout, S. Lacroix, Y. Quiquempois, G. Martinelli, and P. Bernage. Measurement and calculation of electrostrictive effects in a twin-hole silica glass fiber. *Jour. of the Opt. Society of America B*, 17(1):1–5, 2000.

[21] F. Haberl, J. Hochreiter, J. Zehetner, and A. J. Schmidt. Electrical breakdown in ge-doped silica glass fibers. *Int. Jour. of Optoelectron.*, 5(4):363–366, 1990.

[22] D. P. Hand and P. St. Russell. Photoinduced refractive-index changes in germanosilicate fibers. *Opt. Lett.*, 15(2):102–104, 1990.

[23] E. Hecht. *Optics*. Addison-Wesley, 1998. ISBN 0-201-30425-2.

[24] K. O. Hill, Y. Fujii, D. C. Johnson, and B. S. Kawasaki. Photosensitivity in optical fiber waveguides: Application to reflection filter fabrication. *Appl. Phys. Lett.*, 32(10):647–649, 1978.

[25] K. O. Hill, B. Malo, F. Bilodeau, D. C. Johnson, and J. Albert. Bragg gratings fabricated in monomode photosensitive optical fiber by UV

exposure through a phase mask. *Appl. Phys. Lett.*, 62(10):1035–1037, 1993.

[26] J. Hübner, D. Zauner, and M. Kristensen. Strong sampled Bragg gratings for WDM applications. *IEEE Photon. Technol. Lett.*, 10(4):552–554, 1998.

[27] Jörg Hübner. *Index engineering with Excimer light.* PhD thesis, Mikroelektronik Centret, Danish Technical University, 1998.

[28] M. Janos, W. Xu, D. Wong, H. Inglis, and S. Fleming. Growth and decay of the electrooptic effect in thermally poled B/Ge codoped fiber. *Jour. of Lightwave Tech.*, 17(6):1037–1041, 1999.

[29] Jesper Bo Damm Jensen. *UV writing of advanced Bragg gratings in optical waveguides.* PhD thesis, COM, Danish Technical University, 2002.

[30] H.-K. Kang, D.-H. Kang, C.-S. Hong, and C.-G. Kim. Simultaneous monitoring of strain and temperature during and after cure of unsymmetric composite laminate using fibre-optic sensors. *Smart Materials and Structures*, 12(1):29–35, 2003.

[31] Raman Kashyap. *Fiber Bragg gratings.* Academic Press, 1999. ISBN 0-12-400560-8.

[32] P. G. Kazansky and P. St. J. Russel. Thermally poled glass: Frozen-in electric field or oriented dipoles? *Opt. Commun.*, 110:611–614, 1994.

[33] S. Keilich. Optical second-harmonic generation by electrically polarized isotropic media. *IEEE Jour. of Quantum Electron.*, QE-5(12):562–568, 1969.

[34] M. Khoshnevisan and P. Yeh. Relationship between nonlinear electrostrictive Kerr effects and acousto-optics. *Proc. of SPIE - The International Society for Optical Engineering*, 739:82–86, 1987.

[35] K. S. Kim, R. H. Stolen, W. A. Reed, and K. W. Quoi. Measurement of the nonlinear index of silica-core and dispersion-shifted fibers. *Opt. Lett.*, 19(4):257–259, 1994.

[36] M. Kristensen. Ultraviolet-light-induced processes in germanium-doped silica. *Phys. Rev. B*, 64(14):144201–1–144201–12, 2001.

[37] C. Laurent-Lund. Oxidize. Program used to calculate the thickness of thermal oxide layers.

[38] P. J. Lemaire. Reliability of optical fibers exposed to hydrogen: prediction of long-term loss increases. *Opt. Eng.*, 30(4):1062–1071, 1991.

[39] P. J. Lemaire, R. M. Atkins, V. Mizrahi, and W. A. Reed. High pressure H_2 loading as a technique for achieving ultrahigh UV photosensitivity and thermal sensitivity in GeO_2 doped optical fibers. *Electron. Lett.*, 29(13):1191–1193, 1993.

[40] A. Liu, M. Digonnet, and G. Kino. DC Kerr coefficient in silica: theory and experiment. *Proc. of SPIE - The International Society for Optical Engineering*, 3542:102–107, 1998.

[41] A. C. Liu, M. J. F. Digonnet, and G. S. Kino. Measurement of the DC Kerr and electrostrictive phase modulation in silica. *Jour. of the Opt. Society of America B*, 18(2):187–194, 2001.

[42] X.-C. Long and S. R. J. Brueck. Large-signal phase retardation with a poled electrooptic fiber. *IEEE Photon. Technol. Lett.*, 9(6):767–769, 1997.

[43] C. J. Marckmann, J. Arentoft, and M. Kristensen. Measuring poling-induced nonlinearities in Ge:SiON waveguides using a Bragg grating. *Optical Fiber Communication Conference*, Tech. Dig.:WDD94–1–WDD94–3, 2001.

[44] C. J. Marckmann, G. Genty, Y. Ren, and M. Kristensen. Bragg gratings as probes to dertermine nonlinearities induced by thermal poling. *Bragg gratings, Photosensitivity, and Poling in Glass Waveguides conference*, Tech. Dig.:BFC3–1–BFC3–3, 2001.

[45] C. J. Marckmann, R. Shim, Y. Ren, and M. Kristensen. Interpretation of high poling effects with short lifetimes. *European Conference on Integrated Optics*, 1:301–304, 2003.

[46] W. Margulis, F. C. Garcia, E. N. Hering, L. C. Guedes Valente, B. Lesche, F. Laurell, and I. C. S. Carvalho. Poled glasses. *MRS Bulletin*, 23(11):31–35, 1998.

[47] P. V. S. Marques, J. R. Bonar, A. M. P. Leite, and J. S. Aitchison. Simultaneous UV direct writing of channel waveguides and Bragg gratings in Germanium-doped planar silica. *IEEE Jour. of selected topics in Quantum Electron.*, 8(6):1316–1322, 2002.

[48] S. Matsumoto, T. Fujiwara, Y. Seno, Y. Hirose, M. Ohama, and A. J. Ikushima. Crystallization and optical nonlinearity in $GeO_2 - SiO_2$ glass poled with ArF excimer-laser irradiation. *Jour. of Appl. Phys.*, 88(12):6993–6996, 2000.

[49] Kent Erik Mattsson. Plasma-enhanced growth, composition, and refractive index of silicon oxy-nitride films. *Jour. of Appl. Phys.*, 77(12):6616–6623, 1995.

[50] G. Meltz, W. W. Morey, and W. H. Glenn. Formation of Bragg gratings in optical fibers by a transverse holographic method. *Opt. Lett.*, 14(15):823–825, 1989.

[51] Douglas B. Murphy. *Fundamentals of light microscopy and electronic imaging.* Wiley-Liss, Inc., 2001. ISBN 0-471-25391-X.

[52] R. A. Myers, X.-C. Long, and S. R. J. Brueck. Recent advances in the second-order nonlinear optical properties of amorphous silica materials. *Proc. of SPIE - The International Society for Optical Engineering*, 2289:98–109, 1994.

[53] R. A. Myers, N. Mukherjee, and S. R. Brueck. Large second-order nonlinearity in poled fused silica. *Opt. Lett.*, 16(22):1732–1734, 1991.

[54] R. E. Newnham, W. Sundar, R. Yimnirun, J. Su, and Q. M. Zhang. Electrostriction: Nonlinear electromechanical coupling in solid dielectrics. *Jour. Phys. Chem. B*, 101(48):10141–10150, 1997.

[55] A. Othonos and K. Kalli. *Fiber Bragg gratings: fundamentals and applications in telecommunications and sensing.* Artech House, Inc., 1999. ISBN 0-89006-344-3.

[56] D. L. Philen, D. W. Peckham, and I. Brener. Measurement of the nonlinear index of refraction, N_2, for various fiber types. *Optical Fiber Communication Conference*, Thursday:184–186, 2000.

[57] B. Poumellec, I. Riant, P. Niay, P. Bernage, and J. F. Bayon. UV induced densification during Bragg grating inscription in Ge:SiO_2 preforms: Interferometric microscopy investigations. *Optical Materials*, 4(2):404–409, 1995.

[58] P. N. Prasad and D. J. Williams. *Introduction to nonlinear optical effects in molecules and polymers.* John Wiley & Sons, Inc., 1991. ISBN 0-471-51562-0.

[59] Y. Ren, C. J. Marckmann, J. Arentoft, and M. Kristensen. Thermally poled channel waveguides with polarization-independent electrooptic effect. *IEEE Photon. Technol. Lett.*, 14(5):639–641, 2002.

[60] Y. Ren, C. J. Marckmann, R. Shim, and M. Kristensen. Increased electro-optic effect in poled waveguides with a charge-trapping layer. Submitted for the Bragg gratings, Photosensitivity, and Poling in Glass Waveguides conference, 2003.

[61] B. E. A. Saleh and M. C. Teich. *Fundamentals of photonics.* John Wiley & Sons, Inc., 1991. ISBN 0-471-83965-5.

[62] Y. Sasaki and Y. Ohmori. Phase-matched sum-frequency light in optical fibers. *Appl. Phys. Lett.*, 39(6):466–468, 1981.

[63] Horst Scholze. *Glass: Nature, structure and properties.* Springer-Verlag New York, Inc., 1991. ISBN 0-387-97396-6.

[64] J. F. Shackelford, P. L. Studt, and R. M. Fulrath. Solubility of gases in glass. II. He, Ne, and H_2 in fused silica. *Jour. of Appl. Phys.*, 43(4):1619–1626, 1972.

[65] J. Stone. Interactions of hydrogen and deuterium with silica optical fibers: A review. *Jour. of Lightwave Tech.*, LT-5(5):712–733, 1987.

[66] Y. Sun, W. W. Cao, and L. E. Cross. Electrostriction effect in glass. *Material Letters*, 4(8):329–336, 1986.

[67] M. Svalgaard. Personal communication with M. Svalgaard. 2003.

[68] M. Svalgaard. Effect of D_2 outdiffusion on direct UV writing of optical waveguides. *Electron. Lett.*, 35(21):1840–1842, 1999.

[69] Richard Syms and John Cozens. *Optical guided waves and devices.* McGRAW-HILL Book Company Europe, 1992. ISBN 0-007-707425-4.

[70] K. t. Lau, L. Yuan, L. m. Zhou, J. Wu, and C. h. Woo. Strain monitoring in FRP laminates and concrete beams using FBG sensors. *Composite Structures*, 51(1):9–20, 2001.

[71] C2V Concept to Volume. OlympiOs. www.c2v.nl.

[72] A. L. C. Triques, C. M. B. Cordeiro, V. Balestrieri, B. Lesche, W. Margulis, and I. C. S. Carvalho. Depletion region in thermally poled fused silica. *Appl. Phys. Lett.*, 76(18):2496–2498, 2000.

[73] J. van Turnhout. *Thermally stimulated discharge of polymer electrets.* Elsevier Scientific Publishing Company, 1975. ISBN 0-444-41290-5.

[74] J. van Turnhout. *Electrets.* Springer-Verlag Berlin Heidelberg, 1980. ISBN 0-387-09570-5.

[75] H. Vendeltorp-Pommer. *Numerical analysis of optical fibers with non-circular symmetry in the refractive index profile.* PhD thesis, Electromagnetics Inst., Danish Technical University, 1989.

[76] D. Wong, W. Xu, S. Fleming, M. Janos, and K.-M. Lo. Frozen-in electrical field in thermally poled fibers. *Optical Fiber Technology*, 5(2):235–241, 1999.

[77] Y. Xi, Z. Xu, Z. Hou, L. Liu, L. Xu, W. Wang, M. Affatigato, and S. Feller. Second-order optical nonlinearity in bulk PbO/B_2O_3 glass. *Opt. Commun.*, 210(3–6):466–468, 2002.

[78] W. Xu, P. Blazkiewicz, S. Fleming, and A. Canagasabey. Fibre poling. *Bragg gratings, Photosensitivity, and Poling in Glass Waveguides conference*, Technical Digest:BFC1–1–BFC1–3, 2001.

[79] W. Xu, P. Blazkiewicz, S. Fleming, and D. Tang. Stability of the change of the third-order nonlinearity in silica fibre. *Optical Fiber Communication Conference*, Wednesday:WW4–1–WW4–3, 2001.

[80] Dan Anker Zauner. *Integrated optical devices for wavelength division multiplexing using PECVD and direct UV-writing techniques.* PhD thesis, COM, Danish Technical University, 1999.